TECHNISCHE UNIVERSITÄT MÜNCHEN

Fachgebiet Physik der weichen Materie

Structural ordering in block copolymer thin films

Alessandro Sepe

Vollständiger Abdruck der von der Fakultät für Physik der Technischen Universität München zur Erlangung des akadamischen Grades eines

Doktors der Naturwissenschaften (Dr. rer. nat.)

genehmigten Dissertation.

Vorsitzender: Univ.-Prof. Dr. Harald Friedrich

Prüfer der Dissertation:

1. Univ.-Prof. Christine M. Papadakis, Ph.D.
2. Univ.-Prof. Dr. Thorsten Hugel

Die Dissertation wurde am 03.05.2012 bei der Technischen Universität München eingereicht und durch die Fakultät für Physik am 08.06.2012 angenommen.

Preface

The following Ph.D. thesis was developed under the supervision of Prof. Christine M. Papadakis, group-leader of the Physik weicher Materie group at the Physik-Department, Technische Universität München. The Ph.D. project was developed between 2009 and 2012 and it has been funded by the International Graduate School "Materials Science of Complex Interfaces" (CompInt), which Prof. Thorsten Hugel, group-leader of the “Molecular Machines” group at the Zentralinstitut für Medizintechnik, Biophysik-Department at the Technische Universität München, has been co-advisor of. Part of the polymers used within the Ph.D. research project were synthesised in Prague, Czech Republic, by the group of Peter Černoch at the Institute of Macromolecular Chemistry, Academy of Sciences of the Czech Republic. Within the framework of the CompInt programme, a collaboration between our group and the group of Prof. Ullrich Steiner, group-leader of the Thin Films and Interfaces group at the Cavendish laboratory, Department of Physics at the University of Cambridge, United Kingdom, was created and strengthen, resulting in a three months internship within Prof. Steiner’s group.

Abstract

The Ph.D. research project was aimed to study the structural changes in thin block copolymer films during thermal and solvent vapour treatment. Combining imaging with scattering methods, the surface texture and the inner film structure was investigated. In-situ grazing-incidence small-angle X-ray scattering at large facilities (GISAXS at HASYLAB, DESY, Hamburg and at CHESS, Cornell University, USA) and VIS-interferometry are combined with ex-situ atomic force microscopy (AFM) and X-ray reflectometry (XR). The poly(styrene-*b*-butadiene) (P(S-*b*-B)) system studied during the Ph.D. project is well-suited because the initial lamellar orientation can be controlled, and well-oriented morphologies can be prepared by tuning the substrate properties. The study aimed at revealing the most efficient way of creating long-range order by post-treatment of spin-coated, defectuous films. Moreover, during the Ph.D. project a poly(4-octylstyrene-*b*-butylmethacrylate) (P(OS-*b*-BMA)) system was studied in order to understand the pathway leading to the creation of lateral structures in di-block copolymer thin films during vapour uptake and subsequent drying, with particular interest in the effect of the film thickness (D_{film})

The PhD. research project therefore includes three studies.

The first part of the Ph.D. project was dedicated to the study of the temperature-dependence of the nanostructure of thin block copolymer films, as studied using in-situ GISAXS and VIS-interferometry as well as ex-situ AFM and XRR. We focused on spin-coated P(S-*b*-B) di-block copolymer thin films featuring lamellae perpendicular to the substrate. In-situ GISAXS measurements elucidated the structural changes during heat treatment at temperatures between 60 and 130°C. We showed that the thermal treatment below 100°C does not destroy the perpendicular lamellar order. In contrast, treatment between 105 and 120°C leads to a broad distribution of lamellar orientations which only partially recovers upon subsequent cooling. Treatment at 130°C leads to severe changes of the film structure. We attributed the change of behavior at 100°C to the onset of the glass transition of the polystyrene block and the related increase of long-range mobility. Moreover, we identified that the perpendicular lamellar orientation for high molar mass samples is not stable under all conditions.

The second part of the Ph.D. research project focuses on the structural ordering of a thin film of lamellae-forming P(S-*b*-B) in cyclohexane (CHX) vapour, which is a solvent slightly selective for polybutadiene (PB). During the Ph.D. project a completely customized and remote controlled sample cell was developed in order to precisely control the degree of swelling of the film, in-situ, for all the experiments performed at the large facilities. The resulting structural changes during the whole treatment were then monitored in-situ using GISAXS and VIS-interferometry and ex-situ by means of XR. During the vapour treatment, the lamellar thickness (D_{lam}) is observed to increase, meanwhile a transient state with lower degree of lamellar order and orientation is followed by a large scale reorganization resulting in a dominant lamellar alignment along the direction parallel with respect to substrate. Upon drying, the number of correlated lamellae (N_S) decreases, stabilizing at a value sensitively

higher than the initial one. The increased mobility of the swollen polymer and the decreasing of the segment-segment interaction parameter in the film as function of the solvent volume fraction, induce a large scale rearrangement of the blocks, which eventually results in a long range order of the parallel lamellae, reaching a more equilibrated state after annealing. Additionally, these results point to the formation of additional lamellae due to an increased degree of coiling of the polymer during vapour treatment. We propose a model for the description of the dependence of the D_{lam} on the polymer volume fraction $\phi_{polymer}$ upon solvent vapour treatment and subsequent drying.

The third part of the Ph.D. project was aimed to study the structure formation in lamellar P(OS-*b*-BMA) films during exposure to saturated vapour of *n*-hexane (a poor solvent for both blocks) and subsequent drying using real-time in-situ GISAXS. Previous surface studies on hexane treated samples revealed a lateral surface structure[1]. We focused on the effect of film thickness which is varied between 1.3 and 2.0 times the bulk lamellar thickness. We investigated the lateral repeat distance as well as the correlation length in the film plane. Complex, non-monotonous behavior was observed for both parameters. We identified that the kinetics depends strongly on the film thickness; especially for the thinnest film, it is very slow. Moreover, upon drying, the lateral structure created during vapour treatment is stable only for the thick film, not for the intermediate and the thin film.

In order to analyse and subsequently interpret all the data collected during the whole Ph.D. research project, a completely personalised software, the GISAXS Analysis Package, has been developed within the Igor pro environment, which is freely available at http://users.ph.tum.de/gu68boq/.

Contents

Acknowledgements **1**

1 Theory **4**

1.1 Polymers 4

1.2 Block copolymers 6

1.3 Block copolymer thin films 22

1.4 The glass transition temperature 27

1.5 Solvent 30

2 Sample preparation and characterisation **34**

2.1 Poly(styrene-*b*-1,4-butadiene) 34

2.2 Poly(4-octylstyrene-*b*-butylmethacrylate) 35

2.3 Film preparation 35

2.4 VIS-interferometry 36

2.5 Atomic force microscopy 40

2.6 X-ray reflectometry 41

2.7 Grazing-incidence small-angle X-ray scattering 43

2.8 Small-angle X-ray scattering 48

3 Structural changes during thermal treatment **49**

3.1 Experimental procedure and results 51

3.2 Conclusion 62

4 Structural changes during solvent vapour treatment **66**

4.1 Experimental procedure and results 68

4.2 Conclusion 94

5 Creation of lateral structure during solvent vapour treatment 97

5.1 Experimental procedure and results ……..…… 98

5.2 Conclusion ……..…… 115

6 Conclusion 116

List of publications 120

Bibliography 122

Acknowledgements

I would like to thank you very much Prof. Christine M. Papadakis for proposing me a very interesting topic for my research project, which was for me a valuable spur for further learning and growing both professionally and personally. Therefore, I want thank you very much Prof. Papadakis for her patience and guidance, for her always prompt support and for teaching me how to become a complete researcher. I will treasure all her suggestions and advises which will eventually result in precious supports for facing all my future academic steps.

I do thank you very much Prof. Peter Müller-Buschbaum, for the fruitful discussions which helped me to expand the knowledge on my research topic, achieving a deeper insight on it.

I would like to thank you very much Prof. Thorsten Hugel, for the precious discussions and invaluable support. Prof. Hugel has been a strong reference for me during my whole PhD. project, not only as simple co-advisor but overall as an extraordinary mentor who gave to me the initial opportunity to enter this extraordinary universe of scientific potentialities, which polymer physics represent for me and which I will be to him always grateful of.

I do thank you very much Prof. Dorthe Posselt for her extraordinary support during several beam times and outstanding contribution to my research project.

Thank you very much to the beam line responsibles, Jan Perlich, Detlef M. Smilgies and Jean-Francois Moulin who made me possible to achieve extraordinary results during the challenging beam times, which are then the very core of my whole PhD. project.

A special thank you goes to Semih, Tilo, Joseph, Sebastian and Anastasia for sharing with me all the challenges of this PhD. project, both on the professional and personal side, I will always treasure within me all the wonderful moment shared together. I do thank you very much Zhenyu for supporting me and helping me to start properly my PhD. project. Thank you very much to Kostantinos for the nice and productive time spent together and Jianqi for the valuable help during the beam time.

I do thank you very much Bizan Balzer and Tobias Pirzer for helping me during the whole PhD. with their outstanding support. Thank you to Markus Rauscher for the inspiring discussions, which always result in new and brilliant idea.

Of course, I would like to thank you very much the whole group of the Chair of Functional Materials for supporting me anyhow and contributing to create around me a wonderful environment.

Thank you very much to Prof. Ullrich Steiner and his whole group at the Cavendish laboratory for the great collaboration and wonderful research environment, which allow me to further expand my knowledge and learn new techniques.

Chapter 1

Theory

1.1 Polymers

The word (poly)-(mer) means (many)-(parts) and refers to molecules consisting of many elementary units, called monomers. Monomers are structural repeating units of a polymer that are connected to each other by covalent bonds. The entire structure of a polymer is generated during polymerization, during this process the monomers are bonded together covalently. The number of monomers in a polymer molecule is called its degree of polymerization *N*. The molar mass *M* of a polymer is equal to the overall degree of polymerization times the molar mass of its monomer[2], M_{mon}:

$$M = N \cdot M_{mon} \tag{1.1}$$

The conventional way to describe the mass of a polymer chain is the molar mass, i.e. the mass of one mole (equal to Avogadro's number, N_{Av}) of these molecules. The chemical identity of monomers is one of the main factors determining the properties of a polymeric system. Another major factor is the organization of atoms along the chain, defined as microstructure, which is fixed during the polymerization process. The polymer microstructure cannot be changed without breaking covalent chain bonds.[2]

Macromolecules that contain monomers of only one type are called homopolymers (Figure 1.1).

Figure 1.1. Representation of an homopolymer which contain the same type of monomers (*A*) bonded together.

Homopolymer are made from the same monomer, but may differ by their microstructure, degree of polymerization or architecture. In particular, the degree of

polymerization of macromolecules is a major factor determining many properties of polymeric systems.[2] Linear polymers contain between 20 and 10 billion monomers. The physical properties of molecules change as monomers are linked together. In fact, both the boiling point and the melting point increase rapidly with the number of backbone bonds, this result in different uses of these molecules. Polymeric architecture is another important feature controlling the properties of polymeric systems.[2] There are several types of polymer architectures as shown in Figure 1.2.

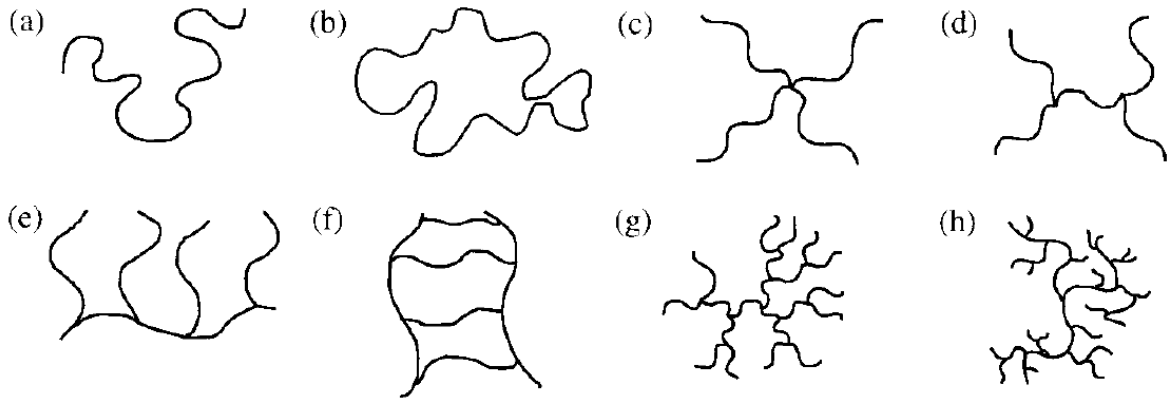

Figure 1.2. Different polymer architectures: (a) linear; (b) ring; (c) star; (d) *H*; (e) comb; (f) ladder; (g) dendrimer; (h) randomly branched.[2]

Combining several different types of monomers into a single chain leads to new macromolecules, heteropolymers. The properties of heteropoplymers depend on both on composition and on the sequence in which these different monomers are combined into the chain. Macromolecules containing two different monomers are called copolymers. A different sequence in which the monomers are bonded together, results in different types of copolymers (Figure 1.3).[2] Polymers containing two blocks are called di-block copolymers, which are of particular interest for this Ph.D. research project.

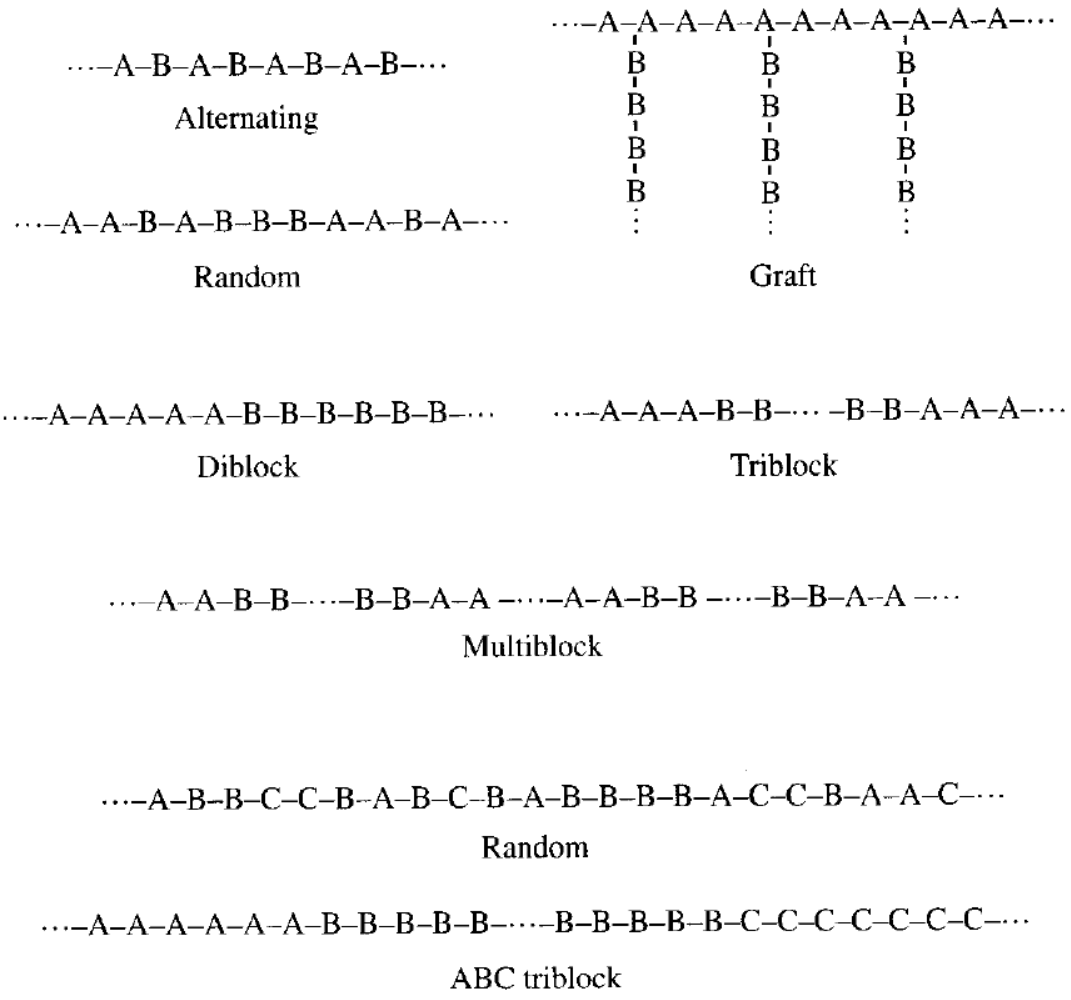

Figure 1.3. Different types of copolymers.[2]

1.2 Block copolymers

Block copolymers (BCPs) consist of two or more chemically different polymer fragments, or blocks, covalently bonded together to form a larger, more complex macromolecule. If the constituent polymers are immiscible, phase separation is induced on a scale that is directly related to the size of the copolymer chains, which results in morphologies characterised by a pattern of chemically distinct domains of periodicity D_{AB} in the 10–100 nm range. The order-to-disorder transition (ODT) temperature and the specific morphologies formed by a given BCP are functions of the polymer molecular weight, the segmental interactions, and the volume

composition. The BCP composition in particular strongly determines the microphase morphology.[3] For example, di-block copolymers having blocks of comparable volume exhibit a lamellar structure. Di-block copolymers forming lamellar structures are the subject of this Ph.D. thesis. Increasing the degree of compositional asymmetry leads to the gyroid, cylindrical, and finally, spherical phases.[3] The fundamental phenomenon which leads to different classes of structures in dependence on the ratio between the degrees of polymerization of the A and B blocks is the microphase separation.[4]

To understand this dominating mechanism in block copolymer it is necessary to understand first the main properties of polymer blends and then their differences with block copolymers. A large part of applications oriented research is devoted to the study of polymer blends, since mixing opens a route for a combination of different properties. In many cases one is searching for materials that combine high stiffness with resistance to fracture. For the majority of common polymers these two requirements cannot be realized simultaneously, because an increase in stiffness, i.e., the elastic moduli, is usually associated with samples becoming more brittle and decreasing in strength. Using mixtures offers a chance to achieve good results for both properties. High-impact polystyrene, a mixture of polystyrene and polybutadiene, represents a prominent example. Whereas polystyrene is stiff but brittle, a blending with rubbers furnishes a tough material that still retains a satisfactory stiffness. Here mixing results in a two-phase structure with rubber particles of spherical shape being incorporated in the matrix of polystyrene. Materials are tough, if fracture energies are high due to yield processes preceding the ultimate failure, and these become initiated at the surfaces of the rubber spheres where stresses are intensified. On the other hand, inclusion of rubber particles in the polystyrene matrix results in only a moderate reduction in stiffness. Hence, the blending yields a material with properties that in many situations are superior to pure polystyrene. Polystyrene and polybutadieneare are indeed the constituent blocks of the lamellar di-block copolymers of which the study of their structural properties this Ph.D. thesis work is mainly aimed to. There are other cases, where an improvement of the mechanical properties is achieved by a homogeneous mixture of two polymers, rather than a two-phase structure. A well-known example is again given by polystyrene when blended with poly(phenyleneoxide). In this case, a homogeneous phase is formed and as it turns out in mechanical tests, it also exhibits a satisfactory toughness together with a high elastic modulus. Therefore it is of crucial importance understanding the mixing properties, i.e., a knowledge of under which conditions two polymeric compounds will form either a homogeneous phase or a two-phase structure. This knowledge can then be used to understand how structures develop and how this can be controlled.[4]

Flory and Huggins devised a general scheme that enables one to deal with the mixing properties of a pair of polymers. It provides a basic understanding of the occurrence of different types of phase diagrams, in dependence on temperature and

the molar masses. The mixing properties of two components may generally be discussed by considering the change in the Gibbs free energy.[4] If n_A moles of polymer A are contained in a volume V_A and n_B moles of polymer B, are contained in a volume V_B. Mixing may be initiated by removing the boundary between the two compartments, so that both components can expand to the full volume of size $V = V_A + V_B$. In order to find out whether a mixing would indeed occur, the change in the Gibbs free energy has to be considered. This change, called the Gibbs free energy of mixing and denoted ΔG_{mix}, is given by

$$\Delta G_{mix} = G_{AB} - (G_A + G_B) \tag{1.2}$$

where G_A, G_B and G_{AB} denote the Gibbs free energies of the compounds A and B in separate states and the mixed state, respectively.[4]

The Flory–Huggins theory represents ΔG_{mix} as a sum of two contributions:

$$\Delta G_{mix} = -T\Delta S_t + \Delta G_{loc} \tag{1.3}$$

which describe the two main aspects of the mixing process. Firstly, mixing leads to an increase of the entropy associated with the motion of the centers of mass of all polymer molecules, and secondly, it may change the local interactions and motions of the monomers. The latter part is referred as ΔG_{loc} and the increase in the translational entropy ΔS_t. ΔS_t and the related decrease $-T\,\Delta S_t$ in the Gibbs free energy always favor a mixing. ΔG_{loc}, instead, may act favorably or unfavorably, depending on the character of the monomer‑monomer pair interactions. In most cases, and, as can be verified, for van der Waals interactions generally, attractive energies between equal monomers are stronger than those between unlike pairs. This behavior implies $\Delta G_{loc} > 0$ and therefore opposes a mixing. As a free energy, ΔG_{loc} also accounts for changes in the entropy due to local effects. For example, a shrinkage or an expansion of the total volume on mixing results in a change in the number of configurations available for local motions of the monomeric units, hence in a change of entropy to be included in ΔG_{loc}.[4]

The decomposition of ΔG_{mix} in these two contributions points to the two main aspects of the mixing process. To make it more explicit we need to direct formulate the expressions for ΔS_t and ΔG_{loc}, so that the sum of the two contributions can be calculated. The Flory–Huggins theory is based on approximate equations for both parts, which can be calculated as follows.[4]

Considering the volume fractions ϕ_A and $\phi_B$of the two components in the mixture and denoting the perfect gas constant with R, the increase in the translational entropy is described by

$$\frac{\Delta S_t}{R} = -n_A \ln \phi_A - n_B \ln \phi_B \tag{1.4}$$

The change in the local interactions is, instead, expressed by the equation

$$\Delta G_{loc} = RT\frac{V}{v_c}\chi\phi_A\phi_B \quad (1.5)$$

where v_c is denoting the (molar) volume of a reference unit common to both polymers, usually it is identified with the volume occupied by one of the monomeric units. χ is instead the Flory–Huggins parameter, which is dimensionless and determines in empirical manner the change in the local free energy per reference unit.[4]

This parameter can be described within the mean field framework, where a system of interpenetrating interacting chains, which comprise the fluid mixture as being equivalent to a system of independent chains that interact with a common uniform mean field set up by the many chain system as a whole. The interaction of a given chain with all other chains, as represented in an integral form by the mean field, has two effects. The contacts with other chains screen the intramolecular excluded volume interactions, thus leading to ideal chain behavior. The Flory–Huggins theory assumes that this effect is maintained in a mixture, with unchanged conformational distributions. Moreover, being in contact with a large number of other chains, a given chain in a binary mixture effectively integrates over the varying monomer–monomer interactions and thus probes their average value. The change in the monomer–monomer interactions following from a mixing may therefore be expressed as change of the mean field, with uniform values for all units of the A-chains and B-chains, respectively.[4]

Originally the χ-parameter was introduced to account for the contact energies only. However, experiments indicate that ΔG_{loc} often includes an entropic part, so that in general

$$\Delta G_{loc} = \Delta H_{mix} - T\Delta S_{loc} \quad (1.6)$$

The enthalpic part ΔH_{mix} is present in the heat of mixing, which is positive for endothermal and negative for exothermal systems. The entropic part ΔS_{loc} is usually due to changes in the number of available local conformations.

Application of the two expressions for ΔS_t and ΔG_{loc}, equations (1.4) and (1.5), results in the Flory–Huggins formulation for the Gibbs free energy of mixing of polymer blends[4]

$$\Delta G_{mix} = RTn_c\left(\frac{\phi_A}{N_A}ln\phi_A + \frac{\phi_B}{N_B}ln\phi_B + \chi\phi_A\phi_B\right) \quad (1.7)$$

where n_c is the molar number of the reference units

$$n_c = \frac{V}{v_c} \quad (1.8)$$

And, in case A-structure and B-structure units have the same volume equal to v_c, the degrees of polymerization expressed in terms of the numbers of structure units are

$$N_A = \frac{v_A}{v_c}; \quad N_B = \frac{v_B}{v_c} \tag{1.9}$$

ϕ_A and $\phi_B$add up to unity,

$$\phi_A + \phi_B = 1 \tag{1.10}$$

The equation 1.7 is the notorious and widely used Flory‑Huggins equation. It sets the basis from which the majority of discussions of the properties of polymer mixtures emanate.[4]

In fact, starting from ΔG_{mix}, the entropy of mixing, ΔS_{mix}, follows as

$$\Delta S_{mix} = -\frac{\partial \Delta G_{mix}}{\partial T} = -RV\left(\frac{\phi_A}{N_A} ln\phi_A + \frac{\phi_B}{N_B} ln\phi_B + \frac{\phi_A \phi_B}{v_c}\frac{\partial(\chi T)}{\partial T}\right) \tag{1.11}$$

and the enthalpy of mixing, ΔH_{mix}, as

$$\Delta H_{mix} = \Delta G_{mix} + T\Delta S_{mix} = RT\frac{V}{v_c}\phi_A \phi_B\left(\chi - \frac{\partial(\chi T)}{\partial T}\right) \tag{1.12}$$

These expressions show that the χ -parameter includes an entropic contribution given by

$$\chi_S = \frac{\partial(\chi T)}{\partial T} \tag{1.13}$$

and an enthalpic part

$$\chi_H = -T\frac{\partial \chi}{\partial T} \tag{1.14}$$

both setting up χ as

$$\chi = \chi_S + \chi_H \tag{1.15}$$

The equation (1.13) indicates that for purely enthalpic local interactions, χ must have a temperature dependence

$$\chi \propto \frac{1}{T} \tag{1.16}$$

In this case, the increase in entropy is associated with the translational entropy only,

$$\Delta S_{mix} = \Delta S_t \tag{1.17}$$

and the heat of mixing is given by

$$\Delta H_{mix} = RTn_c \chi \phi_A \phi_B \tag{1.18}$$

Therefore, the Flory–Huggins equation provides the basis for a general discussion of the miscibility properties of a pair of polymers.[4] In general, as a necessary requirement, mixing must be accompanied by a decrease of the Gibbs free energy.

The Flory–Huggins equation shows that for polymer mixtures the increase in the translational entropy ΔS_t is extremely small and vanishes in the limit of infinite molar mass, therefore:

- positive values of χ necessarily lead to incompatibility. Since the entropic part, χ_S, appears to be mostly positive, one may also state that no polymer mixtures exist with a positive heat of mixing.
- If the χ -parameter is negative, then mixing takes place.

The miscibility is mainly dominated by forces acting between the monomers. Hence, mutual compatibility of two polymers, i.e., their potential to form a homogeneous mixture, is almost exclusively determined by the local interactions. Endothermal conditions are the rule between two different polymers, exothermal conditions are the exception. Hence, the majority of pairs of polymers cannot form homogeneous mixtures. Compatibility is only found if there are special interactions between the A-monomers and the B-monomers as they may arise in the form of dipole–dipole forces, hydrogen bonds or special donor–acceptor interactions.[4]

All these conclusions refer to the limit of large degrees of polymerization. It is important to see that the Flory–Huggins equation permits to evaluate how the compatibility changes if the degrees of polymerization are reduced and become moderate or small. In the case of a symmetric mixture with equal degrees of polymerization for both components:

$$N_A = N_B = N \tag{1.19}$$

with

$$\frac{n_c}{N} = n_A + n_B \tag{1.20}$$

We obtain

$$\Delta G_{mix} = RT(n_A + n_B)(\phi_A ln\phi_A + \phi_B ln\phi_B + \chi N\phi_A\phi_B) \tag{1.21}$$

The dependence of ΔG_{mix} on ϕ_A is shown in figure 1.4, as computed for different values of χN.[4] For vanishing χ, one has negative values of ΔG_{mix} for all ϕ_A, with a minimum at ϕ_A = 0.5. In this case, we have perfect miscibility caused by the small entropic forces related with ΔS_t. For negative values of χN, we have a further decrease of ΔG_{mix} and therefore also perfect miscibility. A change in behavior is observed for positive values of χN. The curves alter their shape and for parameters χN above a critical value

$$(\chi N) > (\chi N)_c \tag{1.22}$$

a maximum rather than a minimum emerges at ϕ_A = 0.5. This change leads us into a different situation. Even if ΔG_{mix} is always negative, there a homogeneous mixture

does not always form. To understand the new conditions we can consider, for example, the curve for χN = 2.4 and a blend with ϕ_A = 0.45. There the two arrows are drawn. The first arrow indicates that a homogeneous mixing of A and B would lead to a decrease in the Gibbs free energy, when compared to two separate one component phases. However, as shown by the second arrow, the Gibbs free energy can be further reduced, if again a two-phase structure is formed, now being composed of two mixed phases, with compositions ϕ_A' and ϕ_A''. The specific feature in the selected curve responsible for this peculiar behavior is the occurrence of the two minima at ϕ_A' and ϕ_A'', as these enable the further decrease of the Gibbs free energy.[4]

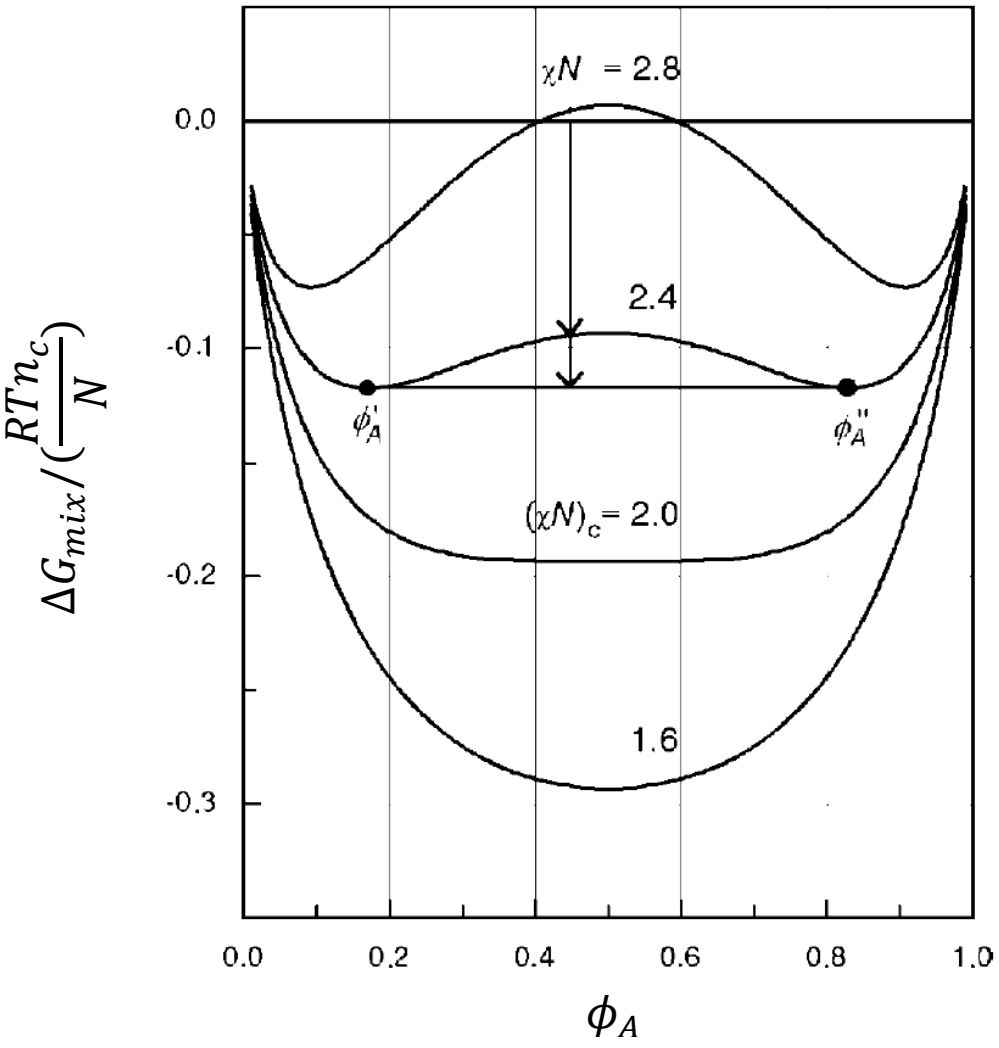

Figure 1.4. Gibbs free energy of mixing of a symmetric binary polymer mixture, as described by the Flory–Huggins equation.[4]

Of course, the overall volume fraction of the A-chains has to be in the range

$$\phi_A' \leq \phi_A \leq \phi_A''$$

Outside this central range, for $\phi_A < \phi_A'$ and $\phi_A > \phi_A''$, a separation into the two-phases with the minimum Gibbs free energies is impossible and one homogeneous phase is formed. For a given ϕ_A it is possible to calculate the fractions ϕ_1, ϕ_2 of the two coexisting mixed phases, in fact

$$\phi_A = \phi_1 \phi_A' + (1 - \phi_1)\phi_A'' \tag{1.23}$$

therefore

$$\phi_1 = \frac{\phi_A'' - \phi_A}{\phi_A'' - \phi_A'} \tag{1.24}$$

and

$$\phi_2 = 1 - \phi_1 = \frac{\phi_A - \phi_A'}{\phi_A'' - \phi_A'} \tag{1.25}$$

Hence in conclusion, for curves ΔG_{mix} (ϕ_A), which exhibit two minima and a maximum in-between, mixing properties depend on the value of ϕ_A. Miscibility is found for low and high values of $\phi_A$only, and in the central region there is a miscibility gap.[4]

It is possible to determine the critical value of χN that separates the range of perfect mixing, i.e., compatibility through all compositions, from the range with a miscibility gap. For the critical value of χN, the curvature at ϕ_A= 0.5 must vanish

$$\frac{\partial^2 \Delta G_{mix}(\,\phi_A = 0.5)}{\partial \phi_A^2} = 0 \tag{1.26}$$

the second derivative of ΔG_{mix} is given by

$$\frac{1}{(n_A + n_B}\frac{\partial^2 \Delta G_{mix}}{\partial \phi_A^2} = \frac{1}{\phi_A} + \frac{1}{1 - \phi_A} - 2\chi N \tag{1.27}$$

The critical value is

$$\chi N = 2 \tag{1.28}$$

Therefore, the mixing occurs for $\chi N < 2$, when we expect full compatibility for

$$\chi < \chi_c = \frac{2}{N} \tag{1.29}$$

and a miscibility gap for

$$\chi > \chi_c \tag{1.30}$$

This last two equations describe the effect of the molar mass on the compatibility of a pair of polymers.[4] In agreement with the previous conclusion, in the limit $N \rightarrow \infty$,

$$\chi_c \rightarrow 0$$

The phase diagram in figure 1.5, summarises the properties of symmetric polymer mixtures. It depicts the two regions associated with homogeneous and two-phase structures in a plot that uses the sample composition as expressed by the volume fraction ϕ_A and the parameter χN as variables. The boundary between the one phase and the two-phase region is called binodal. It is determined by the compositions ϕ'_A and ϕ''_A of the equilibrium phases with minimum Gibbs free energies in the miscibility gap. ϕ'_A and ϕ''_A follow for a given value of χN from[4]

$$\frac{\partial \Delta G_{mix}}{\partial \phi_A} = 0 \qquad (1.31)$$

therefore, we obtain an analytical expression for the binodal

$$\chi N = \frac{1}{1-2\phi_A} ln \frac{1-\phi_A}{\phi_A} \qquad (1.32)$$

The derived phase diagram is universal in the sense that it is valid for all symmetric polymer mixtures. It indicates a miscibility gap for χN > 2 and allows to make a determination of χN in this range if the compositions of the two coexisting phases are known.

The linkages in block copolymers inhibit such a macroscopic phase separation. The A's and B's still segregate but the domains have only mesoscopic dimensions corresponding to the sizes of the single blocks (Figure 1.6). In addition, as all domains have a uniform size, they can be arranged in regular manner. As a result ordered mesoscopic morphologies emerge. In the figure it is also indicated that this microphase separation leads to different classes of structures in dependence on the ratio between the degrees of polymerization of the A's and B's. For $N_A \ll N_B$ spherical inclusions of A in a B-matrix are formed and they set up a body-centered cubic lattice. For larger values N_A, but still $N_A < N_B$, the A-domains have a cylindrical shape and are arranged in a hexagonal lattice. Layered lattices form under essentially symmetrical conditions, i.e., $N_A \approx N_B$. This is the case for the polymer systems object of this Ph.D. thesis, since they are di-block copolymers forming lamellar structures, therefore symmetrical condition are achieved. Then, for $N_A > N_B$, the phases are inverted and the A-blocks now constitute the matrix.[4]

In addition to these morphologies composed of spheres, cylinders and layers, periodic structures occur under special conditions where both phases are continuous and interpenetrate each other. These bicontinuous gyroid structures exist only in a narrow range of values N_A/N_B, between the regimes of the cylindrical and lamellar structures and, as it appears, only when the repulsion forces between the A's and the

B's are not too strong. Spherical, cylindrical and layer-like domains are generally observed in all block copolymers.[4]

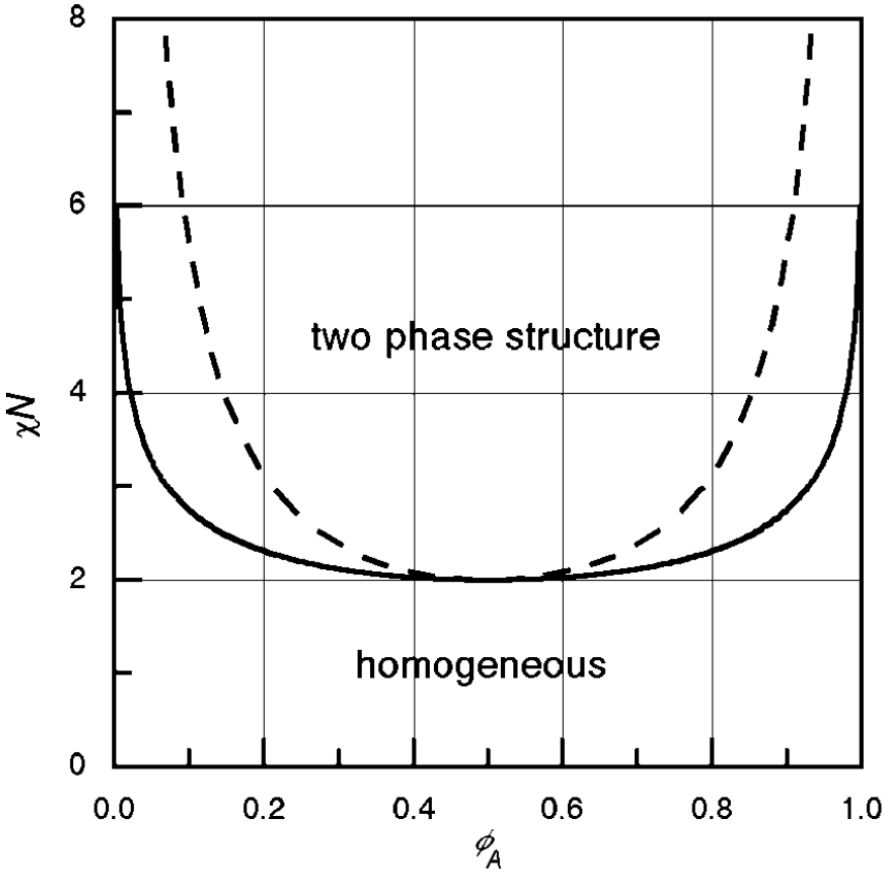

Figure 1.5. Phase diagram of a symmetric polymer mixture. The binodal (continuous line) and the spinodal (broken line) are shown.[4]

The majority of synthesized compounds are di-block copolymers composed of one A-chain and one B-chain; however, tri-blocks and multiblocks, comprising an arbitrary number of A-chains and B-chains, can be prepared as well. Here, we will focus only on the systems studied in this Ph.D. thesis, the di-block copolymers.

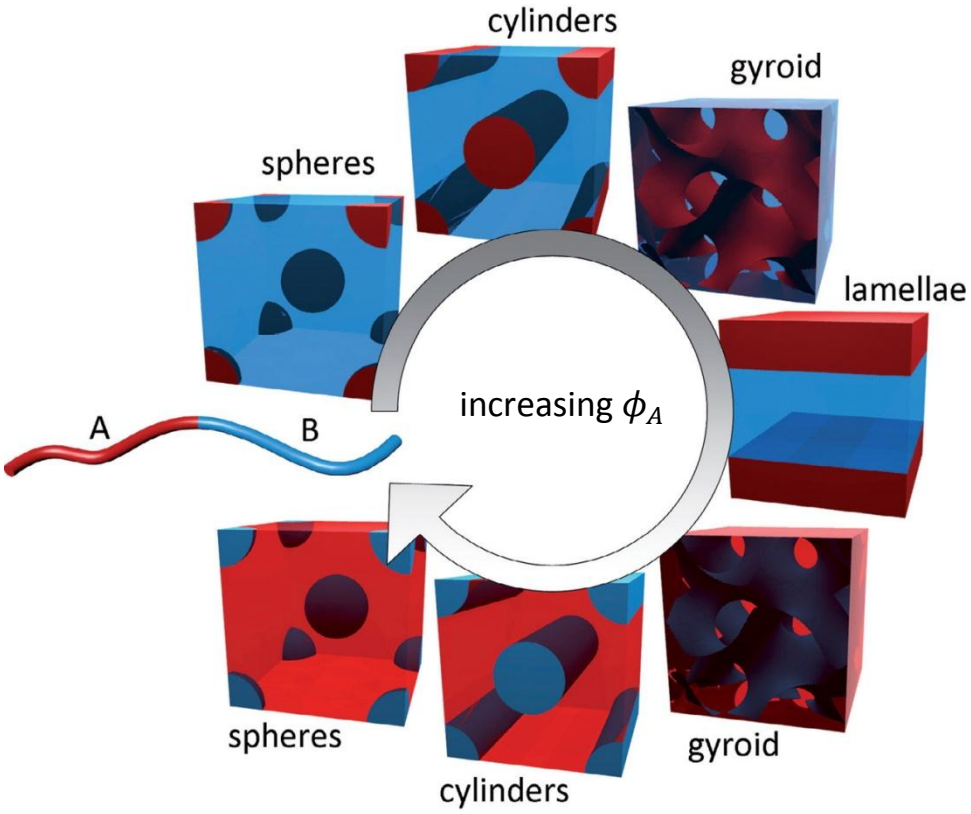

Figure 1.6. Different classes of microphase separated structures in di-block copolymers in the bulk as a function of the volume fraction of one of the blocks (ϕ_A).[5]

A suitable method for the analysis of block copolymer structures is small-angle X-ray scattering (SAXS). Figure 1.7 gives an example of scattering curves obtained for a series of polystyrene-*block*-polyisoprenes, a system very similar to our P(S-*b*-B), where both blocks had similar molar mass. Structures belong to the layer regime and one correspondingly observes series of equidistant Bragg reflections.[4]

As we have previously shown, in binary polymer mixtures, under favorable conditions homogeneous phases are formed. They either arise if the forces between unlike monomers are attractive or, generally, if the molar masses are sufficiently low. Block copolymers behave similarly and can also have a homogeneous phase. It actually has a larger stability range than the corresponding binary mixture.[4] We have previously seen that for a symmetric mixture ($N_A = N_B$) the two-phase region begins at

$$(\chi N_A)_c = 2$$

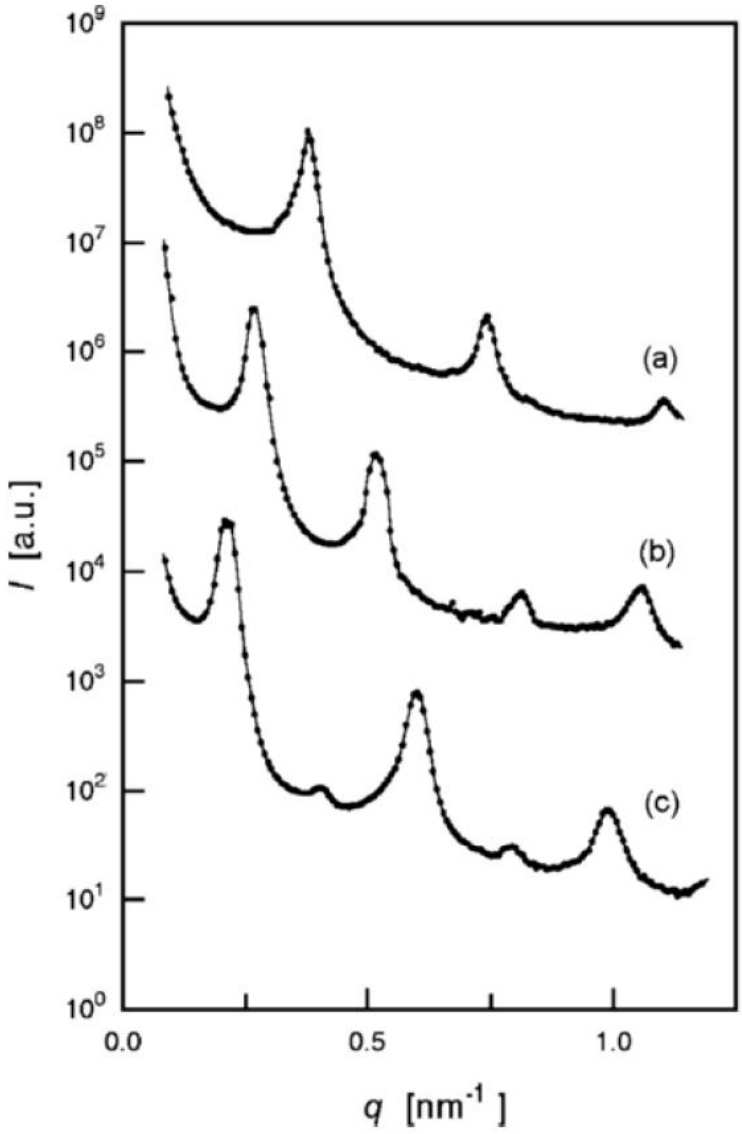

Figure 1.7. SAXS curves measured for a series of PS-*block*-PI with different molar masses in the microphase separated state: (a) M = 2.1×10^4 g mol^{-1}, ϕ(PS) = 0.53; (b) M = 3.1 ×10^4 g mol^{-1}, ϕ(PS) = 0.40; (c) M = 4.9 ×10^4 g mol^{-1}, ϕ(PS) = 0.45.[6]

If a symmetric di-block copolymer is formed from the same A- and B-chains, the transition between the homogeneous phase and the microphase separated state takes place at a higher χ, namely for

$$(\chi(N_A + N_B))_c \approx 10 \tag{1.33}$$

The complete phase diagram of a block copolymer is displayed in Figure 1.8 in a schematic representation.[4] Variables are the volume fraction of the A-blocks

$$\phi_A = \frac{N_A}{N_A + N_B} \tag{1.34}$$

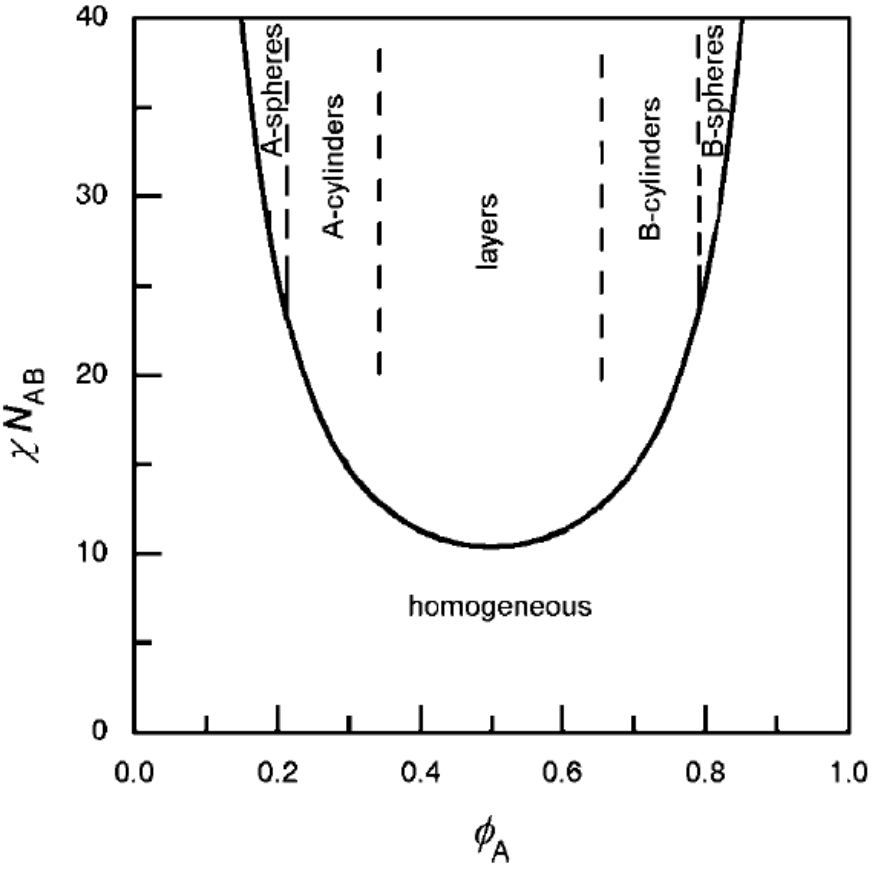

Figure 1.8. Phase diagram of a di-block copolymer in a schematic representation. The curve describes the points of transition between the homogeneous phase and the microphase separated states. The ordered states comprise different morphologies as indicated by the dashed boundary lines.[4]

and the product χN_{AB}, where N_{AB} describes the total degree of polymerization

$$N_{AB} = N_A + N_B$$

The transition line separating the homogeneous phase from the various microphase separated structures has an appearance similar to the binodal of a polymer mixture. There is, however, a basic difference: in the block copolymer case, we are dealing with a one component system rather than a binary mixture. The line therefore relates

to a phase transition rather than to a miscibility gap. It should also be noted that, in contrast to the binodal of a mixture, the transition line tells us nothing about the internal composition of the microphases. In principle, these could be mixed states; however, with the exception of situations near the transition line, compositions are mostly close to pure A- or B-states. The schematic drawing indicates only the structures arising under the conditions of a strong segregation, $\chi N_{AB} \gg 10$, where solely lattices of spheres, cylinders and layers are found. The situation for a weak segregation with χN_{AB} just above the critical value is more complicated. Here, also the bicontinuous structures are found and subtle features decide about their stability relative to the three major morphologies.[4]

Each of the ordered structures represents under the respective conditions the state with the lowest Gibbs free energy. Calculations of the Gibbs free energies and comparisons between the various lattices and the homogeneous phase can therefore provide an understanding of the phase diagram. In addition, they make it possible to determine the structural parameters.[4]

Theoretical analyses were carried out by Meier and Helfand. We will apply the theoretical framework to the case of layered structures, in order to highlight the theoretical background behind lamellar di-block copolymer systems studied in this Ph.D. thesis and discuss the equilibrium conditions. The main result will be a power law that formulates the dependence of the layer thicknesses on the degree of polymerization of the blocks.[4]

The structural changes that accompany a transition from the homogeneous phase to an ordered layer structure are dominated by three contributions to the change in the Gibbs free energy

$$\Delta g_p = \Delta h_p - T\Delta s_{p,if} - T\Delta s_{p,conf} \tag{1.35}$$

The driving force for the transitions comes from the enthalpic part. In the usual case of unfavorable AB-interactions, i.e., $\chi > 0$, there is a gain in enthalpy on unmixing. We assume a maximum gain, achieved when we have a random distribution of the monomers in the homogeneous phase and a perfect segregation in the lamellar phase. Then the enthalpy change per polymer, Δh_p, is given by[4]

$$\Delta h_p = -kT\chi N_{AB}\phi_A(1-\phi_A) + \Delta h_{p,if} \tag{1.36}$$

where $\Delta h_{p,if}$, accounts for an excess enthalpy that is contributed by the interfaces. The interfaces always have a finite thickness, typically in the order of one to several nm. Within this transition layer the A's and B's remain mixed, which leads to an increase in enthalpy proportional to χ and to the number of structure units in the transition layer.[4] Let the thickness of the transition layer be D_t and the interface area per polymer o_p, then we may write

$$\Delta h_{p,if} \cong kT\chi\frac{o_p D_t}{v_c}$$

with v_c the volume of the structure unit, commonly chosen for both the A- and B-chains.

The two entropic parts both work in the opposite direction. There is first the loss in entropy, which results from the confinement of the junction points, being localized in the transition layer. For a layered phase with layer thicknesses D_A and D_B, and therefore a period[4]

$$D_{AB} = D_A + D_B \tag{1.37}$$

$\Delta s_{p,if}$ may be, therefore, estimated using a standard equation of statistical thermodynamics

$$\Delta s_{p,if} \cong kln\frac{D_t}{D_A+D_B} \tag{1.38}$$

The second entropic contribution, $\Delta s_{p,conf}$, accounts for a decrease in entropy, which follows from a change in the chain conformations. The Gaussian conformational distribution found in the homogeneous phase cannot be maintained in the microphase separated state. Formation of a layer structure leads necessarily to a chain stretching, which in turn results in a loss in entropy.[4]

It is, therefore, possible to search for the equilibrium, which results in

$$D_{AB}^3 \propto \chi D_t v_c^{2/3} N_{AB}^2 \tag{1.39}$$

For the homogeneous phase of block copolymers the concentration fluctuations increase with an approaching of the point of unmixing. Scattering functions under variation of the temperature exhibit a peak, with an intensity that strongly increases when the temperature moves towards the transition point. As scattering curves display the squared amplitudes of wave-like concentration fluctuations, in case of block copolymers concentration fluctuations with wavevectors in the range $|k| \approx q_{max}$ are always large compared to all the others and show a particularly strong increase on approaching the phase transition, with q_{max} being the finite scattering vector corresponding to the maximum of the scattering intensity. In general the forward scattering, $S(q \to 0)$, always relates to the fluctuation of the number of particles in a fixed macroscopic volume. For block copolymers, this refers to both the A's and the B's. The strict coupling between A- and B-chains in the block copolymers completely suppresses number fluctuations on length scales that are large compared to the size of the block copolymer. For large q's, instead, asymptotically the scattering law of ideal chains, $S(q) \propto 1/q^2$, shows up again in the case of a block copolymer. Both increases together produce a peak, located at a certain finite q_{max}.[4]

The increase of the intensity with decreasing temperature reflects a growing tendency for associations of the junction points accompanied by some short-ranged segregation. As long as this tendency is not too strong, this could possibly occur without affecting the chain conformations, i.e., chains could still maintain Gaussian properties. Therefore the scattering function can be calculated explicitly.[4] Leibler and others derived the following expression for the scattering function per structure unit S_c:

$$\frac{1}{S_c(q)} = \frac{1}{S_c^0(q)} - 2\chi \tag{1.40}$$

with $S_c^0(q)$, the scattering function in the athermal case.[31] This last equation describes the effect of χ directly, which formulates a critical transition with a continuous passage from the homogeneous to the ordered phase. Here the order parameter is associated with the amplitudes of the concentration waves with $|k| = q_{max}$. In general it is possible to calculate the critical values for all ϕ's. In particular, for a symmetric block copolymer[4]

$$\chi N_{AB} = 10.5$$

which is the lowest possible value, as mentioned in the equation 1.33.

Therefore, for small χN, close to the order-to-disorder transition ($\chi N_{ODT} = 10.5$), the composition profile (density of either component) is approximately sinusoidal. This is termed the weak-segregation limit. At much larger values of χN ($\chi N > 100$), the components are strongly segregated and each domain is almost pure, with a narrow interphase between them. This is the strong-segregation limit.[7]

Lately, a powerful new method to solve the self-consistent field equations for block copolymers has been applied by Matsen and coworkers to analyse the ordering of many types of block copolymer in bulk and in thin films. The strong- and weak-segregation limits are spanned, as well as the intermediate regime where the other methods do not apply. This implementation of the self-consistent field (SCF) theory, where the external mean fields acting on a polymer chain are calculated self-consistently with the composition profile, predicts phase diagrams, and other quantities such as domain spacings, in good agreement with experiment (Figure 1.9) and represents a strong reference for modelling the ordering of soft materials.[7]

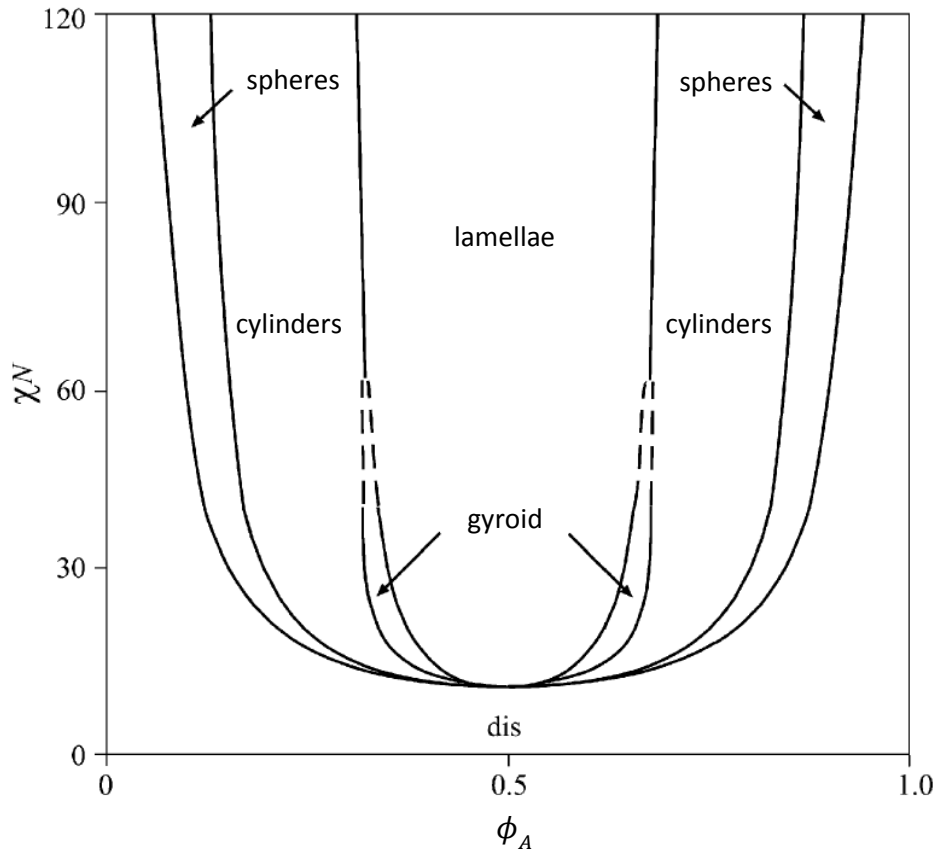

Figure 1.9. Phase diagram for a conformationally symmetric di-block copolymer, calculated using self-consistent mean field theory. In the phase diagram, regions of stability of disordered (dis), lamellar, gyroid, hexagonal (cylinders) and body-centred cubic (spheres) phases are indicated.[7]

1.3 Block copolymer thin films

BCP microphase separation has been the focus of intense research activity. These efforts have produced a solid foundation of theoretical and experimental understanding of the rich behavior of these systems and provided insight into how this spontaneous nanoscopic structure formation might be harnessed for use in a variety of technological applications. While the majority of this work has concentrated upon bulk systems, more recent efforts have striven to understand BCP microphase separation in thin films. This latter research has, in large part, been concerned with

the understanding and emphasizing of the enhanced role of surface/interfacial energetics, as well as the interplay between the copolymer's characteristic length scale, D_{AB}, and the film thickness, D_{film}, in dictating film structure. Indeed, as film thickness decreases, these effects become increasingly consequential.[3] The behavior of amorphous block copolymers (BCPs) in thin films depends on a combination of segmental interactions, interfacial interactions, surface energies and entropy, where the commensurability between the film thickness and the natural period of the microdomains in the bulk is also of importance.[8]

As previously discussed, at temperatures below the order-to-disorder transition temperature, T_{ODT}, BCPs microphase separate into arrays of spherical, cylindrical, gyroid or lamellar microdomains, depending on the volume fractions of the blocks, ϕ, and the degree of microphase separation, χN, where χ is the Flory-Huggins segmental interaction parameter and N is the total number of segments in BCPs. Above the T_{ODT}, BCPs phase mix and are disordered.[8]

The self-assembly of BCPs into well-defined morphologies has opened numerous applications ranging from drug delivery to structural materials. In contrast to the bulk, the morphology of amorphous BCP thin films can be strongly influenced by surface and interfacial energies as well as the commensurability between the D_{film} and D_{AB} (Figure 1.10). With decreasing film thickness these parameters become increasingly important in defining the morphology. Nanostructures in block copolymer films can be oriented using electric fields (if the difference in dielectric permittivity is sufficient), thermal treatment and solvent vapour treatment. Indeed, thermal and solvent vapour annealing has been employed in order to achieve a long-range ordering for the systems studied in this Ph.D. thesis. By controlling the orientation and lateral ordering the BCP microdomains in thin films, unique opportunities in the use of BCPs in materials science (adhesive properties, lubrication, membranes, and coatings), lithography and microfabrication (addressable memory, magnetic storage, insulating foams) and device technologies (light-emitting diodes, photodiodes, and transistors) are beginning to emerge.[8]

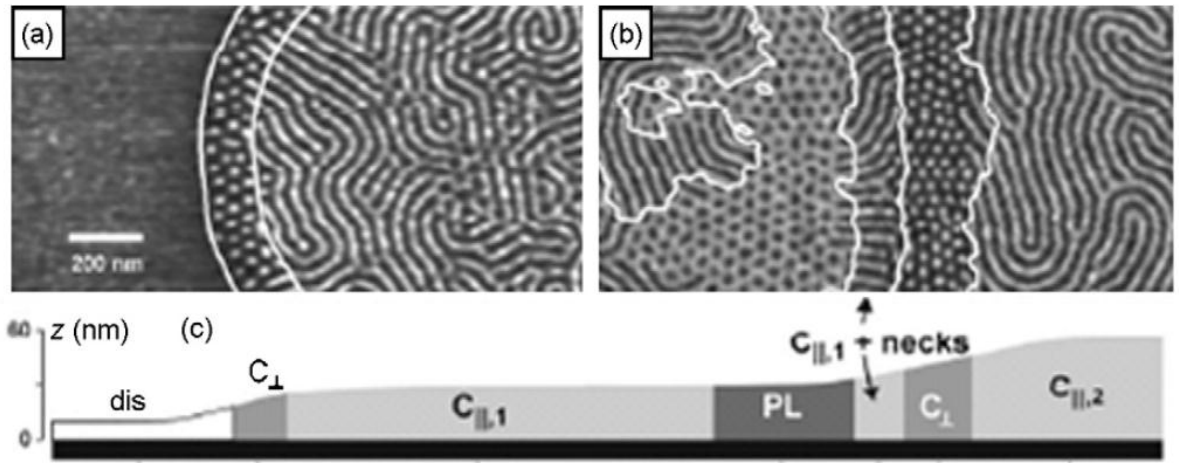

Figure 1.10. (a and b) Tapping mode AFM images (phase contrast) of a PS–PB–PS triblock after solvent annealing. Different structures are delineated with white lines, and correspond to regions of different film thickness. (c) Schematic height profile. $C_{\perp}$ and $C_{||}$ denote cylinders perpendicular or parallel respectively to the substrate, and PL denotes perforated lamellae[9].

In contrast to the bulk BCP morphologies, BCP thin films are often characterized by highly oriented domains. This orientation is a direct result of surface and interfacial energy minimization, as illustrated by a film of a bulk-lamellar di-block with block segments denoted A and B bounded by surfaces 1 and 2 shown in figure 1.11a,b. The overriding trend exhibited by films of thickness $D_{film} > D_{AB}$ is full lamellae oriented parallel to the film and substrate surfaces as shown in figure 1.11c (FL).[3]

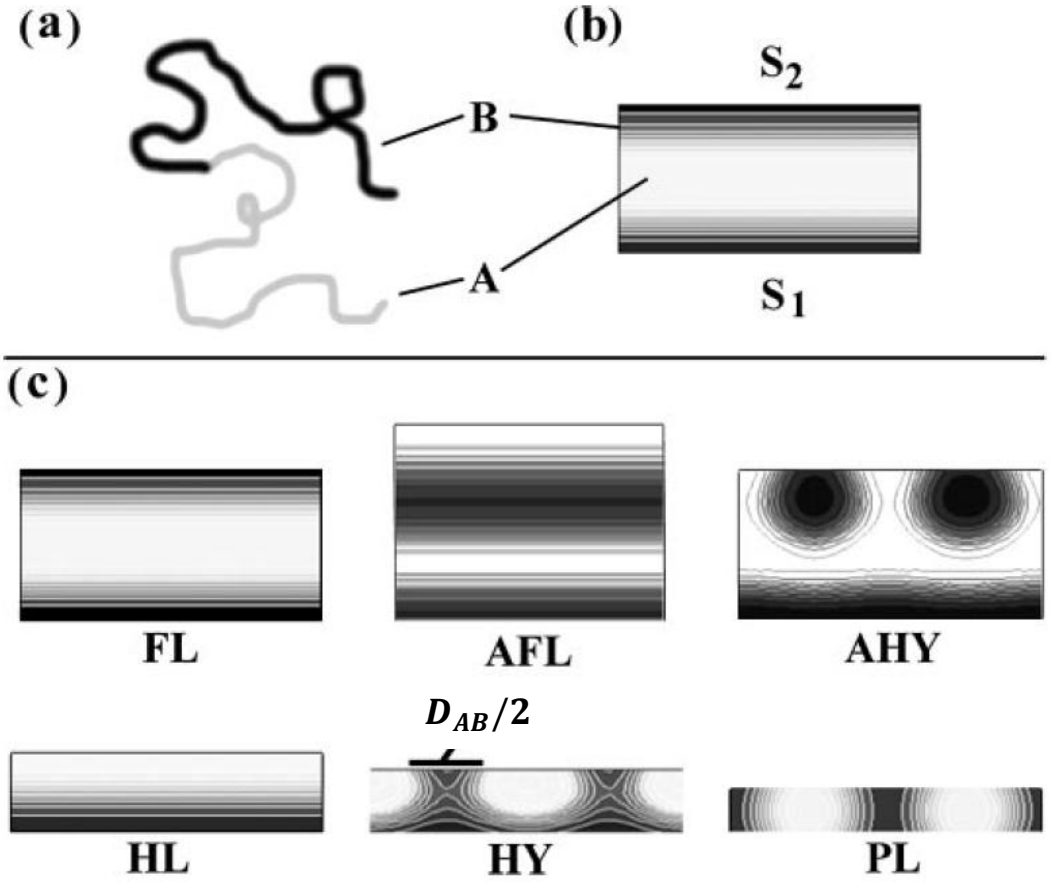

Figure 1.11. Di-block copolymer thin film morphologies. (a) Schematic representation of volume symmetric di-block with A (light) and B (dark) type segments. (b) Diagram of BCP film system in cross section indicating the bottom (1) and top (2) surfaces, with surface interaction energies S_1 and S_2, respectively. (c) Summary of di-block thin film morphologies, generally organized by their appearance as film thickness decreases from D_{AB}. These calculated cross sections indicate the density of B-type segments, i.e., Black = 100% B, white = 100% A. These structures are referred to in the text with the abbreviations included under each diagram. FL: symmetric surface-parallel full lamella; AFL: anti-symmetric surface-parallel lamella; AHY: anti-symmetric hybrid structure; HL: half-lamella; HY: symmetric hybrid structure; PL: surface-perpendicular lamellae.[3]

This morphology develops through the surface and substrate boundary conditions that demand the most energetically compatible block be expressed at each of the surfaces. These surface-parallel lamellae also optimize the interfacial energetics of the system by minimizing the amount of A/B interface while maintaining D_{AB}

periodicity. By convention, if the same block, for example B, is found at each boundary, the copolymer is said to exhibit symmetric wetting. Alternately, BCP films that express different blocks at each surface are termed antisymmetric (Figure 1.11c, AFL). At equilibrium, symmetric film systems exhibit a series of stable films when $D_{film} = mD_{AB}$ (m = 1, 2, 3, 4), whereas anti-symmetric films exhibit a similar series of stable films when $D_{film} = (m + 1/2)D_{AB}$.[3]

The wetting and domain orientation a given BCP exhibits depends upon the energetic/chemical nature of the surfaces that bound the film, i.e., the magnitude and type of interaction (attraction/repulsion) these boundaries have with each of the block species. Surface boundary energetics can be classified into two general categories: symmetric boundary conditions, in which the energetics imposed by each surface is identical, and asymmetric boundary conditions consisting of surfaces with different energetic qualities.[3] In order to describe the theoretical background behind the research presented in this Ph.D. thesis, we will focus on the asymmetric boundary conditions, which are related to substrate-supported films.

Although identical film surface boundaries simplify some analyses, many film systems involve asymmetric boundary conditions, i.e., where the block-segment/ surface interactions, S_1 and S_2, are different in strength and/or sign. This is certainly the case for substrate-supported films that form the majority of technologically relevant and experimentally tractable specimens. In supported film systems, the surface energy of a given monomer can differ from its substrate interfacial energy by an order of magnitude. Furthermore, the presence of asymmetric boundary conditions can result in specific morphological trends (for example, the formation of hybrid morphologies that combine surface-parallel and surface-perpendicular components, which will be then of importance for discussing the results presented in this Ph.D. thesis) that cannot be accounted for with symmetric surface energetics. Accordingly, the understanding of substrate-supported films requires analysis that explicitly includes boundary condition asymmetry.[3]

Several published studies have employed asymmetrical boundary condition in analytical and computational analyses of the morphology of volume-symmetric di-block copolymers. Walton *et al*[10] included this case in their analysis of lamellar domain orientation and defined conditions for the stability of the PL morphology analogous to that supplied for symmetric boundary conditions. Matsen also considered this case using SCF methods[11]. This latter work centered generally on film thicknesses greater than D_{AB}. Mixed-orientation morphologies were included in the analysis, making possible predictions comparable to recent observations of such structures by Huang et al[12] in this thickness regime. However, Matsen's conclusion was that these hybrid forms are metastable. In contrast, another recent study by Tang[13] considered the case of D_{AB}-thick films under asymmetric boundary conditions. While that work did not consider thickness effects, it succeeded in demonstrating the stability of a particular hybrid morphology (AHY in figure 1.11c), which had been

observed in the PS/PMMA system via transmission electron microscopy (TEM) by Morkved and Jaeger[14] and inferred from reflectivity measurements by Russell *et al*[15]. Tang's study also predicts a number of new morphologies that have yet to be observed. Fasolka *et al* completed a comprehensive SCF analysis of the morphological behavior of compositionally symmetric, substrate-supported di-block films in the thickness regime $D_{film} \leq D_{AB}$.[3]

1.4 The Glass Transition Temperature

The transition from the glassy to the liquid state is a purely kinetical phenomenon. The temperature, where the transition from a liquid equilibrium state to a non-ergodic one, i.e., only partially equilibrated state takes place, is called the glass transition temperature, with the general designation T_g.[4]

The T_g can be highlighted in various ways. However, two of the methods are of special importance and are used in the majority of cases. These are temperature-dependent measurements of the expansion coefficient or the heat capacity of a sample, carried out during heating or cooling runs. They need only small amounts of material, and standard equipment is commercially available. The glass transition has a characteristic signature that shows up in the curves of a volumetric and a calorimetric measurement. In fact, the transition is associated with steps in the expansion coefficient and the heat capacity.[4]

It is important to understand the cause for the occurrence of the steps in the heat capacity and the expansion coefficient. Cooling a sample below T_g results in a freezing of the modes of movement. The observations tell us that the modes of movements affect not only the shape of a sample, but also its volume and its enthalpy. In fact, if segments move, they produce an additional volume in their neighborhoods. In the literature, this is often called a free volume in order to stress that it is not occupied by the monomers. The free volume increases with temperature because motions intensify, therefore, the jump rates increase and, more importantly, a growing number of conformational states become populated and not all of them allow a dense chain packing. Therefore, when on crossing T_g from low temperatures the modes of movement become active, beginning slowly and then steadily increasing in intensity, a growing additional free volume correspondingly arises. Thermal expansion in the glass is due to the anharmonicity of vibrational motions, as in crystalline solids. The modes of movement contribute another, even larger part to

the expansion coefficient and it comes into effect at T_g. Moreover, as the free volume incorporates energy, changes in the volume and in the enthalpy are interrelated and this results in simultaneous steps in the expansion coefficient and the heat capacity.[4]

The location of the step in the expansion coefficient or the heat capacity, observed during a cooling run, depends on the cooling rate. Analyzing this dependence in more detail allows to derive a criterion for the position of the glass transition. In the fluid state, all degrees of freedom equilibrate rapidly so that thermal equilibrium is always maintained. Conditions change on approaching the glass transition since, here, the relaxation times of the modes of movement reach values that are too high to further allow for a continuous equilibration. Vibrations and local modes still react immediately to temperature changes but the modes of movement are far less reactive. Finally, after having crossed the transition range, the energy exchange between the instantaneously reacting modes and the modes of movement stops completely.[4]

The change from a non-equilibrium value of the enthalpy associated with the modes of movement, ΔH, to the equilibrium value, ΔH_{eq}, occurs with a temperature-dependent rate τ^{-1}. Using the Vogel–Fulcher law, we obtain that T_g is reached during a cooling run when the relative change of the relaxation rate τ^{-1} within a time in the order of τ is no longer negligible[4]. If the cooling rate is increased, the step in the calorimetric measurement and the volumetric experiment occurs at an even shorter relaxation time τ, and therefore at higher temperatures.[4]

To show some typical values in the case of block copolymers, table 1.1 collects the T_g's of several samples made of poly(styrene-*b*-butadiene) with different overall molar masses[16].

M_N^{stoich} [g/mol]	M_{PS}^{stoich} [g/mol]	T_g^{PS} °C	ODT °C	T_{g1} °C	T_{g2} °C
9200	5000	80	-21 ± 10^a	-78	–
18300	9900	90	130 ± 2	-88	–
18500	10000	90	145.5 ± 2	-89	–
22100	11900	92	181 ± 2	-89	76
54500	29700	97	204 ± 2	-91	102

Table 1.1. Results from Differential Scanning Calorimetry (DSC) measurement on different samples of poly(styrene-*b*-butadiene). Columns from left to right: the overall molar mass, the molar mass of the polystyrene blocks, the glass temperature of pure polystyrene having the same molar mass as the polystyrene block, the T_{ODT} of the block copolymer and the glass temperatures for PB and PS, respectively, measured by means of DSC.[16]

In the case of block copolymers it is crucial to notice that the two blocks can have different T_g's. In fact, in the case of the P(S-*b*-B) studied in this Ph.D. thesis, the T_g(PB) is far below ambient temperature, meanwhile for polystyrene, which is glassy at room temperature, the T_g is located between 80 and 100°C, depending on the molar mass of the polystyrene blocks.

Also quite useful are mixing rules, which describe the T_g-values of blends as a function of the T_g's of the components in pure states and their volume fractions. As it turns out, in many cases a good representation is achieved by the Fox–Flory equation, given by[4]

$$\frac{1}{T_g} = \frac{\phi_A}{T_g^A} + \frac{\phi_B}{T_g^B} \tag{1.41}$$

In this Ph.D. thesis thermal treatment has been adopted as one of the methods capable of anneal defects in spin-coated films, promoting a long-range ordering of the di-block copolymer thin films. The fundamental role of T_g has been highlighted, with particular reference to the behavior of the blocks which at room temperature are in the glassy state (PS, in this study).

1.5 Solvent

Block copolymer films can be prepared by the spin-coating technique, which has also been employed for preparing the films studied in this Ph.D. thesis, where drops of a solution of the polymer in a volatile organic solvent are deposited on a solid substrate (often silicon wafers are used due to their uniform flatness), spinning it to obtain an homogenous thin film. The polymer film spreads by centrifugal forces, and the volatile solvent is rapidly driven off. With care, the method can give films with a low surface roughness over areas of square millimetres. The film thickness can be controlled through the spin speed, the concentration of the block copolymer solution or the volatility of the solvent, which also influences the surface roughness.[7]

Solvent evaporation under controlled conditions can provide a strong directional field to orient block copolymer film nanostructures. A high degree of lateral order with few defects can be achieved. This results from the propagation of ordering from the surface into the film. It may also enable ordered structures to develop more rapidly, although equilibrium morphologies may not be accessed without further annealing.[17] Krausch and co-workers showed that the solvent (THF) evaporation rate could be used to change the orientation of lamellae formed by a PS-P2VP-PtBMA tri-block copolymer[18]. Parallel lamellae were observed for low evaporation rates, and perpendicular lamellae for high evaporation rates. In a subsequent paper, the propagation of lamellar order from the free surface and expulsion of defects to the vicinity of the substrate was monitored via ex situ cross-sectional TEM[19].[17]

Russell and co-workers have applied the solvent annealing technique very successfully to PS-PEO films annealed in benzene vapour[20]. Grazing-incidence small-angle X-ray scattering (GISAXS) has been used to probe the development of ordering and the perfection of the hexagonal structure has been quantified via triangulation algorithms. For PS–PEO di-blocks, environment-controlled spin-coating in a mixed solvent atmosphere of toluene and water leads to well-developed perpendicular PEO cylinder orientation[21]. Toluene is a selective solvent for PS, whereas water is selective for PEO. Perpendicular orientation was favoured in the presence of a mixture of solvents selective for each block.[17] Of course, trapped solvent may also play a role in the structural ordering of block copolymer thin films.

The process of solvent uptake in lamellar P(S-*b*-B) films has more recently been probed by in situ GISAXS[22]. This shows initial linear swelling, followed by buckling instability followed by re-equilibration into a new lamellar structure.[17]

Annealing in selective solvents can lead to non-equilibrium structures in PS-PMMA di-blocks[23]. Annealing of either a symmetric or an asymmetric sample in a selective solvent for PMMA (acetone) created initial hexagonally-packed sphere structures, which upon further exposure to solvent developed into the expected stripe patterns

resulting from lamellar or cylinder structures. The non-equilibrium hexagonal structures were trapped by vitrification at room temperature. Annealing in different solvents was used to switch from parallel to perpendicular cylindrical P4VP + HABA domain orientation and vice versa in thin films of PS-P4VP complexed with (hydroxybenzeneazo)benzoic acid (HABA) [24]. Swelling in dioxane even led to a transition to a spherical morphology.[17]

For the polymer systems studied in this Ph.D. thesis, solvent annealing has been employed in order to obtain a long-range order of the nanostructures in block copolymer thin films. The uptake of solvent induces three major changes in the block copolymer films: a decreasing of the glass transition temperature of the polymer blocks and in particular for the PS block, glassy at room temperature; the χ parameter is replaced by a $\chi_{effective}$ (since now also the solvent volume fraction has now to be taken into account), which is reduced during the solvent uptake; this induce a decreasing of the enthalpic penalty for the creation of additional lamellae, since the screening effect of thee solvent induces the copolymers to assume more coiled molecular conformation.[25] The selectivity of the solvent plays an important role too, since it affects the swelling process inducing asymmetry in the swelling of different blocks, which are differently selective to the solvent chosen.

Bercea and Wolf report on the effect of solvent vapour treatment on the glass transition temperature of the PS block in presence of a mixture of PS and cyclohexane[26]. They prepared polymer films of 100 µm thickness made of PS with two different molecular weight, 110 and 184 kg/mol. The selected solvents were toluene (TL), good solvent for polystyrene, and cyclohexane (CHX), theta solvent for polystyrene. The plasticizing action of cyclohexane and of toluene is represented within the diagram in figure 1.12. Within the region of high volume fractions of the polymer the reduction of T_g does practically not vary with solvent power. In the case of cyclohexane T_g becomes independent of composition upon dilutions at $\phi < 0.62$ and assumes a value of approximately 7°C, whereas it keeps falling for toluene. This finding is typical for theta solvents and caused by the coexistence of a polymer rich and a polymer lean phase. These results are in qualitative agreement with literature reports concerning other systems.[26]

Upon uptake of solvent the PS glass transition is reached, crossing this value the copolymer mobility increases, thereby allowing a large-scale structural rearrangement within the whole film thickness. This is of crucial importance for the present Ph.D. thesis, since polymer mobility is the key parameter which then induces a reordering of the lamellar structures inducing the achievement of a long-range order.

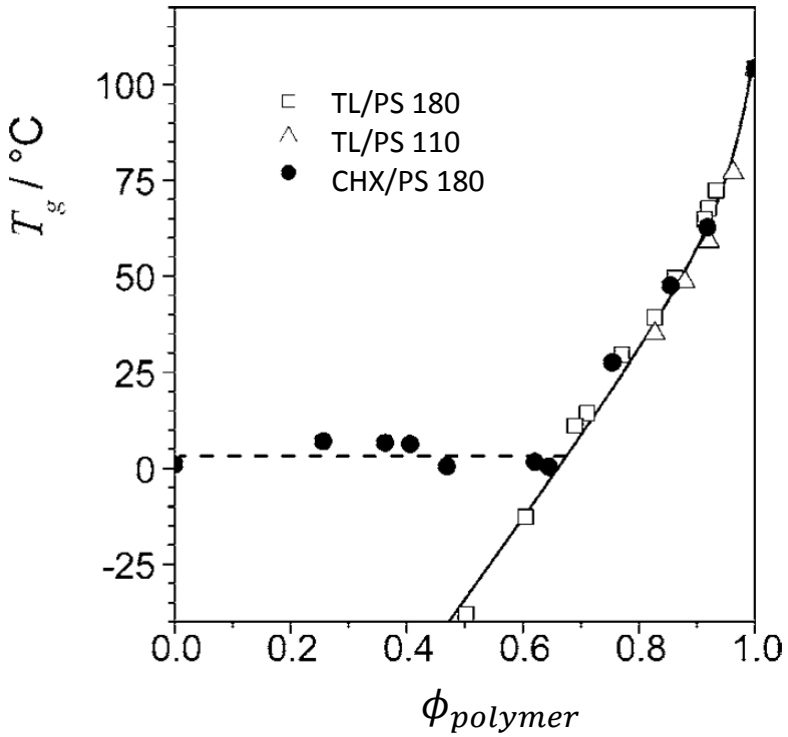

Figure 1.12. Glass transition temperatures, T_g, as a function of the volume fraction of polymer, ϕ, for the thermodynamically good solvent toluene and for the theta solvent cyclohexane. Under isothermal conditions the solutions solidify upon an augmentation of the polymer concentration at the characteristic volume fraction.[26]

Following the uptake of solvent in block copolymer thin films, we observe not only a decrease of T_g, but also the effective Flory-Huggins segment-segment interaction parameter between the two blocks decreases, since now the solvent is screening the repulsive interaction between the blocks. This has to be taken into account when evaluating an eventual order-disorder transition, which can be then crossed by decreasing χN and, moreover, it can occur at higher for χN than 10.5, as predicted by fluctuation theory in the case of low molar mass[27]. In presence of non-selective or slightly selective solvent, within the dilution approximation, the conventional χN of the copolymer is substituted by $\chi_{effective}N$, where $\chi_{effective} = \phi_{polymer}\chi$.[28]

During the solvent uptake, uniaxial swelling of the block copolymer thin film can occur, meanwhile the interfacial area per chain stay constant. Upon an increased polymer mobility, due to the the T_g of the glassy blocks be reached, the lamellae deswell because the copolymers adopt a more coiled molecular conformation. This process induces an undulation in the lamellar interfaces, therefore additional lamellae are created due to the increasing of the interfacial area per chain.[25]

Many thermodynamic properties of polymer solutions such as solubilities and swelling equilibria can be expressed in terms of the unitless polymer-solvent interaction parameter χ_{ps}, which is the exchange interaction parameter in the lattice model of polymer solutions developed by Flory and Huggins. In their definition, the quantity $kT\chi_{ps}$ is the average change in energy when a solvent molecule is transferred from pure solvent to pure, amorphous polymer.[29] However, often χ_{ps} for most systems is defined empirically, and expressed in fuction of the temperature as

$$\chi = \frac{A}{T} + B \tag{1.42}$$

an typical interpretation is that *A* represents an entropic quantity due to non-random segment packing and *B* an enthalpic contribution. Moreover χ_{ps} is found to be dependent on the concentration of the polymer. The important role of solvent selectivity and volume fraction of the polymer on χ_{ps} has been experimentally extensively studied[30]: in case of good solvents it has been observed that χ_{ps} follows the original Flory-Huggins theory, since it is independent from the polymer concentration; instead the dependence on the polymer concentration becomes crucial in the case of poor solvents, where χ_{ps} drastically increases with the polymer concentration; moreover, it has been observed that χ_{ps} decreases with concentration in presence of highly exothermal systems.

Chapter 2

Sample preparation and characterisation

2.1 Poly(styrene-*b*-1,4-butadiene)

A poly(styrene-*b*-butadiene), P(S-*b*-B), di-block copolymer (Figure 2.1), synthetized by Polymer Source, Inc. in Canada, having a molar mass of 216 kg/mol with a PB volume fraction of 0.52 and a polydispersity (PDI) of 1.06 was investigated during thermal treatment. In the following section it will be referred as SB216. Poly(styrene-*b*-butadiene) rich in 1,4 addition polybutadiene is prepared by living anionic polymerization with sequence addition of styrene followed by butadiene in an apolar solvent. The Flory-Huggins segment-segment interaction parameter is $\chi = A/T + B$ with A = 21.6 ± 2.1 K and B = -0.019 ± 0.005.[16] Using these values, the order-to-disorder transition temperature (T_{ODT}) of the block copolymer as estimated from the mean-field prediction, $(\chi N)_{ODT} = 10.5$,[31] where N = 3500 is the overall degree of polymerization of the block copolymer, is above 700°C, i.e. far above the treatment temperatures used. The glass transition temperature of the PS blocks for the block molar masses of the present copolymers is T_g(PS) ≅ 102°C,[16] whereas the one of the PB homopolymer is below –80°C.[32] The surface tensions are γ_c = 28 mN/m for PB and 33 mN/m for PS, respectively[33].

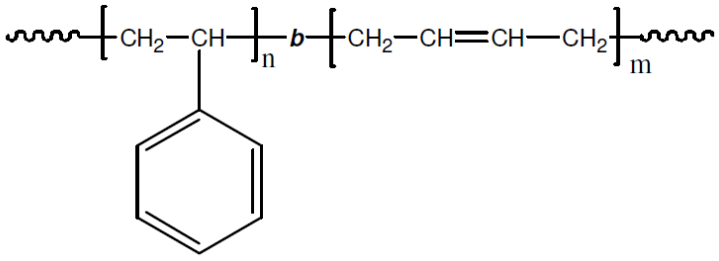

Figure 2.1. Chemical structure of P(S-*b*-B).

During solvent vapour treatment, a P(S-*b*-B) di-block copolymer, also synthetized by Polymer Source, Inc. in Canada with the same procedure described above, having a molar mass of 28.0 kg/mol (15.0 kg and 13.0 kg for PS and PB, respectively), which corresponds to a degree of polymerization N = 474, was used. In the following sections it will be referred as SB28. Its polydispersity index is 1.05 and the PB volume fraction 0.51 ± 0.01. The Flory–Huggins segment–segment interaction parameter of P(S-*b*-B) is also in this case $\chi = A/T + B$ with A = 21.6 ± 2.1 K and B = −0.019 ± 0.005[16]. Using these values, the order-to-disorder transition temperature of the block copolymer as estimated from the mean-field prediction[31] is 250°C. At room temperature, $\chi N \cong 25$, the sample is thus in the intermediate segregation regime.[34]

2.2 Poly(4-octylstyrene-*b*-butylmethacrylate)

A poly(4-octylstyrene-*b*-butylmethacrylate) (P(OS-*b*-BMA)) di-block copolymer was studied during solvent vapour treatment. In the following sections it will be referred as OB5. The di-block copolymer was prepared by sequential living anionic copolymerization in argon atmosphere[1]. The overall molar mass is 35 600 g/mol and the styrene content 62 wt.-%. In bulk, it forms the lamellar morphology with a lamellar thickness D_{lam}^{bulk} = 260 Å, as determined using SAXS on a thermo-annealed sample. The glass transition temperatures of the homopolymers are -40°C for POS and 30°C for PBMA[1].

2.3 Film preparation

In the case of the SB216 Si(100) wafers (Silchem Handelgesellschaft mbH) were precleaned for 15 min at 35°C in a dichloromethane bath and for 15 min at 80°C in an acid bath consisting of 100 ml of 80% H_2SO_4, 35 ml of 30 % H_2O_2, and 15 ml of deionized water, followed by rinsing in deionized water and drying with compressed oil-free nitrogen. Then, the cleaned substrates were spin-dried with ethanol and acetone successively, resulting in a hydrophobic surface. The block copolymer was dissolved in toluene at a concentration of 20 mg/ml together with ~2 % w/w (relative to the polymer mass) antioxidant (Irganox 1010 from CIBA) to prevent cross-linking of the PB blocks during further treatment. The films were prepared by spin-coating at

3000 rpm for 30 s and were dried at room temperature in vacuum for 1 day. For all films, the film thickness was found to be 1500 ± 200 Å

The block copolymers SB28 were dissolved in toluene at a concentration of 40 mg ml $^{-1}$ together with ~2% w/w (relative to the polymer mass) antioxidant (Irganox 1010 from CIBA) to prevent crosslinking of the PB blocks during further treatment. Films were prepared byspin-coating Si(100) wafers of a size 4 cm × 2 cm (Silchem Handelsgesellschaft mbH) at 3000 rpm for 30 s . The Si substrates were precleaned with the same procedure described for the SB216. Even in this case the cleaned substrates were spin-dried with ethanol and acetone successively, resulting in a hydrophobic surface. After spin coating, the films were dried at RT in vacuum for one day. For all as-prepared films, the film thickness was found to be in the range 2150 ± 20 Å.

Films of three different thicknesses were prepared for the OB5 by spin-coating a 1 wt.-% toluene solution onto Si wafers at frequencies of 1000, 2000 and 3000 rpm. The wafers had previously been cleaned using an ammonium hydroxide/hydrogen peroxide/water mixture 1:1:1 at 68°C for 1 hour, then they were rinsed with Millipore water and left overnight in water to stabilize the SiO_2 top layer. The day after, they were dried and coated with the polymer film. The film thicknesses were found at D_{film} = 520 ± 50 Å, 430 ± 50 Å and 350 ± 50 Å for films spin-coated at 1000 rpm, 2000 rpm and 3000 rpm, respectively. The film thicknesses thus amount to 2.0, 1.6 and 1.3× D_{lam}^{bulk}, respectively. In the following, the films will be referred to as OB5 thick, intermediate and thin.

2.4 VIS-interferometry

The film thicknesses of the films were monitored in-situ during thermal and vapour/drying treatment using a FilMetrics F30 spectroscopic reflectometer for the measurements performed at CHESS. At DESY, a white-light interferometer NanoCalc 2000, Ocean Optics was, instead, used. The measuring time was 1 s. The film thickness was measured in-situ once per second through a glass window in the lid of the sample cell using the white light interferometer. When fitting the optical reflectance curves measured in a wavelength range of 400-900 nm, the refractive index of the sample was assumed to be n = 1.5.

The NanoCalc 2000 (Figure 2.2) is a thin film measurement system ideal for in-situ and real-time measurement of transparent and semi-transparent thin layers, in a thickness range of 50 nm - 20 µm, therefore suitable for our investigations. Depending on the layer and substrate material it can measure layers of just a few nanometers up to several hundreds of microns.[35]

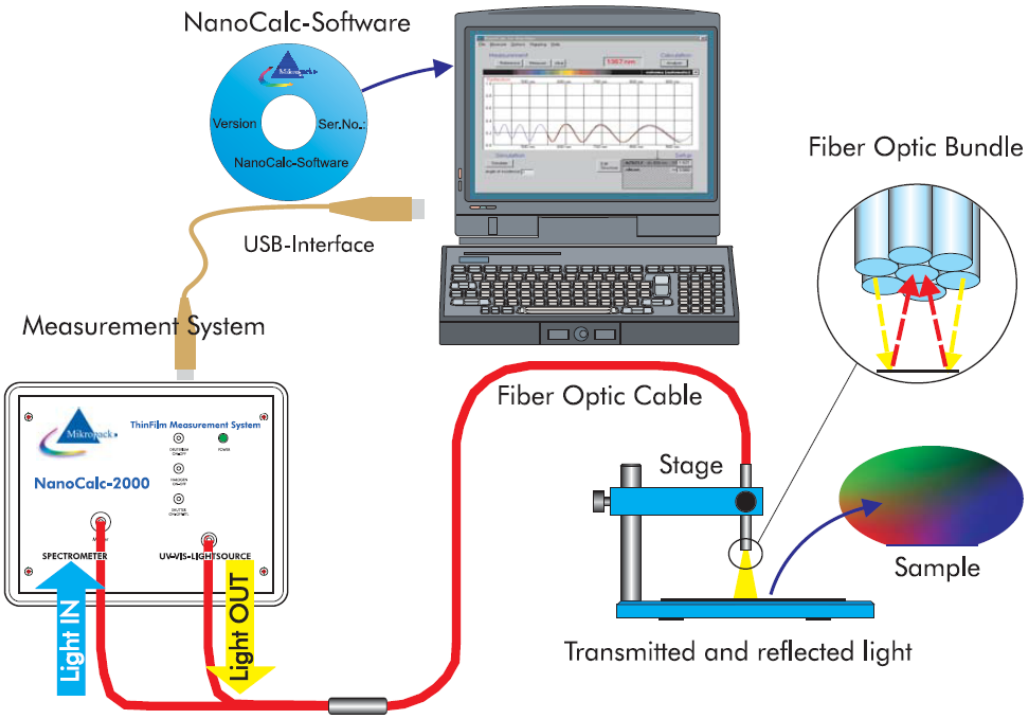

Figure 2.2. Schematic of the VIS-interferometer NanoCalc 2000 set-up.[35]

Optical techniques determine thin-film characteristics by measuring how the film interacts with light (Figure 2.3). Optical techniques can measure the thickness of a

film. Optical constants (*n* and *k*) describe how light propagates through and reflects from a material. Optical techniques are usually the preferred method for measuring thin films because they are accurate, non-destructive, and require little or no sample preparation. One of the most common optical measurement methods is spectral reflectance/transmittance. Spectral reflectance measures the amount of light reflected from a thin film over a range of wavelengths, with the incident light normal (perpendicular) to the sample surface. The amplitude and periodicity of the reflectance of thin films are determined by the films thickness, optical constants and other properties such as interface roughness. In reflectometry it is not possible to solve for film properties in closed form, nor is it possible to solve for *n* and *k* at each wavelength individually. In practice, mathematical models are used that describe *n* and *k* over a range of wavelengths using only a few adjustable parameters. Film properties are determined by calculating reflectance spectra based on varying trial values of thickness and the *n* and *k* model parameters, until the calculated reflectance matches the measured reflectance best (Best-Fit-Algorithm).[35]

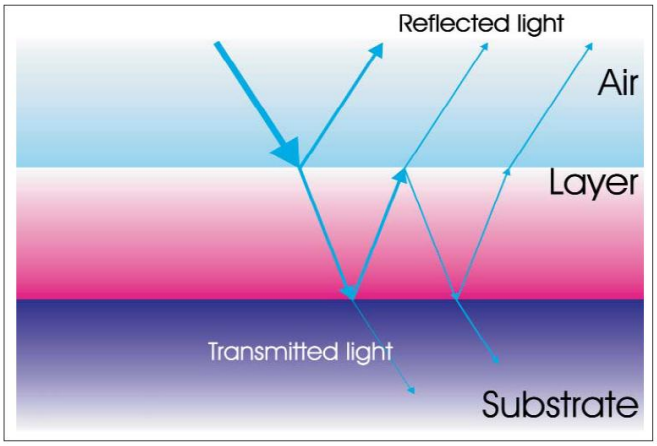

Figure 2.3. Principle of white-light interference.[35]

There are many models for describing *n* and *k* as a function of wavelength. When choosing a model for a particular film, it is important that the model is able to accurately describe *n* and *k* over the wavelength range of interest using as few parameters as possible. In general, the optical constants of different classes of materials vary quite differently with wavelength and require different models to describe them. The NanoCalc 2000 system requires as input parameters the number and kind of the compound thin films. The refraction index behavior versus wavelength *n* is given by Cauchy coefficients (Figure 2.5).[35]

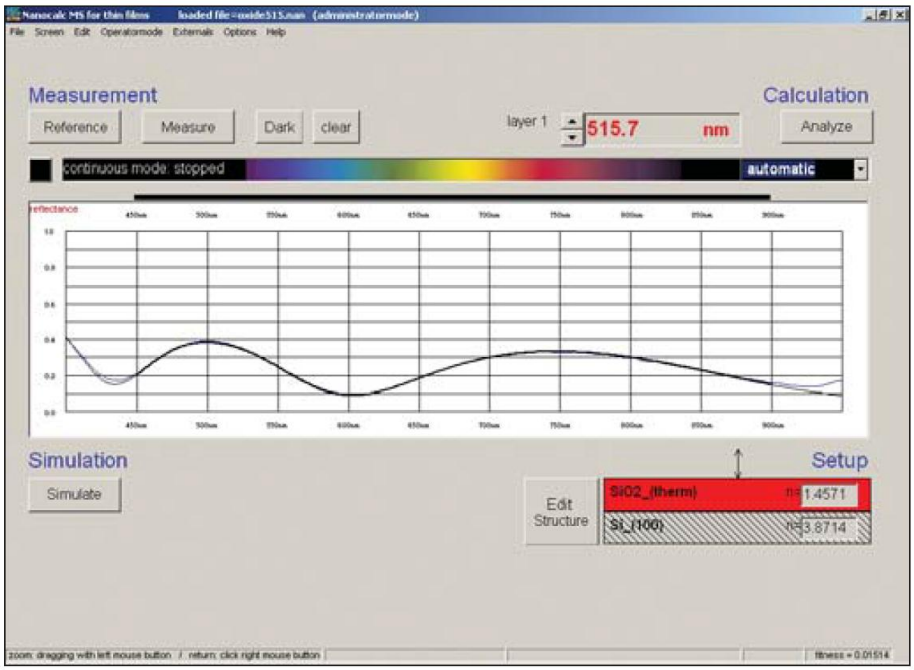

Figure 2.5. NanoCalc software interface, showing a thickness measurement and fitting of a 515 nm thick layer.[35]

The F30 can measure film thickness and optical constants in-situ and real-time. Smooth and translucent, or lightly absorbing films, may be measured, in a thickness

range of 15 nm - 100 µm, therefore suitable for our investigations.[36] The physics principle and fitting characteristics are similar the ones described above for the NanoCalc 2000.

2.5 Atomic force microscopy

The most used technique to study block copolymer film morphologies is the atomic force microscopy (AFM). This is a lab-based technique that allows imaging of the surface structure. The usual method applied in the case of polymer films is called tapping mode AFM, whereby a sharp tip (usually a silicon or silicon nitride crystal) is oscillated just above the surface of a sample (Figure 2.6). The tip tracks the topography of the surface and its oscillation frequency is changed by the presence of relatively harder or softer features at the surface, giving rise to so-called phase contrast images.[17]

For the SB216 samples tapping mode AFM experiments were carried out using a Jeol JSPM 5200 instrument with point-probe silicon SPM sensors, type CSC 12/AIBS/50 from µMash, having a typical resonance frequency of 200 kHz. A set-point ratio of 0.8-0.9 was chosen. Due to their different viscoelastic properties, there is a strong phase contrast between PS and PB domains. The Igor routine (Asylum Research) was used for Fourier transformation of the images. Samples for AFM were measured ex-situ at room temperature after the thermal treatment.

Also in the case of the OB5 samples tapping mode AFM experiments were carried out using the Jeol JSPM 5200 instrument with point-probe silicon SPM sensors, type CSC 12/AIBS/50 from µMash, having a typical resonance frequency of 150 kHz. A set-point ratio of 1.2-1.5 was chosen. Due to their different viscoelastic properties, there is a strong phase contrast between POS and PBMA domains. A routine written by us within the IgorPro environment was used for Fourier transformation of the images. The 1D Fourier transforms are given in dependence on k, the wave number, which is an inverse length scale. Samples for AFM images were prepared in the same way as the ones used for the GISAXS measurements and one vapour/drying cycle was carried out in the same way. AFM measurements were carried out after preparation and after one vapour/drying cycle at room temperature.

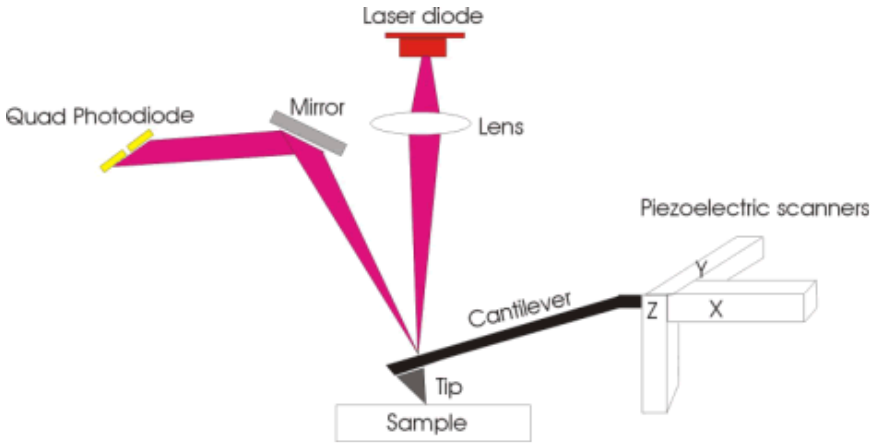

Figure 2.6. AFM diagram[37].

2.6 X-ray reflectometry

Specular X-ray reflectivity (XR) provides the density profile normal to the surface with Å resolution, via measurement of the intensity of reflected X-rays as a function of angle (at small angles). The methods are non-invasive in that the film structure is not perturbed by the measurement. X-ray reflectivity depends on variations in electron density. The theoretical background is dominated by Bragg's law

$$n\lambda = 2D_{film}sin\alpha_i \tag{2.1}$$

Where α_i and λ are the incident angle and wavelength of the X-ray beam and n = 1, 2, 3, etc. (Figure 2.7). Kiessig fringes are present when the two reflected beams interfere constructively. Kiessig fringes are an important phenomenon which arises to a large number of information: their period allows the determination of the film thickness; their amplitude, instead, give information about the roughness of the thin film. In case multilayers are present within the film, beside the Kiessig fringes as well as Bragg peaks appear. In this case it is possible to directly determine the D_{AB}. Therefore, by means of a modified Bragg law, it is possible to determine the multilayer thickness, corresponding to the angular spacing of the satellite maxima in the XR curve, and the total multilayer thickness, corresponding to the period of the Kiessig fringes. Specular X-ray reflectivity refers to scattering within a plane perpendicular to the surface of the sample and averages over lateral structures. The

lateral structure within block copolymer films can be, instead, probed by grazing-incidence small-angle X-ray scattering (GISAXS) in which the beam is incident on the sample at a grazing angle, but outside the specular plane, as described in the next section.[17]

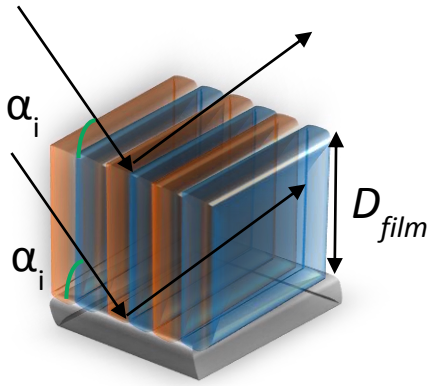

Figure 2.7. Illustration of the specular X-ray reflectivity.

For the SB216 and SB28 samples ex-situ XR by means of a D5000 diffractometer (Siemens) was used with an X-ray wavelength of 1.54 Å. A step size of 0.005° with a measuring time of 1 s per point was applied. Furthermore, in the case of the SB28, at beamline D1 at the Cornell High Energy Synchrotron Source (CHESS) at Cornell University in Ithaca, New York, U.S.A., the film thickness was measured in-situ with XR using the collimating slits, goniometer and sample environment of the GISAXS experiments. The detector was a ion chamber with an aperture of 50 mm height and 13 mm width mounted in front of the CCD camera. A blade placed in front of the ion chamber was screening the sample surface at low angle from the direct beam. The measuring time was 1 s per point and the whole curve was measured in ~8 min. The electronic background was measured and subtracted from the data. For all the measured samples, model fitting was carried out using Parratt 32 (HMI Berlin), which implements the Parratt's recursion scheme for stratified media.

For the SB216 fits, the scattering length density (SLD) of Si was kept between 2.0 × 10^{-5} Å^{-2} and 2.1×10^{-5} Å^{-2}. Small deviations may be due to slight variations of the cleaning procedure. The SLD and the thickness of the SiO_x layer were left as fitting parameters. For all films, an SLD value of 2×10^{-5} Å^{-2} and thicknesses between 17 and 22 Å were obtained consistently for the SiO_x. From the SLDs of pure PS (9.50× 10^{-6} Å^{-2}) and PB (8.26×10^{-6} Å^{-2}), the SLD of the P(S-*b*-B) investigated is expected to be 8.85×10^{-6} Å^{-2}. In fitting, the SLD of the polymer film was left as a free fitting parameter.

From the SLDs of pure PS (9.50×10^{-6} Å^{-2}) and PB (8.26 × 10^{-6} Å^{-2}), the SLD of the P(S-*b*-B) investigated, in the case of the SB28, is expected to be 8.85 × 10^{-6} Å^{-2}. In fitting, the scattering length density (SLD) of the polymer film was left as a free fitting parameter. In the fits, the SLD of Si was kept between 2.0 × 10^{-5} and 2.1 × 10^{-5} Å^{-2}. The SLD and the thickness of the SiO*x* layer were left as fitting parameters. For all SB28 films, a SLD value between 2 × 10^{-5} and 2.3 × 10^{-5} Å^{-2} and thicknesses of 20 °A were obtained for the SiO*x*. Small deviations for the SLD of Si and SiO*x* may be due to slight variations of the cleaning procedure.

2.7 Grazing-incidence small-angle X-ray scattering

Grazing-incidence small-angle X-ray scattering (GISAXS) is performed at synchrotron sources and the high flux enables rapid measurements including dynamic processes and measurements of weak scattering features. GISAXS is a fundamental and established technique to probe the lateral structure of block copolymer films.[17] Moreover, the measuring time is very short, therefore allowing to methodically studying in-situ the system kinetics.

The geometry of a GISAXS experiment is illustrated in figure 2.8. A monochromatic X-ray incident beam with the wavevector k_i is directed on a surface with a very small incident angle α_i with respect to the surface. The Cartesian z-axis is the normal to the surface plane, the x-axis is the direction along the surface parallel to the beam and the y-axis perpendicular to it. The X-rays are scattered along k_f by any type of electron density fluctuations at the illuminated portion of the surface.[38,39]

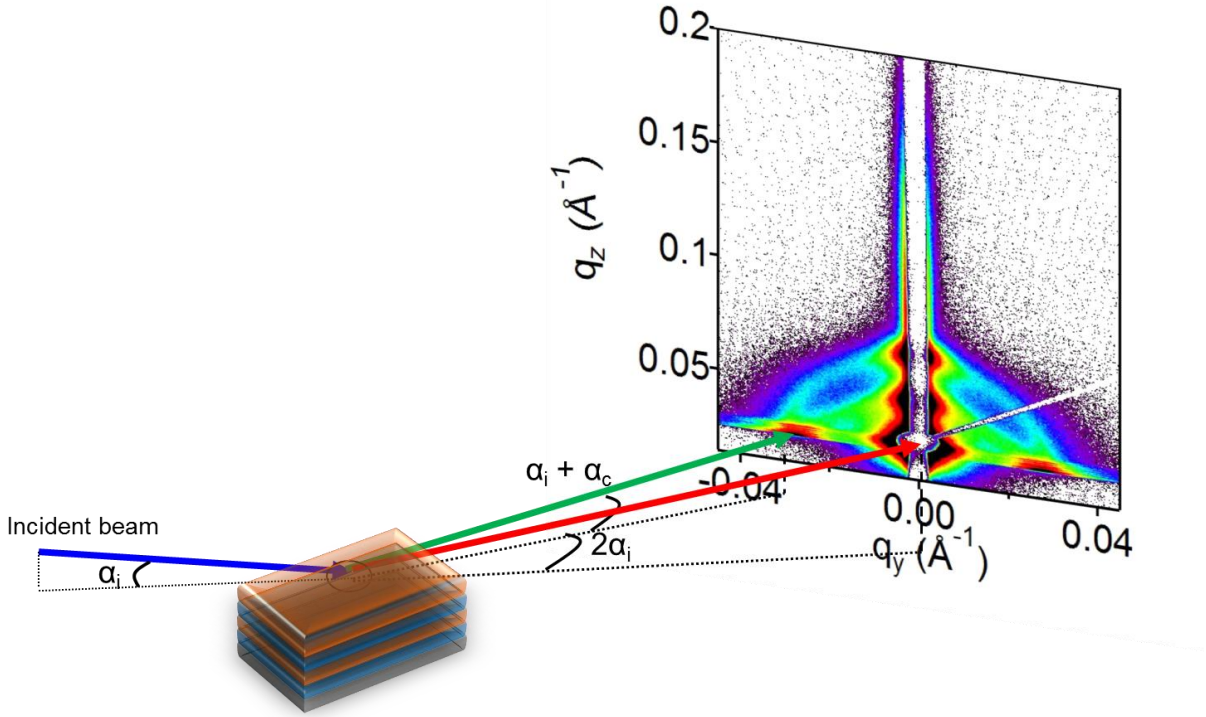

Figure 2.8. GISAXS geometry.

In general, a 2-D detector records the scattered intensity at angles up to a few degrees for the observation of lateral sizes ranging from a few up to hundreds of nanometers. The sample detector distance is normally in a range of 1 to 4 meters for GISAXS. Gas-filled wire frame detectors, CCD-detectors as well as imaging plates are in use. The direct and the reflected specular beam are often suppressed by two small beamstops to prevent damage or saturation of the detector.[38,39]

For the SB216 samples, scattering experiments were performed at beamline BW4, HASYLAB at DESY in Hamburg, Germany[40]. At BW4, the wavelength was λ = 1.38 Å with a bandwidth of 10^{-4} (Si(111) monochromator), and the beam was focused by Beryllium compound refractive lenses to a size of ~40 µm × 20 µm (horizontal × vertical) at the sample position, which limits the footprint to ~6 mm at an incident angle of 0.2°. A tantalum rod with a diameter of 1.5 mm served as a beam stop for the intense reflected beam and the strong diffuse scattering in the incident plane.

Parasitic scattering around the intense specularly reflected beam was in some cases blocked with an additional, disk-like beamstop. A MarCCD area detector was used for the detection of the scattered intensity. The pixel size was 79.1 µm × 79.1 µm. The sample-detector distance was chosen to be 1.915 m. $q_{||} = \sqrt{q_x^2 + q_y^2}$ and q_z are the in-plane and the normal components of the scattering vector, respectively. For small incident angles and scattering angles, the coordinates of the 2D detector correspond approximately to q_y and to q_z, and we use this notation in the remainder of the thesis.

The scattering experiments for the case of the SB28 samples were performed Scattering experiments were performed at beamline BW4, HASYLAB at DESY in Hamburg, Germany, and at beamline D1 at the Cornell High Energy Synchrotron Source (CHESS) at Cornell University in Ithaca, New York, U.S.A. At D1, λ was 1.22 Å with a beam size of ~500 µm × 100 µm (horizontal × vertical). An incident angle α_i = 0.16° was chosen, which resulted in a beam footprint on the sample having a length of 41 mm, which is i.e. similar to the sample size. α_i was larger than the critical angle of total external reflection of P(S-*b*-B), $\alpha_{c,p}$ = 0.12° and smaller than the critical angle of the Si substrate, α_{cS} = 0.17°, thus internal film structures could be detected and the beam was fully reflected from the sample/substrate interface. Moreover, at this incidence angle, the diffuse Bragg sheets (DBSs) of the as-prepared film were well separated both from the specularly reflected beam and the Yoneda peaks of the polymer and the substrate. A CCD camera with a pixel size of 46.9 µm × 46.9 µm was used as a detector with a sample-to-detector distance of 2.015 m. The sample was moved sidewards 0.3 mm after each measurement to avoid beam damage. The sample was scanned three times. A tantalum rod was placed vertically in front of the CCD camera to screen it from the reflected beam as well as the intense diffuse scattering in the incident plane. At BW4 the wavelength and set-up were the same as for the SB216, with a footprint of ~6 mm at an incident angle of 0.18°. At the chosen wavelength, $\alpha_{c,p}$ = 0.13° and α_{cS} = 0.19°. The sample-detector distance was chosen to be 1.930 m and the q_z resolution for the instrument was $\Delta\, q_z^{res} = 5 \times 10^{-4}$ Å^{-1}. The sample was moved sidewards 0.05 mm after each measurement to avoid beam damage. The *q*-space calibration was performed for both the beamlines fitting the characteristic ring arising from the silver behenate scattering signal.

In the case of the OB5, GISAXS experiments were performed at HASYLAB beamline BW4 equipped with a MarCCD camera as an area detector. Even in this case the wavelength was 1.38 Å, meanwhile the sample-to-detector distance was 2.23 m. The beamline set-up is the same previously describe for the other two samples. In the experiment, the incident angle, α_i, was chosen at 0.20°-0.25°, thus at values slightly above the critical angle of total external reflection of SiO_x which is α_{cS} = 0.19° at the wavelength used.

In all images, the specularly reflected beam as well as the Yoneda peaks are observed. The latter are intensity maxima at exit angles $\alpha_f = \alpha_{cS}$ or $\alpha_f = \alpha_{cP}$.

For perpendicular lamellar orientation, the differential scattering cross-section for diffuse scattering factorizes into two terms: $d\sigma/d\Omega = g(\mathbf{q}_{||}) \times \left|f(k_{iz}, k_{fz}, D_{film})\right|^2$.[41] The first factor, $g(\mathbf{q}_{||})$, is the Fourier-transform of the lateral density-density correlation function, which only depends on the components of the scattering vector in the film plane, $\mathbf{q}_{||} = (q_x, q_y)$. The lateral structure of the perpendicular lamellae thus gives rise to constructive interference at multiples of $q_{||} = 2\pi/D_{lam}$, where D_{lam} denotes the lamellar thickness (i.e. the repeat distance) in the film. The intensity profile normal to the sample plane is described by the second factor. The *z*-component of the momentum transfer, q_z, is given by $q_z = k_{fz} - k_{iz}$ with $k_{iz} = (4\pi sin\alpha_i)/\lambda$ and $k_{fz} = (4\pi sin\alpha_f)/\lambda$ being the *z*-components of the incident and the exit wave vector, respectively. For fixed k_{iz}, i.e. for a specific GISAXS map, each value of k_{fz} corresponds to a certain value of q_z. $\left|f(k_{iz}, k_{fz}, D_{film})\right|^2$ has sharp maxima at the critical angles of total external reflection of the polymer and the substrate, α_{cP} and α_{cS}, respectively, the so-called Yoneda peaks of the polymer and the substrate[42]. Additionally, in films of homogeneous thickness D_{film}, and lamellae extending through the full thickness of the film, fringes are expected above α_{cS}, which, for large q_z, have a period $\Delta q_z = 2\pi/D_{film}$, similar to Kiessig fringes in reflectometry. Between α_{cP} and α_{cS}, oscillations are expected as well, however, their shape and period is strongly influenced by dynamic effects[25].

In summary, in the two-dimensional GISAXS maps of laterally ordered films, Bragg rods are expected at parallel momentum transfers $q_{||}$ being multiples of $2\pi/D_{lam}$ and with a q_z-profile mainly determined by D_{film}.

For randomly oriented lamellae, rings of high intensity around the direct beam (diffuse Debye-Scherrer rings, DDSRs) and around the specularly reflected beam are expected as well (Figure 2.9).[43] In contrast to transmission scattering, the intensity along the DDSR is not homogeneously distributed, but is maximum near the Yoneda peaks appearing at the q_z values corresponding to the critical angles of the polymer film and the substrate (in the so-called Yoneda band) and decays towards high q_z.[42] The lamellar thickness, D_{lam}, is calculated using Bragg's law:

$$D_{lam} = \frac{2\pi}{q_{y,DDSR}}, \tag{2.2}$$

where $q_{y,DDSR}$ is the radius of the DDSR centered at the specularly reflected beam.

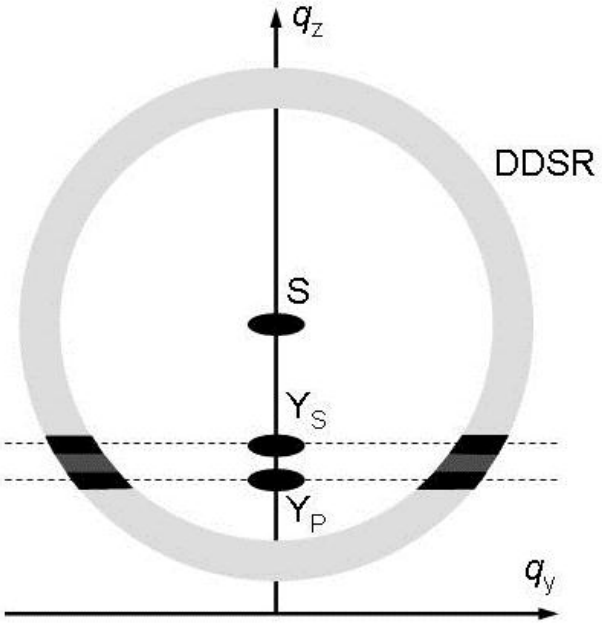

Figure 2.9. Schematic representation of the scattering from a randomly oriented lamellar thin film. S, Y_S and Y_P denote the specularly reflected beam and the Yoneda peaks of the substrate and the polymer film, respectively. DDSR denotes the first-order diffuse Debye-Scherrer ring. The darker the ring, the higher its intensity. The dashed lines mark the q_z positions of Y_S and Y_P. Not shown is the strong intensity decay of the ring below Y_P.

2.8 Small-angle X-ray scattering

The small-angle X-ray scattering (SAXS) technique is used to study the electron density fluctuations that occur over larger distances as a result of structural inhomogeneities. SAXS is widely used to study the lamellar structure by measuring parameters such as lamellar spacing, height and diameter of the lamellar stacks, and thickness of the transition layer between the crystalline and amorphous domains. No sample preparation and data averaged over the area (typically 0.1 mm^2) of illumination are the most relevant advantages in using SAXS. SAXS is also used for studying conformation, size and dynamics of polymers in solutions and in gels.[44]

The small-angle X-ray scattering (SAXS) experiment for the SB 28 was carried out at FRM II, Garching, Germany, using an Hecus S3-Micro. An X-ray beam with a wavelength λ = 1.54 Å was used. A Pilatus 100k detector with a pixel size of 172 µm $\times$ 172 µm was used. The sample to detector distance was 0.29 m. The sample was directly exposed to the X-ray beam in order to avoid any unwanted scattering signal from other materials but bulk structures. Measuring time was 10 h. Measurements were carried out at room temperature. The 2D data were spectrally averaged. The calibration of the detector and the determination of the position of the direct beam were carried out using silver behenate.

Chapter 3

Structural changes during thermal treatment

In the present chapter, we focused on the perpendicular lamellar orientation formed by high molar mass samples (SB216). We studied the effect of thermal treatment on spin-coated films. Spin-coating is a fast and easy technique to prepare films of homogeneous thickness, but it also introduces a large number of defects in the block copolymer mesophase and results in a multi-domain structure. Thermal treatment may anneal these defects because it reduces the interfacial tension between both blocks and increases the polymer mobility. The latter is especially important for block copolymers containing a polystyrene (PS) block, which is glassy at room temperature.

In the previous chapters it has already been pointed out that the nanostructure in the ordered phase is controlled by a number of parameters, such as the interaction energy between the two blocks, the relative volume occupied by the two blocks, and the overall degree of polymerization, i.e. the molar mass. For thin films, the interface enthalpies and entropies at the air-polymer and the polymer-substrate interface[45,46,47,48], the roughness of the substrate[49] as well as confinement effects, i.e. film thickness[50], enter as additional parameters.

In this study GISAXS has been used since it offers a unique, non-invasive method to obtain information on both lateral and transverse structures inside block copolymer thin films. Various structural aspects of the different morphologies formed in block copolymer films have been studied using GISAXS, in particular the structural changes of di-block copolymer films in solvent vapour. [51,52,53,54,55,20,56,57,58,59,60]

Our group studied thin films of symmetric and thus lamellar poly(styrene-*b*-butadiene) and have previously found that molar mass is a determining parameter regarding the orientation of the nanostructure relative to the film surface[52,53,60]. Using atomic force microscopy (AFM) and GISAXS, they found that in low molar mass (below ~ 55 kg/mol) P(S-*b*-B) films, the lamellae have their interfaces parallel to the film surface, whereas for high molar masses (above ~ 90 kg/mol), they are perpendicular. The latter orientation came unexpected, but could be explained by a model involving the

interfacial tensions between all components as well as corrections to the strong-segregation limit[48]. To extract quantitative information on the lamellar structure from the complex GISAXS images, they have developed models for the GISAXS scattering cross-section of thin films of parallel or perpendicular lamellae in the distorted-wave Born approximation[42]. The structural changes during solvent vapour treatment were investigated in-situ, and complex rearrangements of the lamellar structure were encountered[51,22,41,25].

Systematic studies of the thermal behavior of block copolymer films are scarce.[61,62,63,64,65,66] Thick films were prepared by roll-casting from cylinder-forming and lamellae-forming P(S-*b*-B-*b*-S) triblock copolymers[61]. These macroscopically oriented samples were investigated using transmission electron microscopy (TEM) and transmission SAXS. It was observed that the distortion present in the hexagonal arrangement of the cylinders after roll-casting was relieved during treatment at 120°C. The lamellae-forming triblock copolymer contained a number of defects after roll-casting. Thermal treatment led to a nearly complete annealing of these defects, resulting in the formation of a close to perfect structure. In-situ transmission SAXS showed that the lamellar thickness increases abruptly at 75°C and stays at this value, also upon cooling. These findings were explained by the relaxation of triblock copolymers, which have their PS blocks in separate domains, along the cylindrical or lamellar interface.

An in-situ AFM investigation of a single layer of cylinders in PS-containing di-block copolymers in what gave insight into the relation between the change of the orientational correlation length of the cylinders and the various ways of defect annihilation during treatment at 140 or 170°C.[62] In another study, a number of mechanisms could be identified for a similar single or double layer of cylinders thermally treated at 105°C where structural defects are annihilated by short-term phase transitions into what may be considered excited states[63]. In a few recent publications, the structural response of block copolymer thin films to temperature gradients has been investigated[64,65,66] using, among others, thermally responsive block copolymers[64,65]. Cold-zone annealing was found to be very efficient in enhancing the ordering kinetics in a block copolymer thin film, however ordering was detected under certain annealing conditions only[66].

In the present study, we focus on the influence of treatment temperature on the structure of lamellar thin films with initially perpendicular lamellae. The samples were spin-coated onto Si wafers. The treatment temperatures were chosen between 60 and 130°C, i.e. below and above the glass transition temperature of the PS block (~100°C) (the glass transition temperature of PB is far below room temperature)[16]. We expect that treatment above T_g allows for long-range diffusion of the copolymers and thus more significant alterations of the lamellar structure than below where only local changes are possible. In-situ GISAXS allowed us to investigate changes in the

lamellar thickness and the correlation of the lamellae in the film plane. We correlate these findings with results obtained by AFM and X-ray reflectometry.

3.1 Experimental procedure and results

During the GISAXS measurements, the film was in a sample chamber mounted on a heating plate and continuously flushed with N_2 gas. The temperature in the chamber was measured close to the sample by means of a Pt100 resistance installed at the bottom of the sample holder. A GISAXS image was taken at room temperature. Then, the samples were heated to the target temperature within ~35 min. The samples were kept at this temperature for ~5 min, before another GISAXS image was taken. Then, the samples were cooled down to room temperature, which took ~40 min. After another 5 min, a GISAXS image was taken. The exposure times were always 400 s. Beam damage was minimized by choosing a new spot on the sample for each measurement. All the GISAXS images taken at RT after 400 s are very similar to the ones measured for 5 s, therefore we can rule out any influence on our measurements related to beam damage. The samples were investigated using AFM within a couple of days after the GISAXS experiments.

To quantify the structures by means of the GISAXS mesurements, 1D intensity profiles were constructed along q_y at the q_z-value of the Yoneda peak of the polymer film, averaged over the range q_z = 0.0255 Å^{-1} to 0.0275 Å^{-1}. In this q_z-range, the transmission function of the polymer film has a maximum[42], thus the scattering is dominated by the structures in the polymer film. Lorentz functions were fitted to the peaks in the profiles due to the first-order BRs for both negative and positive q_y values:

$$I(q_y) = I_0 \Big/ \left[1 + 4\left(\frac{q_y - q_{y1}}{w} \right)^2 \right] \tag{3.1}$$

where q_{y1} is the peak position, w the full width at half maximum (FWHM) and I_0 the amplitude, and the results from negative and positive q_y-values were averaged. The number of correlated lamellae, N_S, was estimated from q^* and w:[16]

$$N_S = 2.75 \times \frac{q^*}{w\pi} \tag{3.2}$$

where q^* denotes the peak position

The conversion of the 2D images from pixels to *q*-values as well as the construction of 1D profiles and the peak fitting were carried out using the GISAXS Analysis Package, written by us within the Igor Pro development enviroment.

The AFM height image taken after spin-coating and drying at room temperature shows small and randomly oriented lamellar domains (Figure 3.1a). The lamellae themselves are not continuous but consist of small round grains. The RMS surface roughness is 40 Å. The 2D Fourier transform (figure 3.1a, inset) displays a distinct ring. The corresponding 1D Fourier transform shows a clear peak at a wave number of 1.06×10^{-3} $Å^{-1}$ (Figure 3.2, lower curve), which corresponds to a repeat distance of 940 ± 30 Å.

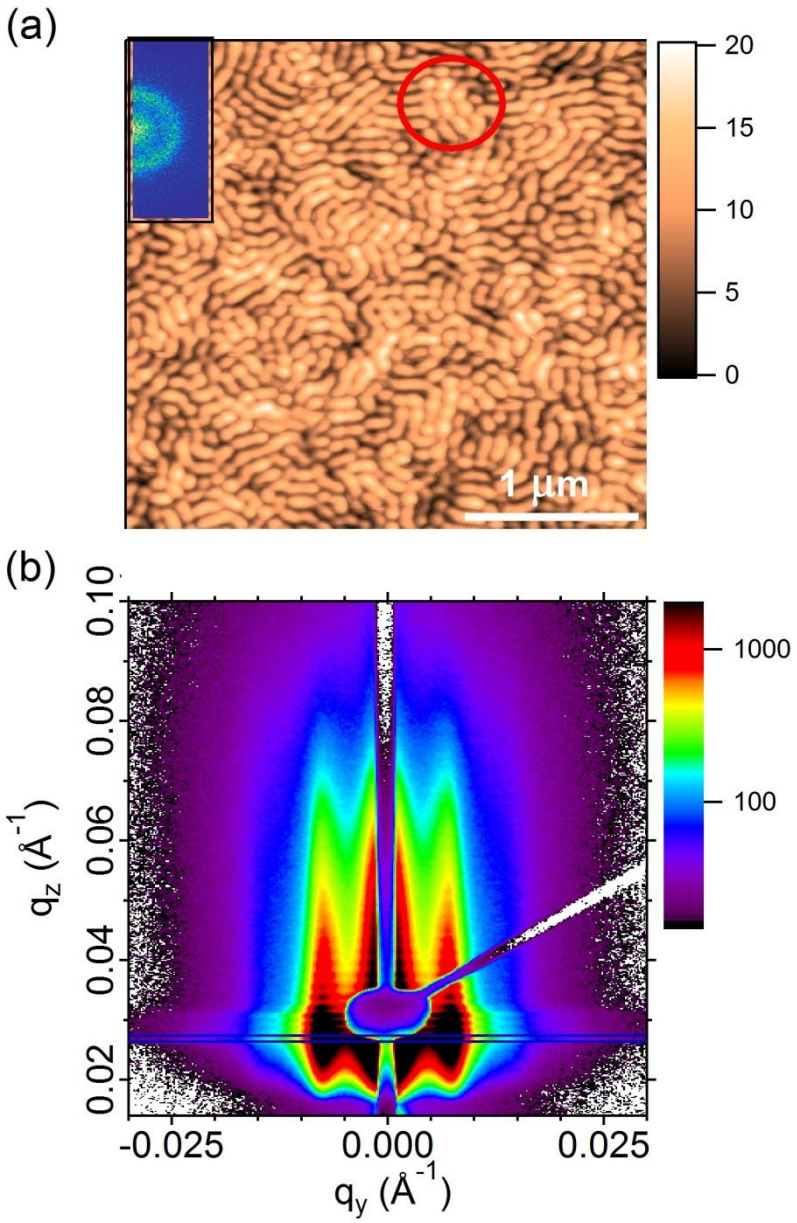

Figure 3.1. (a) AFM height image, size 3 µm × 3 µm with the 2D Fourier transform in the inset. The circle marks a lamellar domain where the lamellae are composed of grains. The hight scale is in nm. (b) 2D GISAXS image of the as-prepared film, both measured at room temperature. The blue horizontal lines in (b) show the region used to construct the intensity profiles. The intensity scale is logarithmic.

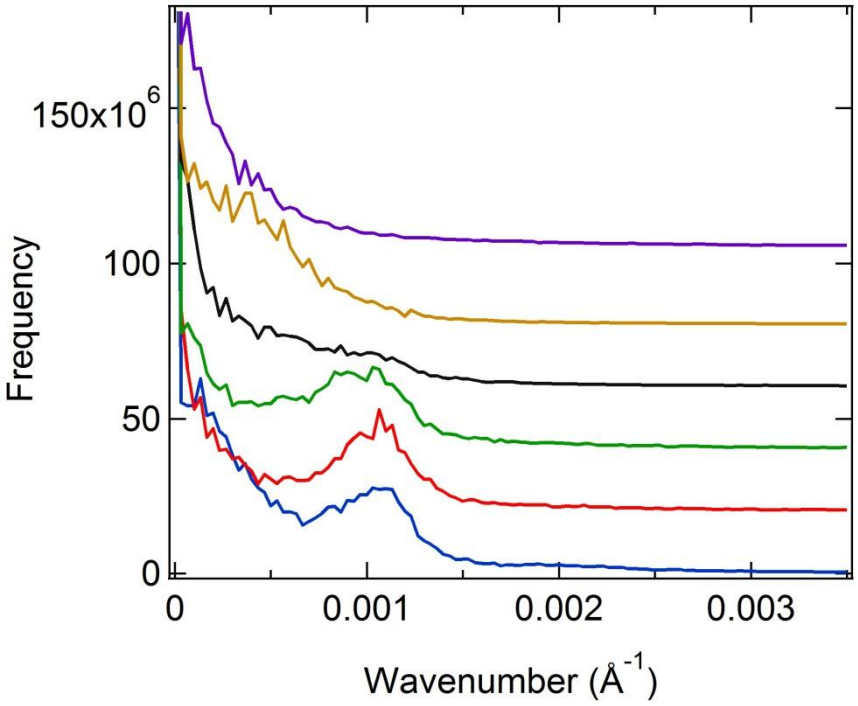

Figure 3.2. 1D Fourier transforms of the AFM height images. From bottom to top: room temperature, and after thermal treatment at 85°C, 100°C, 105°C, 120°C and 130°C. The curves are shifted vertically.

At room temperature, the 2D GISAXS images display straight and elongated Bragg rods (BRs) at $q_y = \pm 2\pi/D_{lam}$ which indicate the perpendicular lamellar orientation (Figure 3.1b). Both first and second order peaks are evident, i.e. the film contains a noticeable amount of perpendicular lamellae. Oscillations between the Yoneda peak of the polymer and of the substrate are clearly visible, indicative of a well-defined and smooth film surface, in consistency with AFM. From the q_y-positions of the BRs (q_y = 0.0073 Å^{-1} and 0.0146 Å^{-1}), obtained from fitting a Lorentz curve (Equation 3.1) to the first- and second-order peaks in the 1D intensity profile, the lamellar thickness is determined to be 861 ± 5 Å, which is slightly lower than the value obtained from AFM. The averaged number of correlated lamellae, N_S, in the film plane (Equation 3.2) is 2.6, which is consistent with the AFM image (the same value is obtained at higher q_z-values, so the structure is truly two-dimensional). Both methods thus confirm the

presence of laterally ordered structures inside the film, as previously observed for similar samples[51,52,53,60].

The XR curve (Figure 3.3a, lower curve) shows a number of Kiessig fringes. A good fit was obtained for a homogeneous film with an SLD of 9.7×10^{-6} Å^{-2}, a thickness of 1350 ± 20 Å and a surface roughness of 44 ± 4 Å (Figure 3.3b). The SLD of the polymer film is close to the expected value. The film thickness and surface roughness are consistent with the results from white-light interferometry and AFM, respectively.

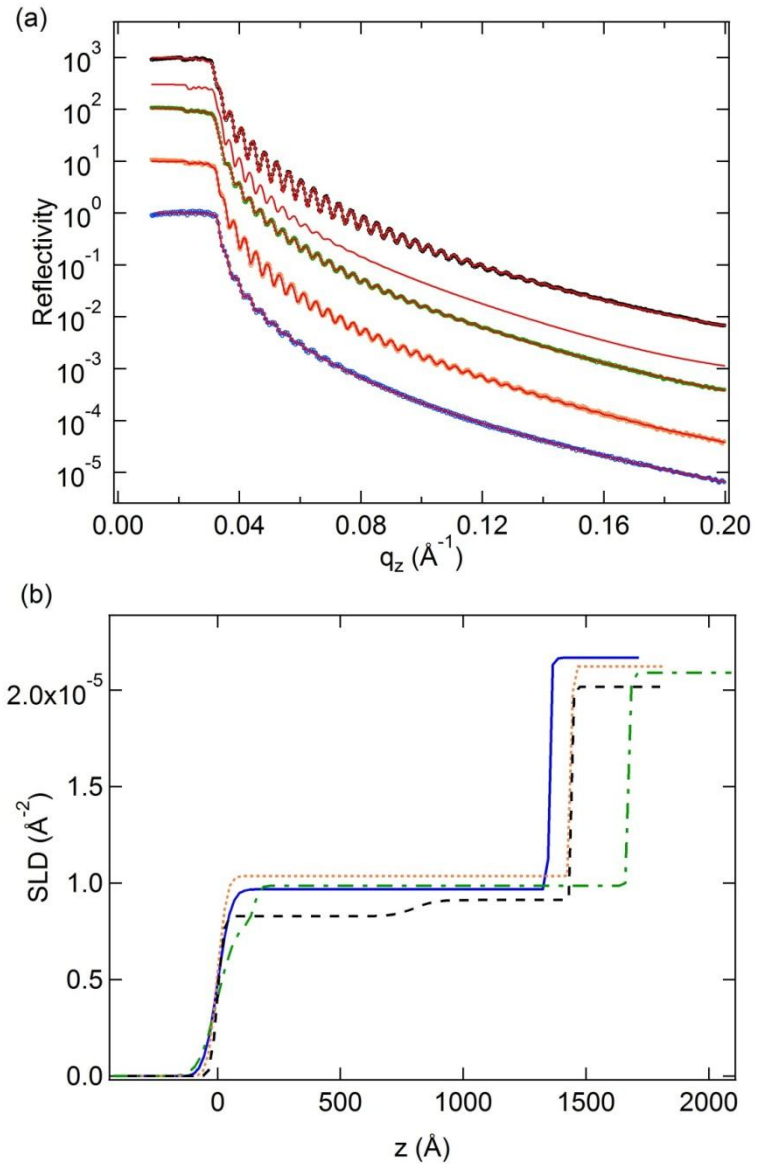

Figure 3.3. (a) XR curves of the as-prepared film (lower blue curve) and films treated at 100 °C (second curve from below, orange), 120 °C (third curve from below, green), and 130 °C (upper black curve), and subsequent cooling down. The best fit for the 120°C curve using only one layer is shown as a thin red line right above the experimental curve. Symbols: experimental curves; lines fitted model curves. The curves were shifted vertically by a factor of 10, respectively. (b) Corresponding SLD profiles of the as-prepared film (blue full line) and the films treated at 100 °C (orange dotted line), at 120 °C (green dash-dotted line) and 130 °C (black dashed line).

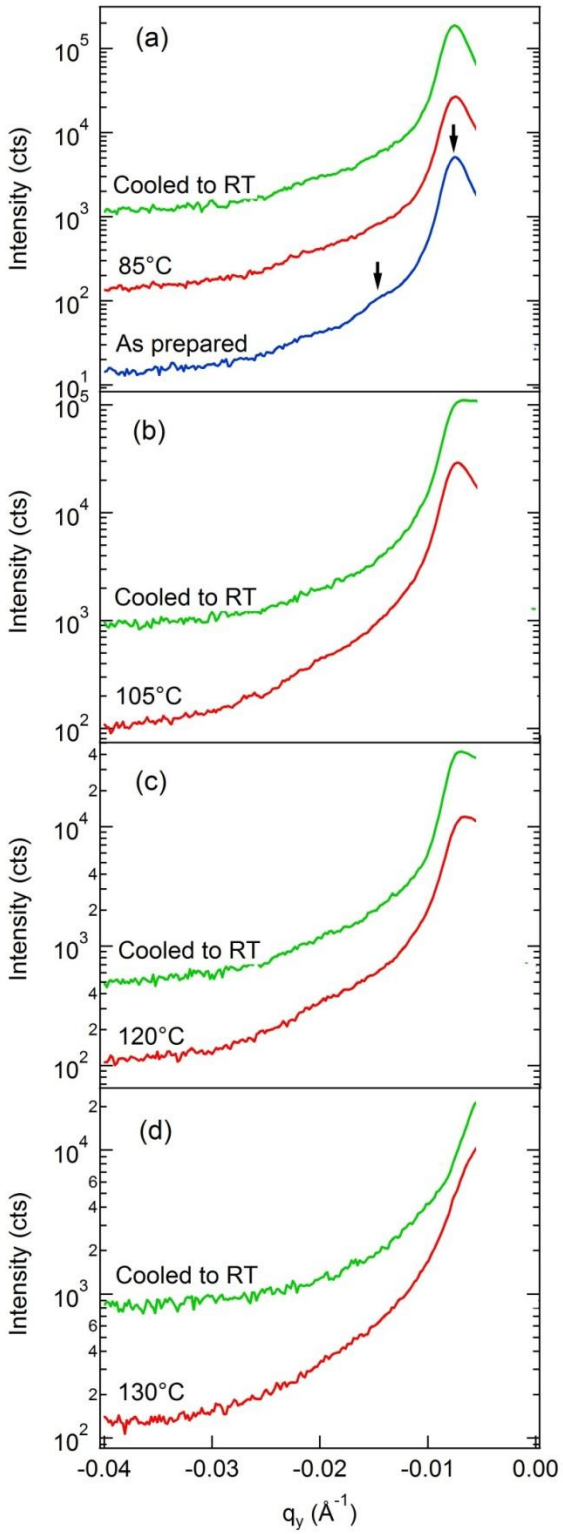

Figure 3.4. 1D GISAXS intensity profiles along q_y of the (a) as-prepared film during treatment at 85°C and after cooling down to room temperature. Same for 105°C (b), 120°C (c) and 130°C (d). The arrows in (a) indicate the positions of the first- and second-order BRs. In (a-d), the curves are shifted vertically.

To investigate the structural changes during thermal treatment of the films, we have carried out in-situ GISAXS measurements at the target temperature and after subsequent cooling down to room temperature (Figure 3.5, left and middle pictures). At temperatures between 60°C and 100°C, the shape of the BRs changes (Figure 3.5a,b) with respect to the shape at room temperature (Figure 3.1b): In addition to the straight part extending to high values of q_z, a contribution which is slightly bent inwards is present as well. The higher the temperature, the shorter is the bent part. We attribute the bending to tilting of the lamellae away from the purely perpendicular orientation. At temperatures between 105°C and 120°C (Figure 3.5c,d, left picture), the elongated straight parts vanish, and the bent parts become shorter and broader with increasing temperature. At 130°C (Figure 3.5e, left picture), no more BRs can be discerned, and only diffuse scattering is observed around the specularly reflected beam. At all target temperatures and after cooling down, the oscillations reflecting the high smoothness of the film surface and the absence of internal layering are present; only after cooling down from 130°C, they vanish. We anticipate that this may be due to the formation of a more complex inner structure. We note that even at 130°C, the sample is deeply in the ordered state (T_{ODT} is expected at ~700°C).

To distinguish whether the above described structural changes upon thermal treatment depend on treatment time, we have carried out additional in-situ GISAXS measurements during prolonged thermal treatment. A thin film was thermally treated at 100°C for 3 h and another one at 130°C for 1 h. Both GISAXS images were very similar to the ones taken after 5 min at the respective temperatures.

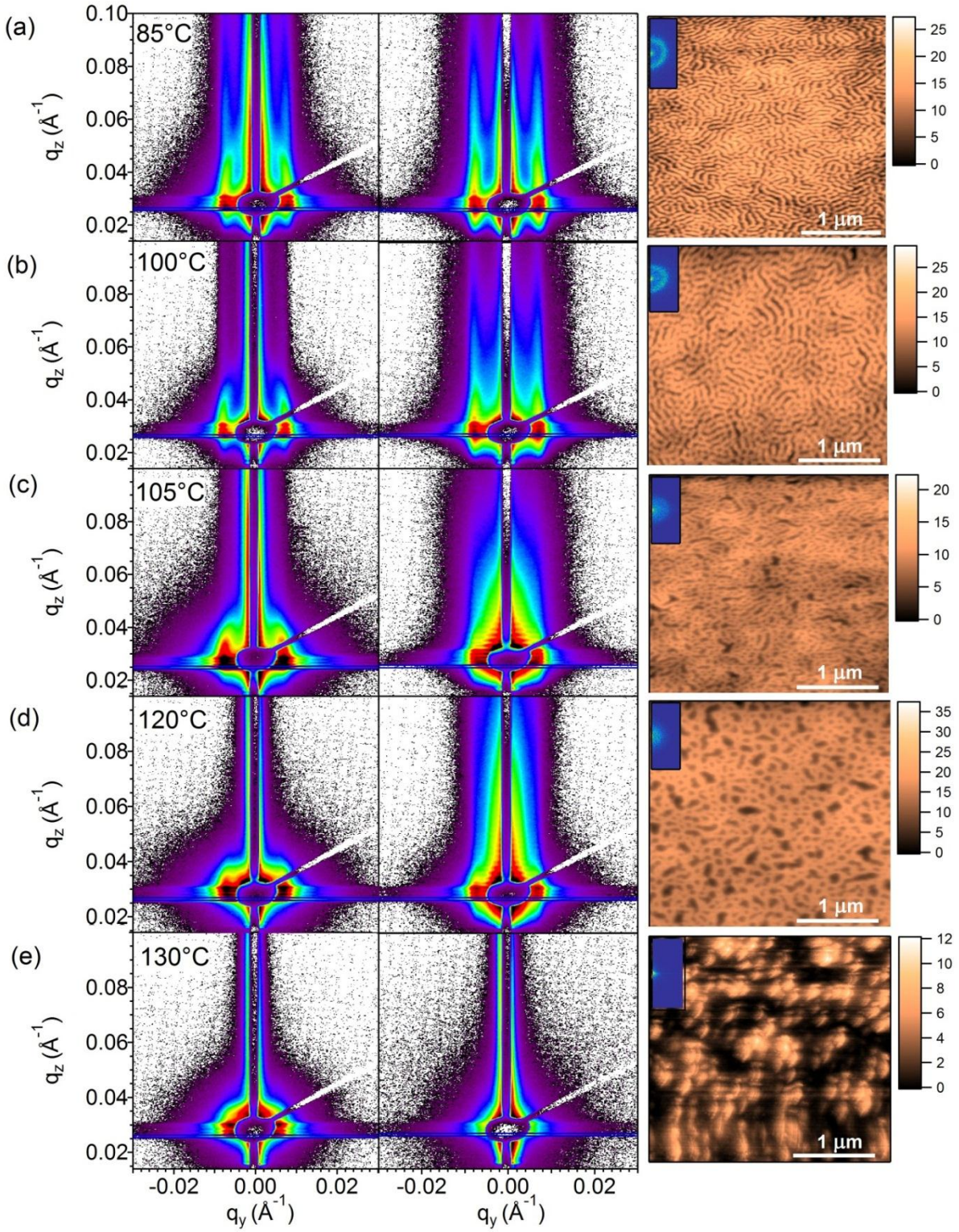

Figure 3.5. In-situ results at the target temperature and after cooling down. For each annealing temperature, we show 3 images: GISAXS at the target temperature (left) and after cooling down to room temperature (middle) and ex-situ AFM image (right). The target temperatures are given in each row. The blue horizontal lines show the

regions used to construct the intensity profiles. The color scale for all GISAXS pictures is the same as in figure 3.1b. The AFM height images have a size of 3 µm × 3 µm. The high scale is in nm. The insets show the corresponding 2D Fourier transforms.

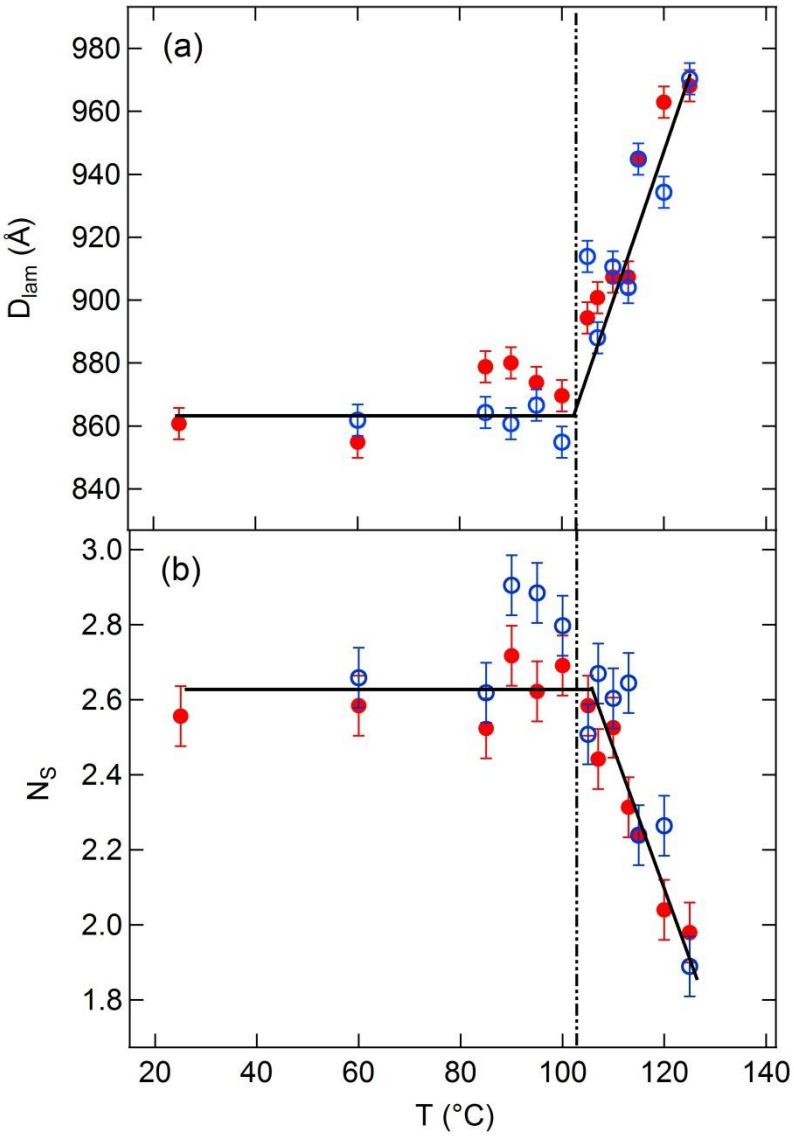

Figure 3.6. (a) Apparent lamellar thickness, D_{lam}, and (b) number of correlated lamellae, N_S, as a function of treatment temperature. Closed symbols: at the treatment temperature given, open symbols: after cooling down from this temperature to room temperature. The lines guide the eye. The vertical dash-dotted line marks T_g(PS).

The lamellar thickness, again determined from the q_y positions of the BRs at the q_z value of the Yoneda peak of P(S-*b*-B), is unchanged at ~870 Å up to 100°C (Figure 3.6a). The same holds for the number of correlated lamellae, N_S, in the film plane (Equation 3.2), which is unchanged at ~2.6 up to 100°C. At 105°C, D_{lam} starts to increase, and N_S starts to decrease. At 125°C, D_{lam} = 970 Å is reached, and N_S has decreased to ~1.9. The increase of D_{lam} and the decrease of N_s are presumably not due to a real expansion of the lamellar structure but rather to an increase of orientational disorder. The resulting bending of the BRs around the specular peak causes a decreased q_y peak position and an increased width *w* in the intensity profiles taken at the q_z-value of the Yoneda peak of the polymer, which is below the specular peak. At 130°C, no more peak is visible, i.e. the lamellar structure is not present any longer.

Upon cooling down to room temperature after the thermal treatment, the straight BRs reappear for treatment temperatures up to 100°C, i.e. the perpendicular orientation is recovered (Figure 3.5a,b, middle pictures). This is also evident from the intensity profiles (Figure 3.4a), where the peak position and shapes are nearly unchanged from the as-prepared state. In contrast, upon thermal treatment at 105-120°C, the BRs do not quite recover after cooling down to RT (Figure 3.5c,d, middle pictures and Figure 3.4b,c), and they are completely absent after thermal treatment at 130°C (Figure 3.5e, middle picture and Figure 3.4d). In summary, the perpendicular orientation is unchanged by thermal treatment up to 100°C, destabilized between 100°C and 120°C, but partially reversible, and apparently vanished at 130°C.

The surface texture gives a hint on the origin of the structural changes. AFM images of the surface texture were taken after the thermal treatment described and the subsequent cooling to room temperature, i.e. ex-situ. After thermal treatment between 60 and 100°C, the order at the surface is locally slightly improved (Figure 3.5a,b, right pictures). The grains have merged and form continuous lamellae. The peaks in the 1D Fourier transforms (Figure 3.2) – which reflect the lamellar correlation – have nearly unchanged positions and widths from the as-prepared state, i.e. the mesoscopic lamellar correlation is unchanged, presumably due to the low polymer mobility. In contrast, after thermal treatment at 105-120°C, the surface order is lost. Larger structures are present at the surface which have no well-defined length scale (Figure 3.5c,d, right pictures). The Fourier transforms do not display peaks any longer (Figure 3.2). We attribute these changes to a migration of PB (which has a lower surface tension than PS) to the surface. After thermal treatment at 130°C, even larger surface structures appear (Figure 3.5e, right picture). The Fourier transform does not show any peak (Figure 3.2). The near-surface layer is smoother than the one observed after thermal treatment at 120°C. This process which requires large-scale motion is enabled by the increased mobility of the block copolymers above T_g(PS).

The XR curve of the sample taken after thermal treatment at 100°C (Figure 3.3a, second curve from below), shows Kiessig fringes as well. From modeling, the polymer film appears homogeneous with a nearly unchanged SLD of 1.0×10^{-5} Å^{-2} (Figure 3.3b). Both the thickness of the film, 1440 ± 20 Å, and the surface roughness, 46 ± 4 Å, are very similar to the one of the as-prepared film; the slight difference in the film thickness is due to unavoidable variations in the preparation process. After thermal treatment at 120°C, in contrast, a model with a single layer could not reproduce the experimental curve (Figure 3.3a, thin line above the curve measured at 120°C). An extra layer at the film surface has to be included in the model to obtain a good fit (Figure 3.3a, third curve from below). This layer has a thickness of 150 Å with an SLD of 8.0×10^{-6} Å^{-2} and a surface roughness of 60 Å (Figure 3.3b). The underlying homogeneous part is very similar to the as-prepared state and the one after thermal treatment at 100°C (layer thickness 1520 Å, SLD 9.9×10^{-6} Å^{-2} and surface roughness of 18 Å). We attribute the surface layer to a layer of PB at the surface which contains voids, in consistency with the AFM image (Figure 3.5d). Modelling the XR curve of the sample taken after thermal treatment at 130°C (Figure 3.3a, upper curve) reveals that the polymer film splits up into two layers: The bottom layer has a thickness of 650 Å with an SLD of 9.1×10^{-6} Å^{-2} (as expected for P(S-*b*-B) and a roughness of 70 Å, whereas the upper layer has a thickness of 800 Å with an SLD of 8.3×10^{-6} Å^{-2} and a surface roughness of 20 Å (Figure 3.3b). We attribute the upper layer which has a reduced SLD to a restructured surface layer. A hybrid structure is formed, where PB forms a thin surface layer (presumably ~200 Å thick), followed by a thin PS layer (~400 Å) and an interfacial layer to the underlying perpendicular lamellae, in agreement with Ref. 3. This parts cannot be distinguished but form together the upper layer of thickness ~800 Å. This is consistent with the GISAXS observation that, above 130°C, the complex structures inside the film are not observable any longer, due to interference of scattering in the upper and the lower parts of the film.

3.2 Conclusion

We conclude that the structures of lamellar P(S-*b*-B) di-block copolymer thin films depend strongly on treatment temperature. In particular, the highest glass transition temperature of the two blocks (T_g(PS) = 102°C) plays an important role. Upon treating the films at temperatures below T_g(PS) and subsequently cooling them down

to room temperature, the perpendicular lamellar orientation is unchanged inside the film, and only a local improvement is observed at the surface.

Treatment between 105°C and 120°C and cooling down to room temperature causes a partial reorganization of the lamellar structure inside the film: In addition to the straight and elongated BRs, an arc appears, indicating the presence of lamellae with a wider orientation distribution. This effect is the stronger, the higher the treatment temperature, which is reflected in the increasing value of the apparent lamellar thickness. Moreover, the number of correlated lamellae decreases, i.e. the lateral domain size decreases. After cooling to room temperature, both the apparent lamellar thickness and the number of correlated lamellae stay unchanged. However, the 2D GISAXS images at the target temperature and after cooling are different, i.e. structural changes do occur both during heating and during cooling. Especially, at the film surface, a severe rearrangement is observed, namely a wetting of the surface by PB. Above 130°C, the surface smoothen and the PB layer induces a PS layer underneath. Only in the lower part of the film, perpendicular lamellae may still be present. As consequence, the structure inside the film is not observable any longer with GISAXS, already at the target temperature. These large-scale rearrangements are possible because of the increased mobility of the polymers far above T_g(PS).

Thermal treatment is expected to enable structural reorganizations towards thermodynamic equilibrium. The thin P(S-*b*-B) films prepared by spin-coating are possibly not in thermodynamic equilibrium because the preparation process is very fast. The solvent evaporation process during spin-coating is presumably faster near the film surface than inside the films, thus the lamellar structure near the film surface has more defects than inside the film. We have observed that, at the film surface, only small grains form instead of continuous lamellae (Figure 3.7a), which merge upon thermal treatment below T_g(PS), while the lamellar structure inside the film is unchanged by the treatment (Figure 3.7b). This improvement only requires short-range motion of the polymers which is possible even below T_g(PS). In contrast, thermal treatment above T_g(PS), but below 130°C, results in changes both at the film surface and inside the film: The PB block migrates to the film surface, as expected from its lower surface tension and as previously observed[25], and inside the film, a wider lamellar orientation distribution is encountered (figure 3.7c). Such a reorganization of the lamellar structure is only possible above T_g(PS). Thermal treatment at 130°C results in a propagation of the layered structure into the film and to a very complex lamellar structure.

We conclude that thermal treatment and subsequent cooling results in changes of the lamellar structure, which occur both when heating the sample to the treatment temperature and when cooling down. The best correlated structure is obtained by treatment at 100°C, in consistency with Ref. 63. In-situ GISAXS measurements combined with XR and AFM experiments are mandatory for the detailed understanding of the process.

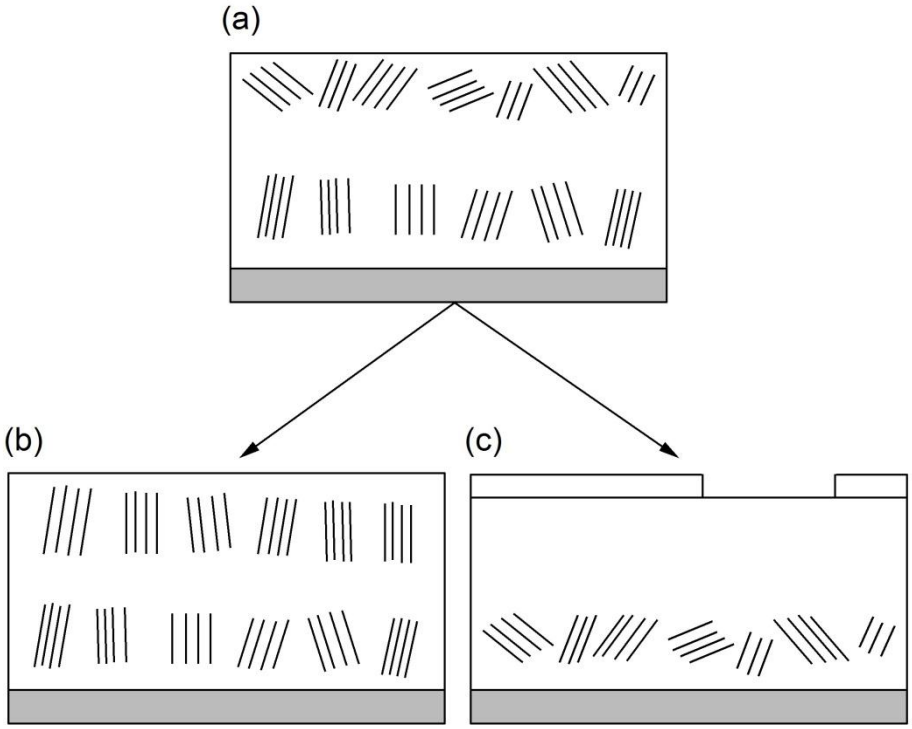

Figure 3.7. Sketch of the structure of the as-prepared sample (a), after thermal treatment below T_g(PS) (b) and above T_g(PS) (c). The short lines denote lamellar interfaces. For clarity, only few lamellar domains are shown and surface near and deeper-lying regions are distinguished. The substrate is marked in grey. The surface layer in (c) is a thin PB layer.

As previously observed the perpendicular lamellar orientation persists in very similar P(S-*b*-B) thin films after a few days of thermal treatment at 150°C.[52,60] This is in contradiction to the results described in the present work where the lamellar structure vanishes after ~45 min at 130°C. This difference may be due to subtle differences in the sample characteristics and preparation, e.g. the substrate properties, the initial lamellar structure, the amount of antioxidant, and the exact conditions of the thermal treatment, such as high vacuum or N_2 atmosphere, heating and cooling rate, and duration. Since the present study was carried out with a systematic change of treatment temperature, leaving all other parameters unchanged, we conclude that under these conditions, the described structural changes are reliable. The P(S-*b*-B) system may be particularly sensitive to slight differences in the sample preparation and the treatment procedure, because the interfacial interactions of PS and PB are quite similar, and entropy plays an important role.

Chapter 4

Structural changes during solvent vapour treatment

Solvent vapour treatment is a commonly used technique to anneal defects in block copolymer thin films present after spin-coating[67,68,69,70,71,72,22]. The solvent enters the polymer film, where it has two effects: It decreases the repulsive interaction between the two blocks, and it increases the mobility of the (glassy) blocks[25]. Regarding the lamellar morphology, it is mainly controlled by the overall degree of polymerization, N, the volume fraction of one of the blocks, ϕ, the selectivity of the solvent towards the two blocks and the Flory-Huggins segment-segment interaction parameter χ between the two blocks as well as confinement effects[50,45,46,1,47,48]. As a function of the selectivity, the degrees of swelling of the two domains will differ which affects e.g. the mobility of the two blocks in different ways.

In the present chapter, we focus on the conditions during solvent vapour treatment and subsequent drying, in particular on the rate of swelling and the final degree of swelling of the film (SB28) as well as on the rate of drying. Papadakis *et al* have carried out in-situ, real-time investigations of the structural changes in block copolymer thin films during solvent-induced swelling of lamellae-forming poly(styrene-*b*-butadiene) employing in-situ, real-time grazing-incidence small-angle X-ray scattering. They first focused on experiments with saturated solvent vapour, where different solvents were applied: toluene, a good and non-selective solvent for both blocks, [51,22,41] and cyclohexane which is a theta solvent for PS and a good solvent for PB.[25] The liquid solvents were injected directly into the cell, therefore during the evapouration, the solvent vapour was used in combination with an N_2 flow to treat the samples. In thin films with initially perpendicular lamellae, the exposure to toluene vapour induced a transition from a 2D powder structure, i.e. lamellar domains with a preferential orientation perpendicular to the surface but randomly oriented within the film plane, to a more bulk-like 3D powder, i.e. lamellar domains having all possible orientations, on a time scale as short as a few minutes.[51] The exposure to toluene vapour of thin films with initially *parallel* lamellae induced a complex behavior: a destabilization of the structure was observed during the first few minutes, i.e. the

break-up of the existing lamellae and the formation of additional lamellae.[22] These latter findings lead them to the conclusion that upon solvent uptake more coiled molecular conformations are reached. Since the more coiled block copolymers require a higher interfacial area, this can only be accommodated via the creation of additional lamellae and therefore a reorganization of the entire stack of lamellae. The lamellar thickness follows initially $D_{lam} \propto \phi^{-0.74}$ and later $D_{lam} \propto \phi^{0.35}$ with D_{lam} the lamellar thickness of the parallel lamellae and ϕ the polymer volume fraction. The mean-field predictions $D_{lam} \propto \phi^{-1}$ and $D_{lam} \propto \phi^{1/3}$ [73,74] are thus only qualitatively recovered with the deviation being largest in the swelling regime. The appearance of a transient state on a time-scale of a few minutes was a new finding and indicates that thin film kinetics needs to be probed in-situ and in real time. However, it was unclear whether the deviations are due to kinetic effects since the entire process span only on a few minutes.

Subsequently, Papadakis *et al* studied a thin lamellar P(S-*b*-B) film in which, in contrast to the previously studied samples, the lamellae were initially not well oriented.[25] This allowed them to follow the appearance of long-range order during vapour treatment. They carried out in-situ, real-time GISAXS measurements during the exposure to saturated cyclohexane vapour (slightly selective to polybutadiene). Different processes were observed: First, the glass transition of the PS domains is crossed, enabling the lamellar film to rearrange by orientating the lamellae parallel to the film surface and by forming additional lamellae. Then, the order-to-disorder transition is crossed, and the film becomes disordered. Again a transient state of improved order is present, as in the case of toluene described above. The behavior of the lamellar thickness follows initially $D_{lam} \propto \phi^{-0.76\pm0.11}$ and later $D_{lam} \propto \phi^{0.27\pm0.04}$, i.e. it initially swells at very low solvent concentration and later shrinks. Again, there is a significant deviation from the mean-field prediction $D_{lam} \propto \phi^{-1}$ in the initial regime. Instead of swelling the film in small steps across the maximum of D_{lam}, it was already encountered *during* the first step. Moreover, the drying process was not followed in time.

In another study, the swelling of a thin film of lamellae-forming poly(styrene-b butadiene) in cyclohexane vapour was investigated[75]. Here, the degree of swelling of the film was increased in a stepwise manner and the resulting structural changes during and after each step were followed in-situ using time-resolved GISAXS. During the first step, the lamellar thickness increases strongly, before it decreases again, meanwhile a sharp maximum is present for the full width at half maximum (FWHM) of the diffuse Bragg reflection along the film normal. This is an evidence of formation of new lamellae. However, in this case, the behavior deviates from earlier theoretical predictions. A complex structural changes during swelling of a lamellar P(S-*b*-B) film featuring initially a bimodal distribution of lamellar orientations with a preference for the parallel orientation was observed. In non-saturated vapour, maximum swelling

was reached earlier than in saturated CHX vapour, and the formation of new lamellae then dominated which resulted in a rapid decrease of D_{lam}. Therefore, in non-saturated vapour, during the first step, the swelling occurs too fast and the lamellar thickness overshoot strongly.

In the present research, we chose a different approach. The vapour pressure of CHX was increased continuously by means of a completely customized solvent vapour treatment setup equipped with a bubbler, which allow a very precise control between each single step of the vapour and drying treatment, i.e. controllable rates of swelling and of drying. CHX was chosen because the structural changes were found to proceed more slowly than in toluene, and it is thus easier to follow them in detail. Moreover, by using a different procedure for substrate cleaning, the roughness and surface energy of the substrate are more well-defined than in the previous experiments. This way, the initial lamellar structure is more well-defined.

4.1 Experimental procedure and results

At the beamline D1 at CHESS, the film thicknesses of the films were monitored in-situ during vapour treatment and drying using a FilMetrics F30 spectroscopic reflectometer. At the beamline BW4 at DESY, a white-light interferometer (NanoCalc 2000, Ocean Optics) was used. The measuring time was 1 s. The film thickness was measured in-situ once per second through a glass window in the lid of the sample cell using the white light interferometer. When fitting the optical reflectance curves measured in a wavelength range of 400-900 nm, the refractive index of the sample was assumed to be 1.5. The resulting film thickness, D_{film}, was converted to the polymer volume fraction, $\phi = D_{film}^{dry} / D_{film}$, where D_{film}^{dry} is the film thickness in the as-prepared, unswollen state. To determine the degree of film swelling we used the relation $\left(D_{film}(t) - D_{film}^{dry}\right) / D_{film}^{dry} \times 100\%$.

The P(S-*b*-B) thin film studied by us forms lamellae in the bulk, and during vapour treatment contains a certain fraction of CHX. For randomly oriented lamellae, rings of high intensity (diffuse Debye-Scherrer rings, DDSRs) around the direct beam and around the specularly reflected beam are expected.[60] The distribution of lamellar orientations is reflected in the intensity distribution along the ring. However, dynamic effects in the grazing-incidence scattering geometry must be taken into account: For a completely random distribution of lamellar orientations, the intensity along the

DDSR is not homogeneously distributed (in contrast to transmission scattering), but is maximum near the Yoneda peaks appearing at the q_z values corresponding to α_{cP} and α_{cS} and decays towards high q_z.[76] In addition, the DDSrs are distorted from their circular shape.[77] In case the parallel lamellar orientation prevails, i.e. a high fraction of lamellae have their interfaces parallel to the film surface, the intensity of the DDSR around $q_y = 0$ is largely increased. This part of DDSR and its tangent is called diffuse Bragg sheet (DBS). Using the distorted-wave Born approximation (DWBA), the lamellar thickness of parallel lamellae, D_{lam}, can be deduced from the q_z position of the DBSs:

$$D_{lam} = \frac{2\pi}{\sqrt{(q_z - k_{iz})^2 - k_{c,film}^2} \pm \sqrt{k_{iz}^2 - k_{c,film}^2}}, \tag{4.1}$$

here, $k_{iz}=k_0\sin\alpha_i$ is the z-component of the incoming beam and $k_{c,film}= k_0\sin(\alpha_{c,film})$ with $k_0=2\pi/\lambda$. α_i is the incidence angle of the X-ray beam with respect to the film surface. With $\alpha_{c,film}$ the critical angle of total external reflection of P(S-*b*-B), possibly containing CHX. m is the order of the reflection. In case of symmetric lamellae (where the PS- and the PB-rich parts are equally thick, namely $D_{lam}/2$), m takes only odd values. For each value of m, two peaks denoted 'minus branch (M)' and 'plus branch (P)', are expected, which correspond to the DDSRs centered on the direct beam (M) and the beam reflected from the substrate (P), respectively.

For the presently studied samples, the lamellae which are parallel to the film surface prevailed and played a key role during the reconstruction in vapour. We therefore focused on the parallel lamellae. To gain more detailed information of the parallel lamellae, intensity profiles along q_z were created from the experimental 2D GISAXS maps by averaging over a narrow q_y range (-0.0051 Å^{-1} < q_y < 0.0039 Å^{-1}), centred at the maximum intensity along q_z, right behind the beamstop.

We quantified the FWHMs of the P1 peak along q_z by fitting a modified Gaussian, i.e. the plus branch of the first order peak, in the intensity profiles. The P1 peak was chosen because it is the most intense peak and does not overlap with the specularly reflected beam or the Yoneda region at any time. The profiles were found to be fitted well by the following function, a combination of a Gaussian and the Fresnel reflection function:

$$I(q_z) = \frac{1}{(q_z - q_{zS})^4} \times \frac{A}{\omega\sqrt{\pi/2}} \times \exp\left[-2\frac{(q_z - q_{z0})^2}{\omega^2}\right] + I_0 \tag{4.2}$$

Here, q_{zS} is the q_z position of the specularly reflected beam, q_{z0} the q_z position of the DBS, ω =0.849 × FWHM and I_0 a constant background.

The FWHM give information on the average number of correlated lamellae within the film[76].

To gain information on the correlated roughness of the lamellar interfaces[78], intensity profiles along q_y were created from the experimental 2D GISAXS images by averaging over a q_z range width 0.015 Å^{-1} centered at the P1 peak. Lorentzian functions were fitted to them to quantify the FWHM of the peak:

$$I(q_y) = I^* \Big/ \left[1 + 4\left(\frac{q_y - q_{y1}}{w} \right)^2 \right] \tag{4.3}$$

where q_{y1} is the peak position, w the FWHM and I^* the amplitude

The conversion of the 2D images from pixels to q-values as well as the construction of 1D profiles and the peak fitting were carried out using the GISAXS Analysis Package, written by us within the Igor Pro development environment.

Several versions of the sample cell and gas handling system were used. In all cases, the sample cell had Kapton windows for the incoming and scattered radiation. It was connected to a gas handling system, allowing the remote control of the flow of the CHX vapour and the dry gas (N_2). All tubes were made from PFA and all connections from stainless steel. The initial, rough flow meter (outside the hutch) was connected to the gas supply (typically 1.3 bar at D1 and 1 bar at BW4) by a long tube. Afterwards, the gas line was split into two, one being connected directly to the cell and one to the bubbler, a flask of volume 40 ml which contained 20 ml of liquid CHX. Valves allowed to control these two gas flows. The bubbler was connected to a three-way valve which allowed to install the desired gas flow and make sure that it is stable before opening the valve to the sample cell. This defined the beginning of the vapour treatment. The tube between the bubbler and the cell typically had a length of 50 cm. For swelling, a gentle stream of gas was guided through a pipe of inner diameter 6 mm into the bubbler. The flow was adjusted such that a certain number of bubbles per second (1 bubble/second or 3 bubbles/second, which corresponds to 0.4 l/h or 1.2 l/h) was flowing through the bubbler. Once the flow was adjusted, it was lead into the cell. The film swelling was adjusted by means of the nitrogen gas flow through the cell which could be varied between 0 and 3 l/h. The higher the gas flow, the lower was the local vapour pressure at the sample.

The interior dimensions of the vapour chamber used at D1 are the following: length along the beam 48 mm, width perpendicular to the beam 57 mm, and height 38 mm. The overall volume of the vapour cell used at BW4 is 20% bigger than the one used at D1.

Different conditions for the vapour treatment and drying were tested by means of three different customized setups, 1, 2 (Figure 4.1, inset), and 3 (Figure 4.1) in order to implement the best protocol for the structural ordering of the block copolymers. In all cases, two cycles of vapour treatment were performed. At the beamline D1 at CHESS switchable, not adjustable, valves were installed in order to open and close

the vapour (Figure 1, inset): setup 1. The sample was kept in vapour for 40 min at a CHX rate of 1.2 l/h, then it was dried for 30 min at an N_2 rate of 1.2 l/h. A second cycle of vapour was performed with the same condition of the first one, whereas the second drying took the same time of the first one but with a much lower N_2 flow rate of 0.4 l/h. At the beamline BW4 at DESY, different conditions were chosen. The first experiment was performed with the same setup and similar conditions of the one at CHESS (Figure 4.1, inset), but this time the the experimental cell had a larger volume: setup 2. The flow rate was set to be 0.4 l/h for both the CHX and N_2 streams, meanwhile the time of treatment was 45 min for both the vapour and drying. A second cycle took place with the same identical conditions of the first one. In order to improve the control on the degree of swelling of the thin block copolymer films, we installed two variable valves which allowed us to precisely set the flow rate of both CHX and N_2 (Figure 4.1): setup 3. The vapour treatment was accomplished by flowing N_2 gas at 0.4 l/h into the bubbler with liquid CHX. Therefore, from the bubbler a very gentle stream of CHX vapour was flowing into the experimental cell. For this setup we built two dedicated lines for the N_2 and CHX, respectively. This allowed us to drastically reduce any possible backflow resulting from the mixing of the two lines.

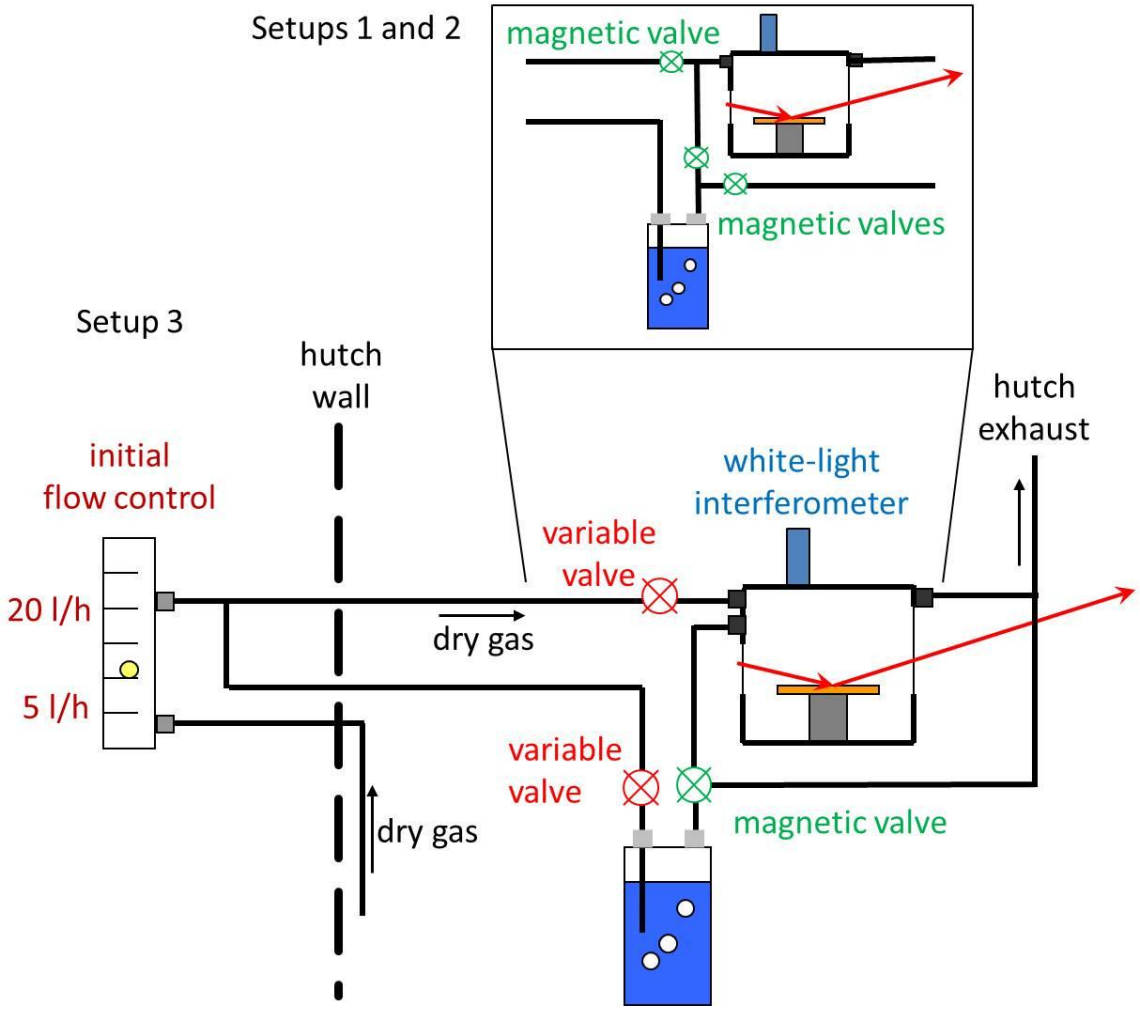

Figure 4.1. Schematic of the set-up for vapour treatment and drying employed for in-situ measurements at the beamline BW4, HASYLAB at DESY, during the experiment employing variable valves, namely setup 3. The inset shows the different valve type and arrangement used at the beamline D1 at CHESS and at the beamline BW4, HASYLAB at DESY, during the first experiment, which employed no variable valves, namely setups 1 and 2 respectively.

The as-prepared films had thicknesses of 2150 $\pm$ 200 Å, as determined using white-light reflectometry and XR.

The bulk structure of the as-prepared films was determined using small-angle X-ray scattering (SAXS) with synchrotron radiation. The inset in figure 4.2 shows the typical 2D SAXS-profiles observed for the as-prepared film, whereas in figure 4.2, the corresponding spectral averaged profile is presented. The bulk structure of the P(S-*b*-B) shows three strong diffraction peaks, which by means of the Bragg-equation allow calculating the layer distance and determining the bulk morphology. The relations between the first and the second *Bragg* peaks are 1:2. This ratio indicates the presence of a lamellar structure[79], confirming the GISAXS observations. The corresponding layer spacing amount to 195 ± 2 Å. Dividing the film thickness by this value, we obtain the maximum number of stacked lamellae $N_{lam} = D_{film} / D_{lam}^{bulk} = 11$.

The GISAXS map of the as-prepared film (Figure 4.1a) shows, apart from the specularly reflected beam at q_z = 0.0293 Å^{-1}, the Yoneda peaks of the polymer film and the Si substrate at 0.0257 Å^{-1} and 0.0297 Å^{-1}, respectively. Moreover, it features one pair of DDSRs along the q_z axis at ~0.05-0.07 Å^{-1}. These are the first-order DDSRs from randomly oriented lamellae. Second-order DDSRs are not present since the lamellae are symmetric with equally thick PS and PB blocks, as expected for di-block copolymer with symmetric composition. The intensities of the DDSRs are strongly enhanced near q_y = 0 (DBSs), i.e. a significant fraction of the lamellae is parallel with respect to the Si substrate.

Intensity profiles along q_z were created by integrating over the stripe between the blue vertical lines in Figure 4.3a. This profile (Figure 4.3b) shows the pair of peaks (the plus, P1, and minus, M1, branch of the first order DBS) in addition to the specularly reflected beam (S). Fitting Eq. 4.2, to the P1 peak, D_{lam}^{dry} = 145 ± 1 Å was obtained. D_{lam}^{dry} is lower than D_{lam}^{bulk}. Apart from the DDSRs and the DBSs, oscillations

between the Yoneda peak of the polymer and of the substrate are clearly visible, indicative of a well-defined and smooth film surface.

The XR curve (Figure 4.4a, lower curve) shows a number of Kiessig fringes. A good fit was obtained for a homogeneous film with a SLD of 1×10^{-5} Å^{-2}, a thickness of 1950±20 Å and a surface roughness of 20 ± 4 Å (Figure 4.4b). The SLD of the polymer film is close to the expected value. The film thickness is consistent with the results from white-light interferometry.

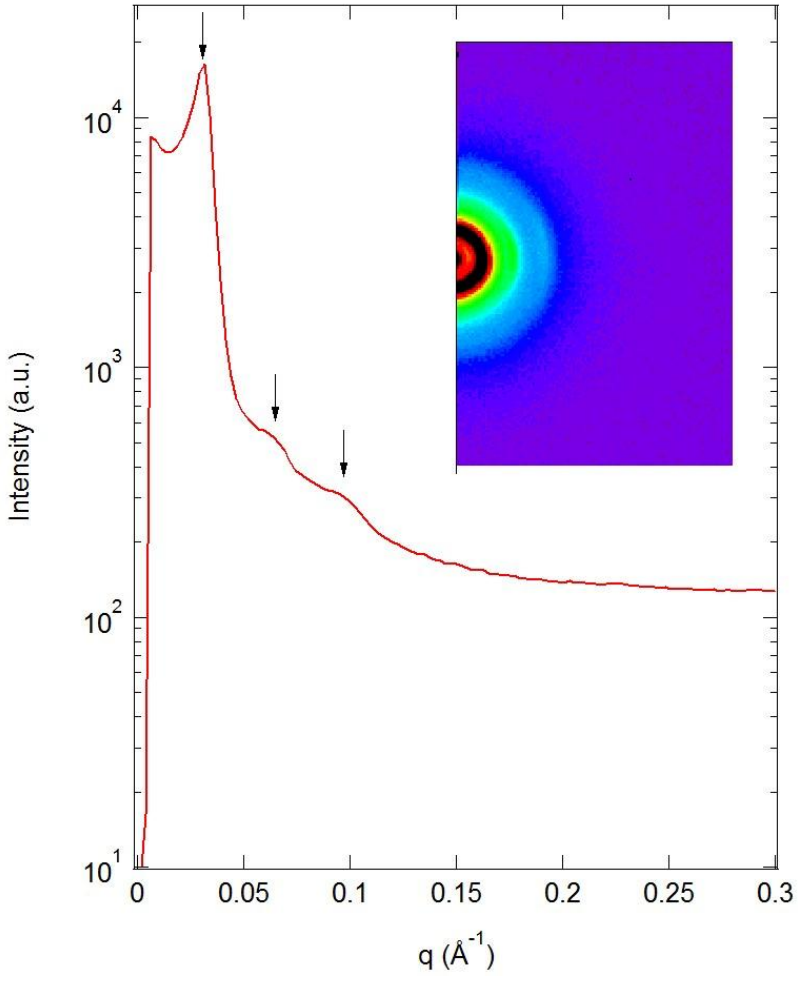

Figure 4.2. 1D intensity profile obtained from a spectral average of the 2D SAXS image (inset) of the as-prepared film. The measuring time was 10 h. The arrows mark the positions of the 1st, 2nd and 3rd order Bragg peak.

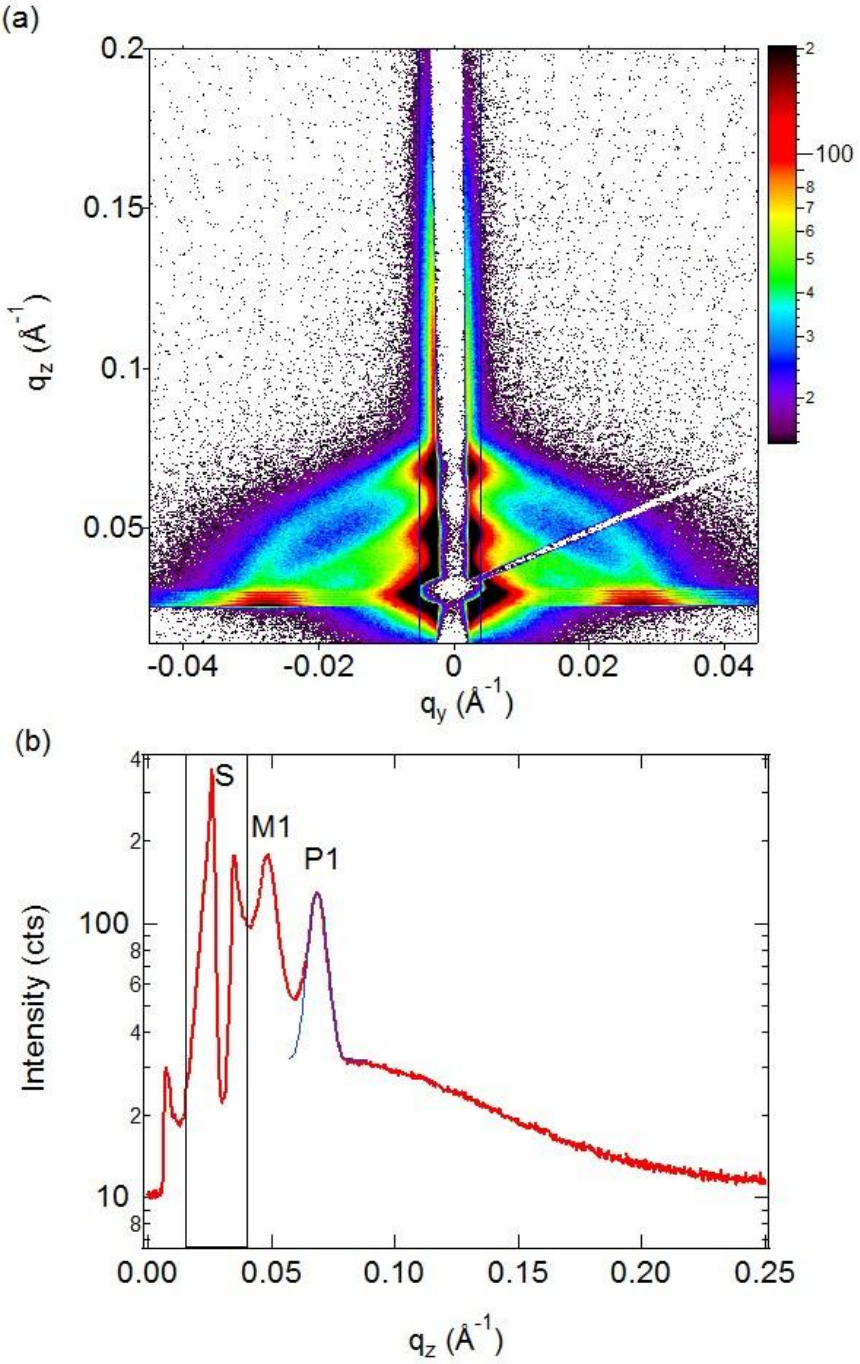

Figure 4.3. (a) 2D GISAXS image of the as-prepared film at α_i = 0.18°. The measuring time was 300 s. The ring-like features are due to the diffuse Debye-Scherrer rings, centered at the direct beam and the specularly reflected beam. The white regions are due to the beamstops. The blue vertical lines in the GISAXS images show the region used to construct the intensity profiles along q_z. (b) 1D GISAXS intensity profile along q_z for the as-prepared film. S, M1 and P1 mark the positions of the specularly reflected beam, partially hidden by the beamstop (enclosed within the black box), and the minus and plus branch of the first-order

DBS, respectively. The fit for the P1 peak curve, obtained using eq. 4.2, is shown as a thin blue line over the experimental curve.

The three different setups previously described were used in order to perform three different experiments, respectively. For each experiment, the 2D GISAXS maps related to two cycles of vapour and drying treatment are shown in Figure 4.6. A schematic which represents the time evolution of the flow rates into the cell is shown in Figure 4.5.

Setup 1 was employed at beamline D1 at CHESS, the CHX flow rate was kept at a constant value of 1.2 l/h for 45 min (Figure 4.5a, left). In this time, the film thickness increased from 2050 Å to 3030 $\pm$ 20 Å, i.e. the degree of swelling amounted to 48 % and ϕ decreased from 1 to 0.677 (Figure 4.8a). GISAXS images were taken continuously every 10 s throughout the whole time. For drying, the CHX line was closed and, at the same time, the N_2 line was opened, letting the dry N_2 gas flow directly into the cell for 50 min at a rate of 1.2 l/h. At the end of the drying process, the film thickness was back to the original value of 2050 $\pm$ 20 Å. Then, a second cycle of vapour treatment and subsequent drying was performed. In this case the CHX flow rate was kept at a constant value of 1.2 l/h for 50 min. At the end of the vapour process the film thickness reached the maximum value of 2950 $\pm$ 20 Å, i.e. the degree of swelling amounted to 44 % and ϕ decreased to 0.695. For drying, N_2 gas flowed directly into the cell for 45 min at a rate of 0.4 l/h. At the end of the drying process, the film thickness was back to the original value of 2050 $\pm$ 20 Å. After 45 min of vapour treatment the GISAXS map shows 2nd order DBSs, pointing to an asymmetry of the swelling process (Figure 4.6a). Since CHX is slightly selective to the PB blocks, the PB layers presumably swell more than the PS layers. Meanwhile, the 1st order DBSs are bending. As previously observed,[22] the bending of the DBSs is mainly due to the formation of additional lamellae, following the reduction of the effective Flory-Huggins segment-segment interaction parameter between the two blocks, χ_{eff}, and the more coiled molecular conformation of the two blocks. In fact, the presence of solvent in the lamellar morphology screens the repulsive interaction between the PS and PB blocks. It is, therefore, possible that, upon solvent uptake, χN reaches the value where the ODT is expected, 10.5. Since CHX is only slightly selective to the PB block, we can assume to be in presence of a non-selective solvent, in this case χ is replaced by $\chi_{eff} = \phi\chi$.[80] We have found that ϕ of P(S-*b*-B) decreases with time (Figure 4.8a), reaching a value which is lower than 0.78 where the glass transition is expected, ϕ_g.[81] Below ϕ_g the polymer mobility increases and a large scale reorganization of the lamellar blocks occurs, eventually resulting in a

longer range order of the lamellae along a direction parallel with respect of the Si substrate. Upon drying, the DDSRs from randomly oriented lamellae disappear and only DBSs are present, showing that the majority of the lamellae are now oriented parallel with respect to the Si substrate. The overall degree of orientational order has thus improved. A second cycle of vapour is then performed. In this case, the GISAXS map does not show any evidence of bending of the DBSs or of the presence of DDSRs due to tilted lamellae: instead the 1^{st} and 2^{nd} order DBSs are now well-defined. This means a more stable state of the lamellar structures after the 1^{st} cycle of annealing. A second drying at a N_2 flow rate of 0.4 l/h induced the weakening of DBSs. The absence of DBSs lead to two possibility: The structures in the film are present with a very short-range order which induce the complete absence of any DBSs; or the structures are perfectly ordered to an extent that any kind of GISAXS signal araising from them is collected behind the beamstop and therefore not visible in our images. In order to discriminate between these two possibilities we performed in-situ XRR on this sample, which clearly show an improvement of the lamellar orientation along the direction parallel to the Si substrate after each vapour/drying cycle (Figure 4.7). Bragg reflections are evident after each drying, pointing to an ordering of the lamellae along the direction parallel to the substrate. Nevertheless, the absence of any DBS higher order point out to a local improvement of the lamellar order.

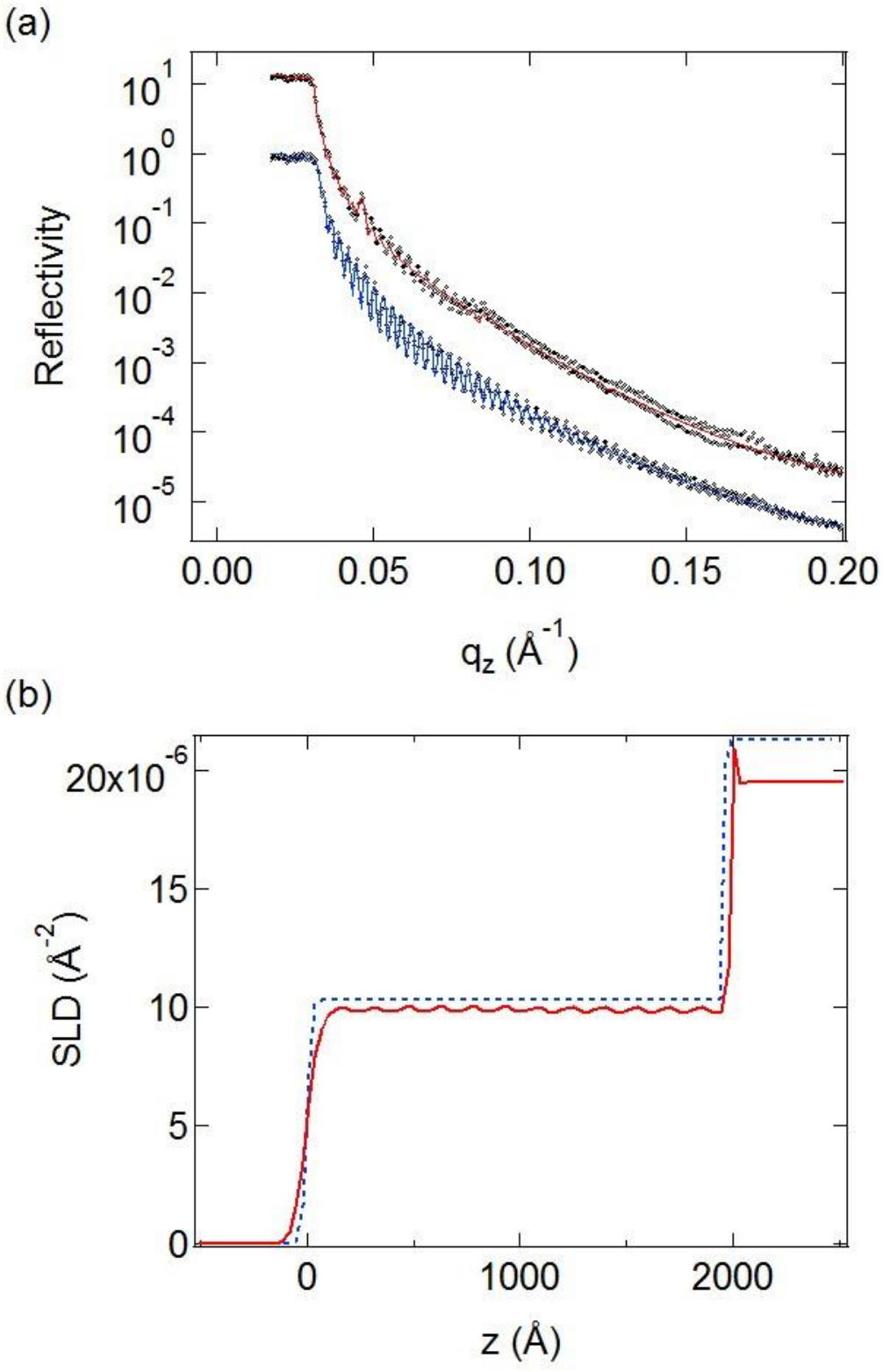

Figure 4.4. (a) Ex-situ XR curves of the as-prepared film (lower blue curve) and films after two cycles of CHX treatment using the setup 3 (second curve from below, red). Symbols: experimental curves; lines fitted model curves. The curves were shifted vertically by a factor of 5, respectively. (b) Corresponding SLD profiles of the as-

prepared film (blue dashed line) and the films after two cycles of CHX treatment using the setup 3 (red solid line).

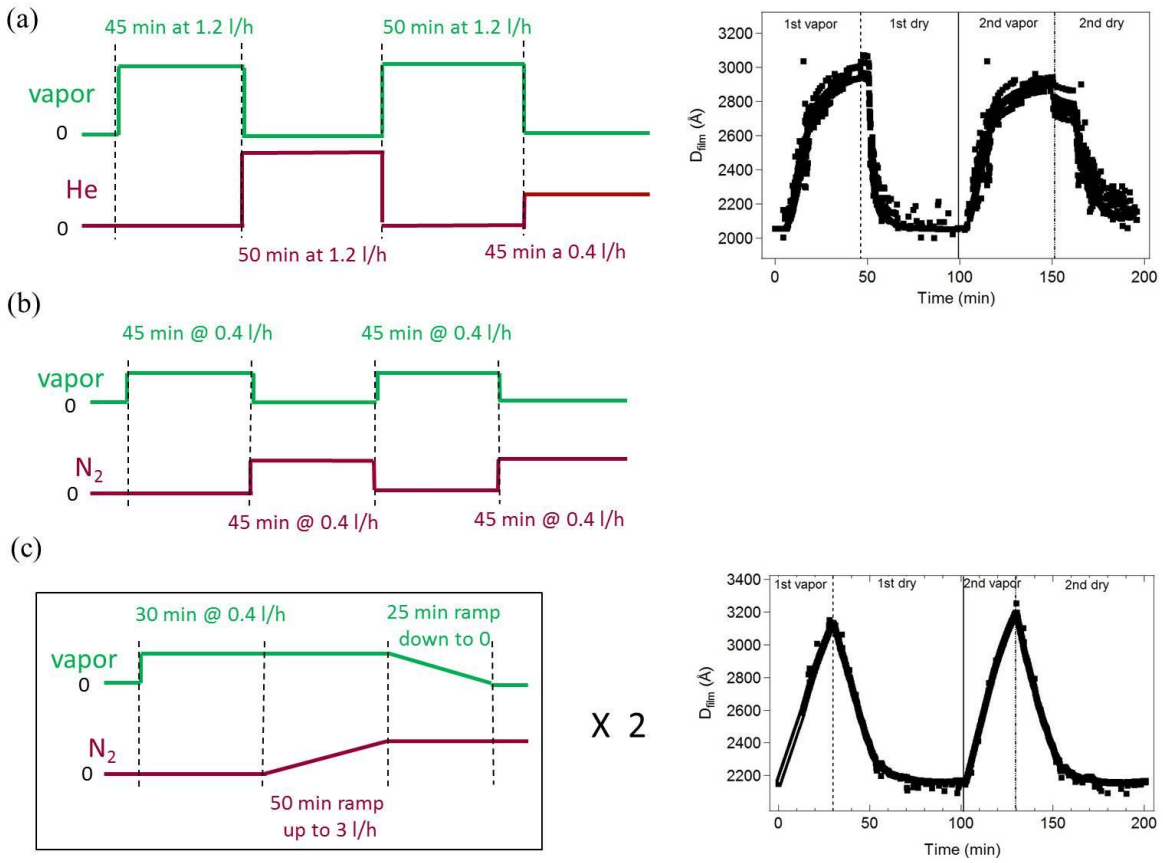

Figure 4.5. (a) Protocol used with the setup 1 (left) and relative film thickness, D_{film} (right), In the case of the D_{film} curve, the vertical dashed, solid and dash-dotted lines indicate the start of the first drying, the second vapour treatment and the second drying, respectively. (b) Protocol used with the setup 2. (c) Protocol used with the setup 3 (left) and relative film thickness, D_{film} (right), in this case the same protocol is applied for both the first and second cycle. The white line on the top of the D_{film} data points marks the region where interpolated data substitute the missing data points.

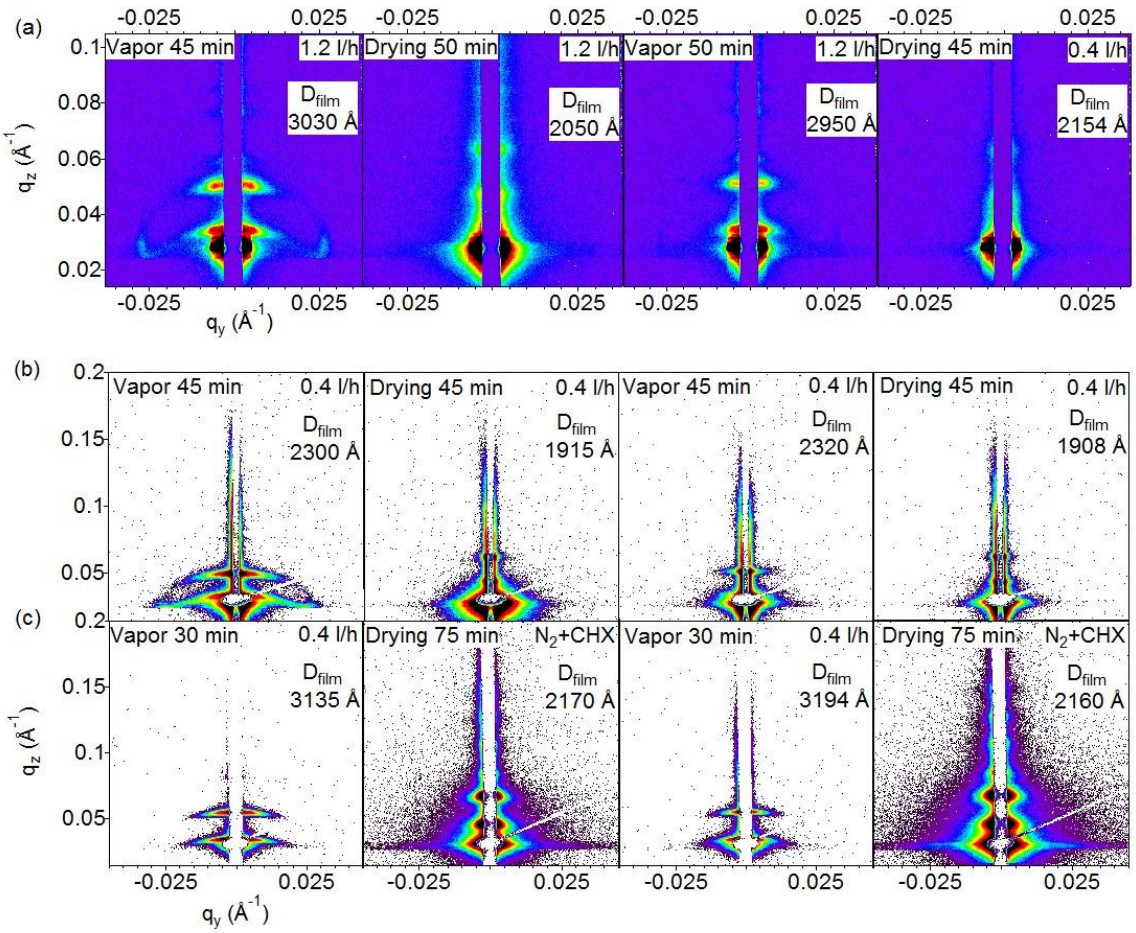

Figure 4.6. Representative GISAXS images of the film during the first and second cycle of CHX vapour treatment and subsequent drying for three different treatment conditions. Experiment at D1, CHESS (a), at BW4 at HASYLAB, DESY (b,c). For each experiment, we show four GISAXS images, all taken in-situ (from left to right): at the end of the first cycle of the vapour treatment, after the first drying, at the end of the second vapour treatment and after the second drying. Times and flow rates of vapour treatment and drying as well as the resulting film thicknesses are indicated in the images. The film thicknesses of the as-prepared samples in (a) and (c) were 2150 $\pm$ 20 Å, for the sample in (b) it was 1900 $\pm$ 20 Å. The color scale for all GISAXS pictures is the same as in figure 4.3(a). The different color, background and the smaller *q*-range of the GISAXS maps in (a) than the ones used in the other GISAXS images are due to the different detectors employed at the two different beamlines. The measuring time was 10 s for the pictures in (a), 300 s for (b) and 300 s for the dry pictures in (c), instead for the pictures in (c) taken during the vapour treatment the measuring time was 30 s. The incident angles were set to be 0.16° for the experiment in (a) and 0.18° for the experiments in (b) and (c).

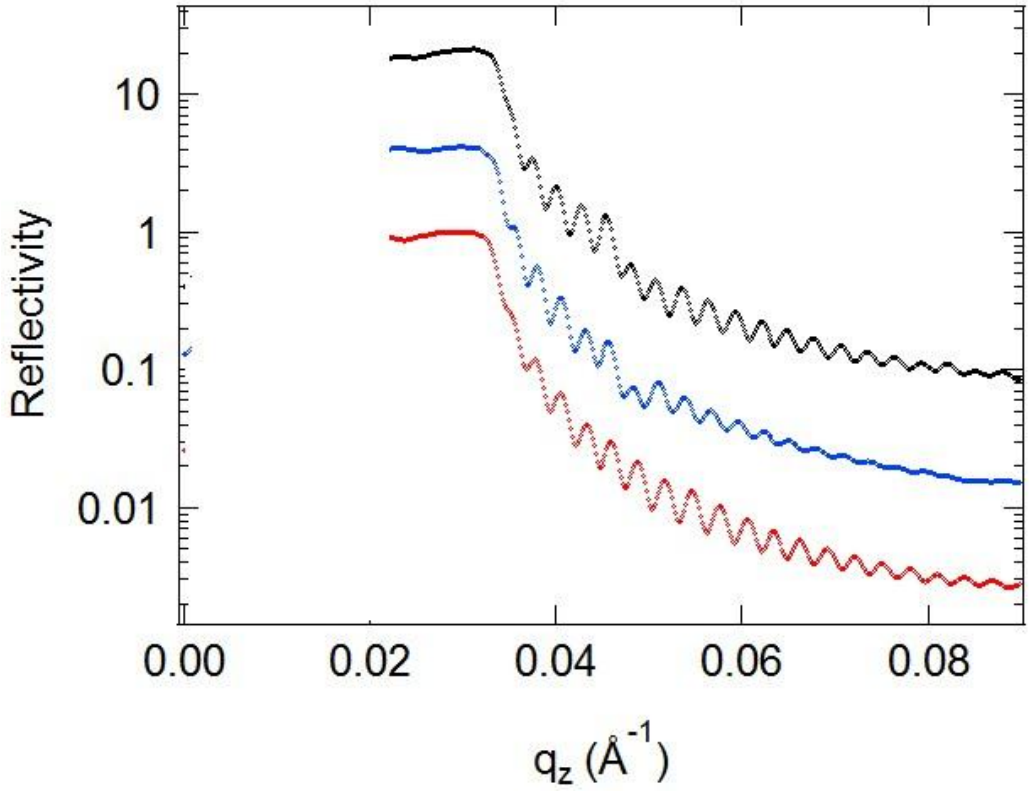

Figure 4.7. (a) In-situ XR curves obtained during vapour treatment at D1 using the setup 1 are shown: as-prepared (lower, red), after 1st drying (middle curve, blue) and after 2nd drying (upper curve, black). The curves were shifted vertically by a factor of 5, respectively.

The different swelling of the film during the first and second cycle (Figure 4.5, right), is due to the different flow rate installed during the second vapour treatment, which evidently allows a better control of the system. Therefore we made use of this experience in a second experiment, at beamline BW4, where the setup 2, which is similar to the one used in the first experiment, was employed. The CHX flow rate was kept at 0.4 l/h for 40 min (Figure 4.5b). As a consequence, the film thickness increased within 45 min from 1900 to 2300 $\pm$ 20 Å, i.e. the maximum degree of swelling was 21 %, and ϕ decreased from 1 to 0.826. GISAXS images were taken continuously every 30 s. The following drying process was started by closing the CHX line and opening the N_2 line at the same time, letting it flowing directly into the cell. The N_2 stream was kept at a value of 0.4 l/h for 45 min. At the end of the drying

process, the film thickness was back to the original value of 1915 ± 20 Å, so the initial film thickness was recovered. A second cycle of vapour treatment and subsequent drying was performed, with a maximum degree of swelling equal to the one in the first cycle.

At the end of the first vapour treatment, the GISAXS map shows only 1st order DBSs which are broad along q_y along with 1st order DDSRs (Figure 4.6b). We attribute these features to undulations and to the presence of tilted lamellae. We recall that the glass transition of the PS layer is presumably not crossed because the solvent content is too low: ϕ decreased only to 0.826 which is higher than the value of ϕ_g. This means the the block copolymers stay tethered to the lamellar interface. The lamellar interface per polymer can only be increased by undulations, large scale reorganization with a formation of additional lamellae is not possible. These undulations lead to broadening of the DBSs.[22] Moreover, the existing randomly oriented lamellae do not reorient, thus the DDSRs stay unchanged from the as-prepared state.

After drying, the DDSRs from randomly oriented lamellae disappear, and only DBSs are present in the GISAXS image. The majority of the lamellae are now only locally oriented parallel with respect to the Si substrate, since large scale reorganization does not occur during the vapour process, as evident from the presence of only the 1st order DBS after drying, meanwhile higher orders are absent. The DBSs are now less elongated along q_y, i.e. the undulations present in the swollen state have vanished, and the interfacial area per chain is decreased again.

At the end of the second vapour treatment, the DBSs are not bent, and no DDSRs are present, but in this case only the 1st order DBSs is present. This point out to the presence of less tilted lamellae than during the first cycle of vapour treatment, but confirm that the mobility of the polymer is sufficient only to induce a local reorganization of the lamellae along the direction parallel with respect to the Si substrate, since again there is no evidence of higher order DBSs. The second drying does not induce any change to the DBSs compared to the first cycle, due to the low polymer mobility of the whole system.

The vapour treatment induces large scale rearrangement of the lamellar structure along an energetically stable preferential direction only when the copolymer mobility is reached, i.e. the glass transition temperature of PS is crossed. In this case $\phi > \phi_g$, therefore the system was not sufficiently swollen and the lamellae could not reorganize on large scale along a direction parallel with respect to the Si substrate.

Comparing the results with the previous experiment at beamilne D1 we conclude that two concurrent processes have to be taken into account in order to induce a long range order of the lamellar structures: the rate of the swelling and the degree of swelling. In fact, at D1 we observed that a large scale reorganization occurs since $\phi <$

ϕ_g, i.e. the degree of swelling was sufficient to promote a lamellar rearrangement along the parallel direction, but the swelling rate was too fast to induce a stable long range formation of lamellae along the direction parallel to substrate interface; to the other hand, at BW4 we observed that controlling the swelling rate is crucial but not sufficient to induce long-range ordering of the lamellae if the degree of swelling is insufficient to let such a reorganization to occur. This brought us to the conclusion that a more accurate contro on the degree and rate of swelling was necessary. Therefore we implemented a new setup (setup 3) equipped with adjustable valves in order to fulfill these requirement and induce a controlled long range reorganization of the lamellar structures.

By means of this new setup which allows for adjustable flow rates of the vapour and the dry gas, a more controlled and very slow drying process was established (Figure 4.6c). In fact, we noticed that in the case of the setups 1 and 2, when switching over from vapour treatment to drying, a backflow of vapour into the dry gas line was present. By means of the setup 3 this effect was drastically reduced. In the remainder, we will focus on the analysis of the experiment presented in Figure 4.6c, where, after a vapour treatment with a sufficiently high degree of swelling, a slow and controlled stepwise drying was carried out, and a stable, long-range order was achieved. The vapour treatment was carried out at a CHX flow rate of 0.4 l/h for 30 min (Figure 4.5c, left). The film thickness increased from 2150 to 3135 $\pm$ 20 Å (Figure 4.5c, right), i.e. the degree of swelling was 46 %, and ϕ decreased from 1 to 0.686 (Figure 4.8b). GISAXS images were taken continuously every 30 s throughout the whole time. The subsequent drying process was carried out by keeping the vapour flow constant at 0.4 l/h and, at the same time, increasing the content of pure N_2 gas step by step using an adjustable valve from zero to 3 l/h within 50 min. Again, N_2 was flowing directly into the sample cell. This decreased the film thickness to 2185 $\pm$ 20 Å. To dry the film completely, the CHX vapour flow was decreased step by step to 0 l/h which took 25 min. At the end of the drying process, the film thickness was back to the original value of 2170 $\pm$ 20 Å. A second, identical cycle of vapour treatment and subsequent drying was performed, with a degree of swelling very similar to the one monitored during the first cycle.

At the end of the first vapour treatment, the GISAXS map shows 1st order DBSs which are broad along q_y (Figure 4.6c) but no DDSRs. The absence of the DDSRs means that the tilted lamellae have disappeared, whereas the broadening of the DBSs is due to undulations of the lamellar interfaces. $\chi_{eff}N$ is reduced to 17.8 at the end of the vapour treatment (Figure 4.8b), therefore the enthalpic penalty for the creation of additional lamellar interfaces is decreased. The copolymers inside the thin film are now assuming a more coiled molecular conformation than in the dry state. Therefore each copolymer requires now an increased interfacial area, which then induces the formation of additional lamellae. At the same time, the T_g(PS) has been crossed at an extent which allow proper mobility to the polymers and therefore a

large scale reorganization occurs, but preserving the lamellar state, since the ODT is not crossed. After the first drying, three orders of the DBSs are present, i.e. long-range order of the parallel lamellae is achieved. At the end of the second vapour treatment, the broadening of the DBSs is reduced compared to the one after the first vapour treatment. The lamellar interfaces are thus more smooth at the end of the second vapour treatment than after the end of the first vapour treatment. After the second drying, the three orders of DBSs are more intense than after the first drying. The presence of higher and more pronounced DBS orders point to the achievement of longer range order of the lamellar structures along the parallel direction with respect to the Si substrate.

This confirms our expectations, since a proper control on the degree and rate of swelling of the whole system is now achieved by means of the setup 3 and the lamellae can be now reorganized along the direction parallel with respect to the Si substrate on a larger scale, therefore obtaining a long range ordering.

The different degrees of maximum swelling encountered during the experiments are due to the different setups used for the experiments themselves: the volume of the experimental cell used in the third experiment was larger than the one used in the first experiment . Moreover, due to the installation of a second inlet for the dry gas directly at the sample cell, backflow effects present during the first and second experiment Figure 4.6a,b) were suppressed.

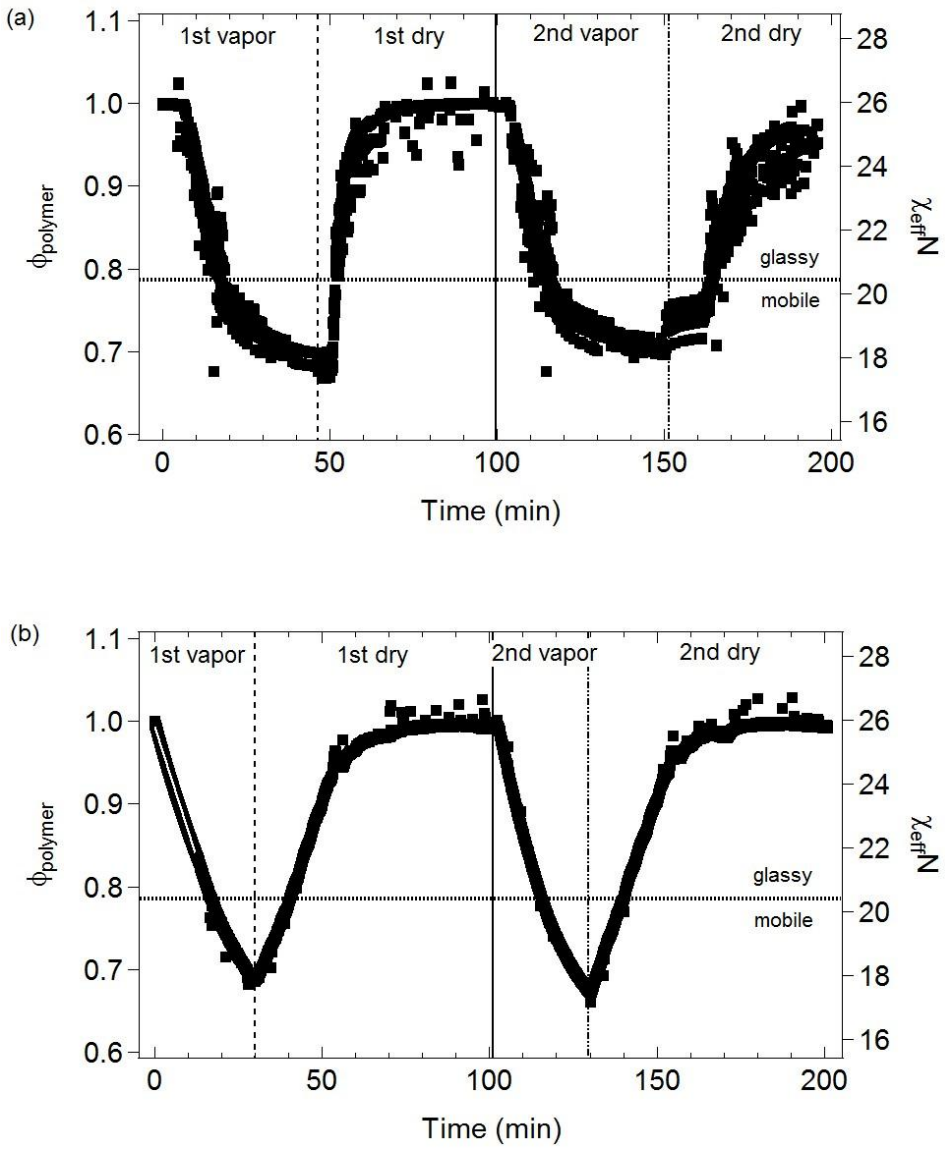

Figure 4.8. (a) Volume fraction ϕ (left axis) and $\chi_{eff}N$ (right axis) of P(S-*b*-B) as a function of time at D1 and (b) at BW4, making use of the setup 3. The vertical dashed, solid and dash-dotted lines indicate the start of the first drying, the second vapour treatment and the second drying, respectively. The horizontal dashed line divide the PS glassy region when $\phi > \phi_g = 0.78$ and PS mobile region where $\phi < \phi_g = 0.78$. The white line on the top of the experimental data points in (b) marks the region where interpolated data substitute the missing data points.

The detailed structural changes of the sample presented in Figure 4.6c during vapour and drying treatment have been monitored as a function of time. The GISAXS images taken during the first vapour treatment and the subsequent drying process are shown in Figure 4.10. During the first 20 min of vapour treatment, the DDSR becomes weaker, thus randomly oriented lamellae vanish. A pronounced broadening and bending of the DBSs becomes evident which is especially pronounced after 20 min. This is mainly due to the formation of additional lamellae (lenses), i.e. a large scale reorganization of the block structures takes place in the presence of solvent. These changes become possible once the glass transition of PS is crossed (Figure 4.8b). In the remaining time of the first vapour treatment, the 1st order DBSs become sharper along q_z and more straight along q_y. Upon drying, the 1st order DBSs become more narrow along q_y which indicates that the undulations become less pronounced. Moreover, a pair of 2nd order DBSs appears after 5 min of drying (Figure 4.12), which reflects an asymmetric swelling of the PS and the PB layers with parallel orientation. This is in accordance with the selectivity of CHX towards PB, inducing the PB layer to absorb more CHX vapour than the PS layer. After ~10 min of drying, 3rd order DBSs appear, i.e. the correlation of the lamellar interfaces improves, followed by the vanishing of the 2nd order DBSs after 20 min of drying (Figure 4.9b). This means that the state with asymmetric swelling of the two blocks is a transient one. At the end of the drying process, however, all the three order DBSs are back (Figure 4.9a). The presence of three orders of DBSs points to the achievement of a long range order of the parallel lamellae with respect to the Si substrate.

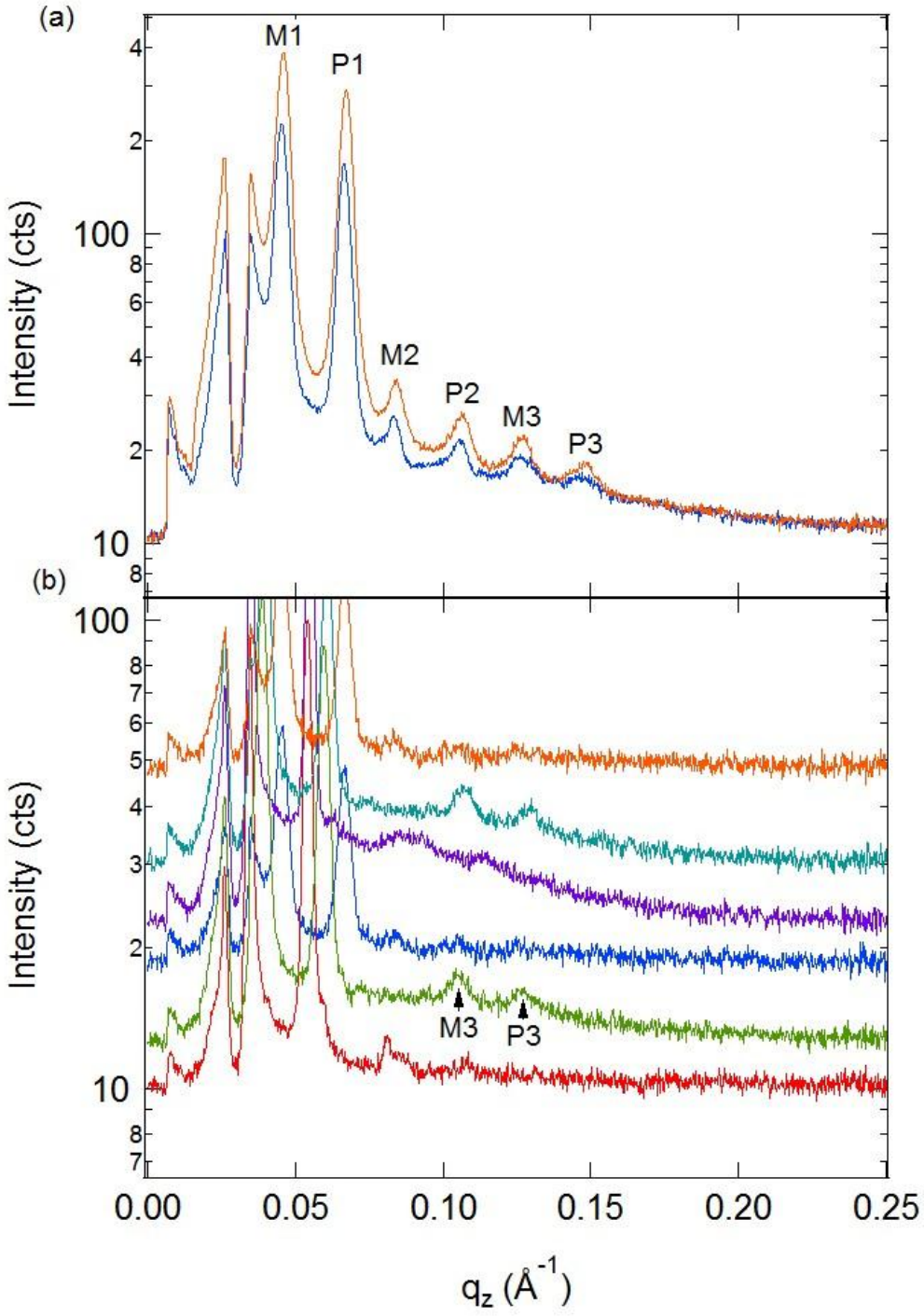

Figure 4.9. (a) 1D GISAXS intensity profiles along q_z for the film after the first and second drying, red and blue curve respectively. The measuring time was 300 s. (b) Selected 1D GISAXS intensity profiles along q_z for the film after 30 min of vapour treatment, after 20 min of drying, after complete drying for the first and second cycle, bottom to top. The measuring time was 30 s. Same notation and cutting region as Figure 4.3.

A second cycle of vapour treatment and subsequent drying was performed (Figure 4.11), with qualitatively the same behavior as in the first one. Starting from more well-oriented lamellae than after spin-coating, the broadening of the DBSs is now less pronounced, which is also an evidence that a more equilibrated state is reached after the first cycle. Again within 20 min of drying the same behavior than in the first cycle is observed for the 2nd and 3rd order DBSs, with a transient asymmetric swelling followed by a symmetric swelling (Figure 4.9b). At the end of the 2nd vapour and drying cycle, the three orders of DBSs are more pronounced than the ones after the first cycle (Figure 4.9a), which points out to an even more pronounced improvement of the long range order of the parallel lamellae.

The behavior of the positions and shapes of the DBSs can be followed more clearly looking at the intensity profiles along q_z (Figure 4.12) and q_y (Figure 4.13).

During the first 15 min of the 1st vapour treatment, only the 1st order DBSs are visible (Figure 4.12), which move toward lower q_z-values within the 30 min of the vapour treatment. This means that the lamellae swell. Meanwhile, in the q_z region where 2nd and 3rd order DBSs are expected, a shoulder extending to high q_z values is present which may be due to roughness or inhomogeneities of the film surface.[82] Shortly after the drying is started, higher order DBSs become evident and follow the behavior of the 1st order DBSs: all move toward higher q_z-values, i.e. the lamellae shring, and stabilize after 40 min of drying, i.e. the lamellar thickness becomes constant. During the second vapour treatment, the DBSs follow the same behavior as during the first cycle. Moreover, this time is possible to monitor the behavior of the 2nd and 3rd order DBSs even during the vapour treatment. The reason is that the shoulder of high intensity along q_z affecting the first vapour treatment is not present any longer. Again, all DBSs follow the behavior, moving toward lower q_z-values within the 30 min of vapour treatment. The DBSs are thus affected earlier than in the first drying treatment. After the first annealing, the lamellar structure is now closer to equilibrium and the correlation of the lamellae along the film normal is better. This allows the blocks to swell in a more symmetric way and the solvent to escape faster from the film. An advantage of the thin film geometry is that the solvent molecules take only short time (10 μm in 0.1 s)[83] to travel through the whole D_{film} than in the thicker films, i.e. no gradient of solvent concentration is present.

The intensity profile along the q_y-direction centered at the position of the P1 peak gives information on the lateral directions (Figure 4.13). It is possible to monitor the time evolution of the fwhm of the P1 peak as function of the vapour and drying treatment, which then give information on the correlated roughness of the lamellar interfaces. In the first 10 min of vapour the fwhm is stable, then start to increase becoming very broad after 20 min of treatment. Upon drying the fwhm of the P1 peak decrease drastically already after 5 min and then start to stabilize after 10 min of drying.

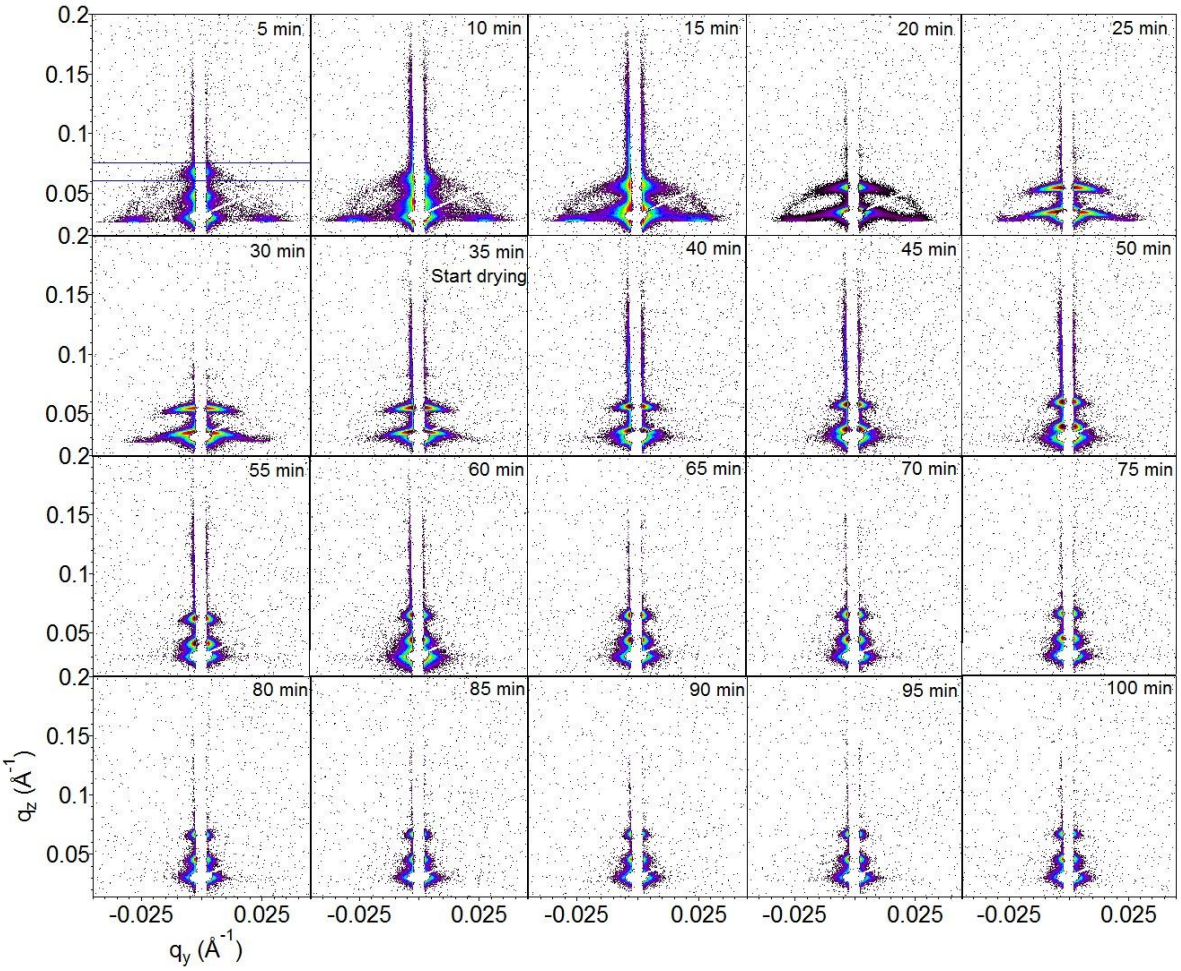

Figure 4.10. Representative GISAXS images of the film during the first cycle with CHX vapour and subsequent drying. The times after the solvent vapour starts entering the cell are given in each image. Drying starts after 30 min by starting a controlled flow of N_2 gas and slowing decreasing the solvent vapour flow. The measuring time was 30s. For all images, the color scale and the regions used to construct the intensity profiles are the same as in Figure 4.3a q_z. The blue horizontal lines in the first GISAXS images show the regions used to construct the intensity profiles along q_y.

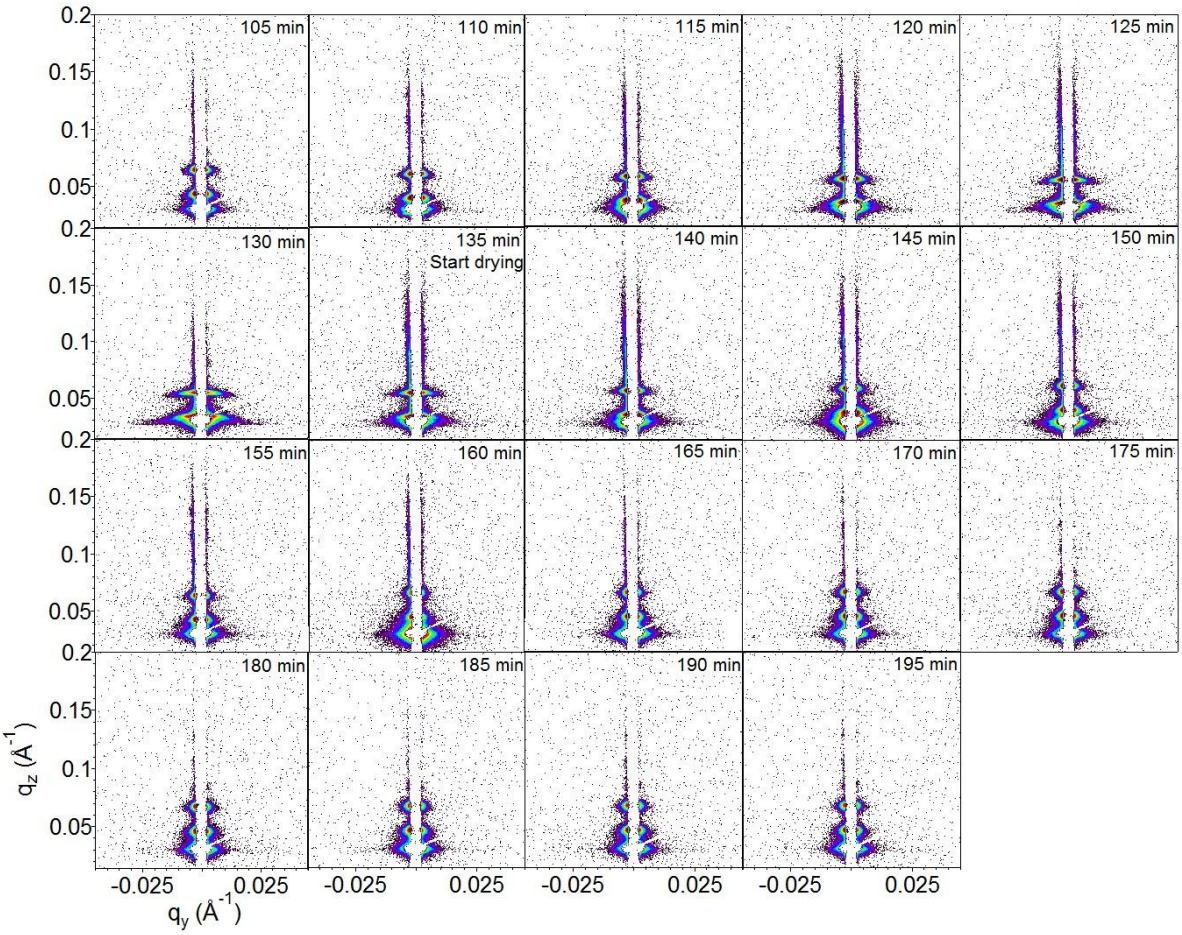

Figure 4.11. Representative GISAXS images of the film during the second cycle with CHX vapour and subsequent drying. Same scale and notation as in Figure 4.10.

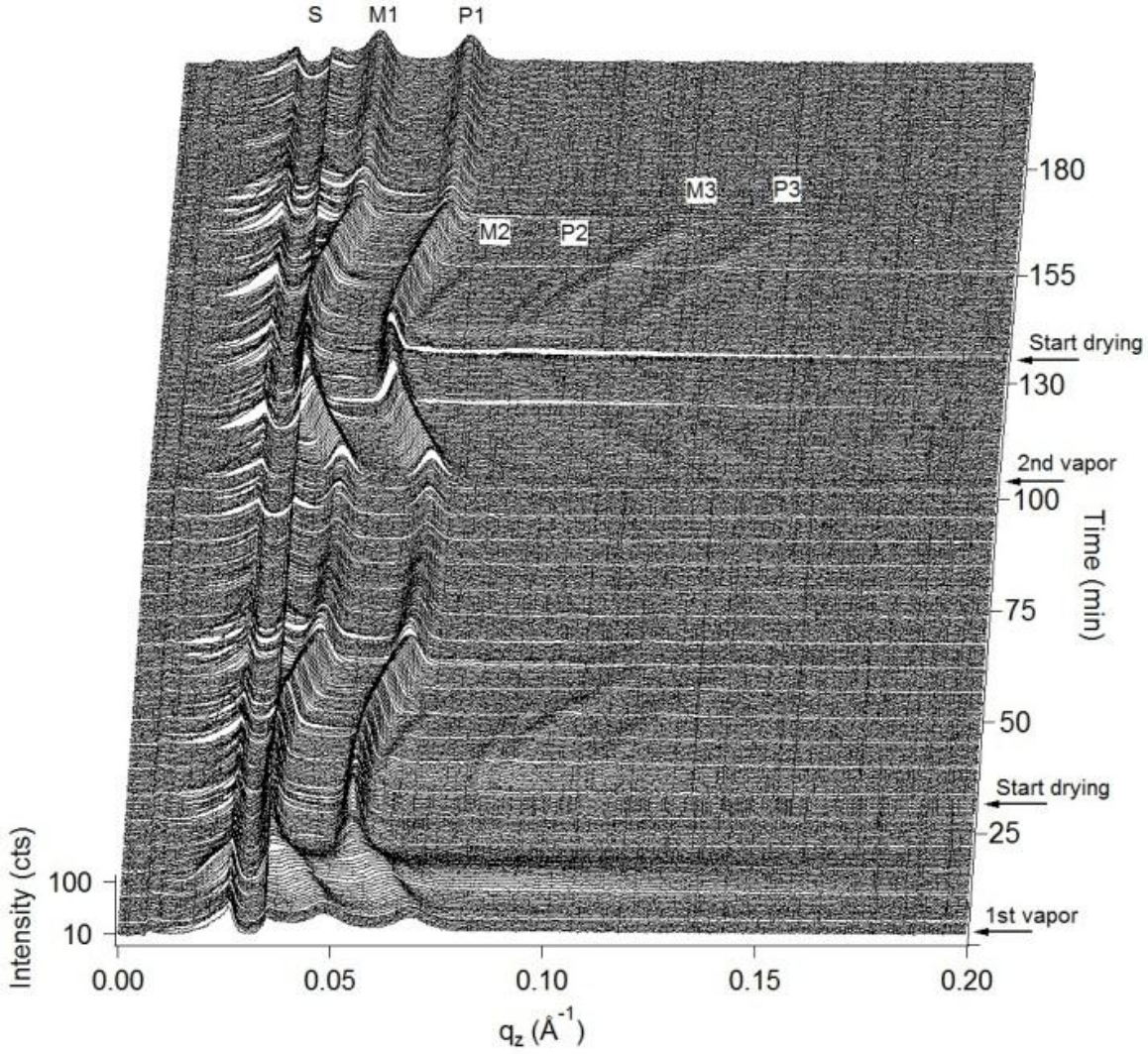

Figure 4.12. Intensity profiles related to the first and second cycle of vapour treatment and subsequent drying, along q_z (through the DBS) as a function of time, centered at q_y = -0.0006 Å^{-1}. S, M and P mark the position of the specularly reflected beam, the minus and plus branches of the DBSs, respectively. The drying starts at the marked position.

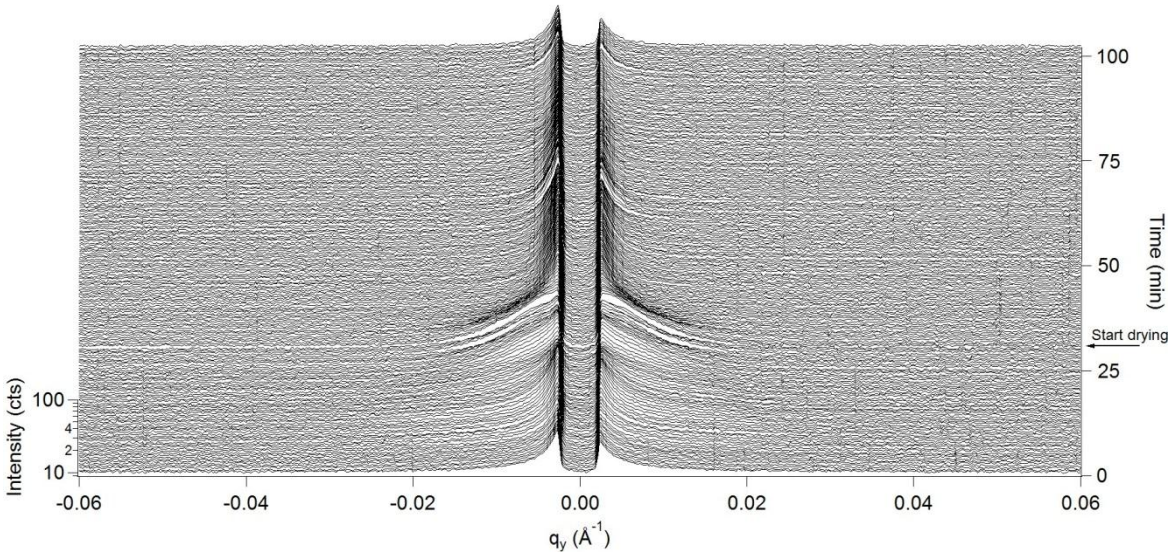

Figure 4.13. Intensity profiles related to the first cycle of vapour treatment and subsequent drying, along q_y centered at the position of P1 and integrated over a q_z-width of 0.015 Å^{-1}. The drying starts at the marked position.

The cutting along q_y and q_z directions were then quantified in order to obtain information about the lamellar thickness, the number of correlated lamellae and the correlated roughness of the lamellar interfaces as function of time of the vapour and drying treatment (Figure 4.14). The P1 peak was analyzed by means of the equations 1 and 2 in order to gain information related to the D_{lam} and N_{corr} (Figure 4.14a,b) and by fitting Lorentzian to the peak along the q_y direction in order to obtain the fwhm, i.e. the correlated roughness of the lamellar interfaces (Figure 4.14c).

D_{lam} of the parallel lamellae resemble a similar behavior already observed for the D_{film}. Within 20 min D_{lam} increases from 145 to 222 ± 1 Å and slightly stabilize around this value, till the drying is started (Figure 4.14a). This behavior it is similar to previous experiments on similar systems where only the vapour treatment effects on thin films of P(S-*b*-B) is studied[25]. Upon drying, D_{lam} rapidly decreases reaching a value of 157 ± 1 Å after 35 min of drying and stabilizing at the minimum value of 152 ± 1 Å after 60 min. This value is slightly lower than the one for the bulk, but higher than the initial value. In contrast a not monotonous behavior is observed in the case of the fwhm reflecting the behavior of the N_{corr} (Figure 4.14b). In fact, during the vapour treatment, the fwhm first decrease reaching the minimum value of 0.0037 ±

0.0001 $Å^{-1}$ within 8 min and subsequently increases reaching a maximum value of 0.0056 ± 0.0001 $Å^{-1}$ within 14 min from the starting of the vapour, then a monotonous behavior take place leading the fwhm to reach a minimum value of 0.00175 ± 0.0001 $Å^{-1}$ after 22 min of vapour treatment and keeping this stable value till the drying process starts. Upon drying, for approximatively 8 min the fwhm does not change, meanwhile D_{lam} was instead decreasing, then it increases reaching a stable maximum at 0.00275 ± 0.0001 $Å^{-1}$ after 30 min of drying, pointing out an improvement on the correlation of the parallel lamellae. A second vapour and drying treatment was performed and if for D_{lam} the behavior reproduce the one for the 1st cycle, but never reaching again a minimum value as the one observed for the as prepared film; in the case of the the number of correlated lamellae the behavior is very much different than the one monitored during the first cycle. In fact, upon the second vapour treatment N_{corr} increases reaching a maximum after 25 min of treatment, then it start to decrease again meanwhile it is still in vapour. When the drying take place the N_{corr} continue to decrease till reaching a stable minimum within 30 min of drying. Therefore the complex behavior observed in the first 15 min of the first vapour is now absent. Upon second drying, both D_{lam} and $N_{corr,}$ reproduce the same behavior already observed for the first drying. Therefore after the first annealing the correlation of the lamellae is improved and a more equilibrated state is reached.

The XR curve of the sample taken after two cycles of cycles of vapour treatment (Figure 4.4a, second curve from below), shows Kiessig fringes and Bragg reflections as well. From modeling, the polymer film appears made of 13 parallel lamellae each constituted by a PS block with a SLD of 1.0 $\times 10^{-5}$ $Å^{-2}$, a thickness of 45 $\pm$ 5 Å and roughness of 45 $\pm$ 5 Å and PB block with a SLD of 9.7 $\times 10^{-6}$ $Å^{-2}$, a thickness of 108 $\pm$ 5 Å and roughness of 20 $\pm$ 5 Å (Figure 4.4b). The thickness of the whole film is therefore very similar to the one of the as-prepared film and consistent with the interferometry measurements, meanwhile the roughness is increased, instead the lamellae thickness is matching the GISAXS results. The XR results therefore confirms that the vapour treatment of a thin P(S-*b*-B) film induces the formation of parallel lamellae oriented along the direction parallel with respect to the Si substrate.

To further understand the large scale rearrangement of the lamellae, occurring during vapour and subsequent drying treatment, we have studied the time evolution of the P1 fwhm cut along the q_y direction. During the first 10 min the fwhm stay at the constant value of 0.0035 ± 0.0003 $Å^{-1}$, then it suddenly increases reaching the maximum value of 0.01 ± 0.0003 $Å^{-1}$ at the end of the vapour treatment, pointing out a drastic decrease in the lateral length scale and therefore an increasing of the correlated roughness of the lamellar interfaces[78]. Therefore during this process formation of rippled lamellar interfaces occur. Upon drying, the fwhm decreases suddenly to the original value of the as-prepared film, whitin 10 min from the beginning of the drying process. Then a second regime take place, the fwhm continue to decreases but the process is slowed down, in fact it reaches a stable

minimum at 0.00105 ± 0.0003 $Å^{-1}$ within 40 min, a value lower than the one of the as-prepared film.

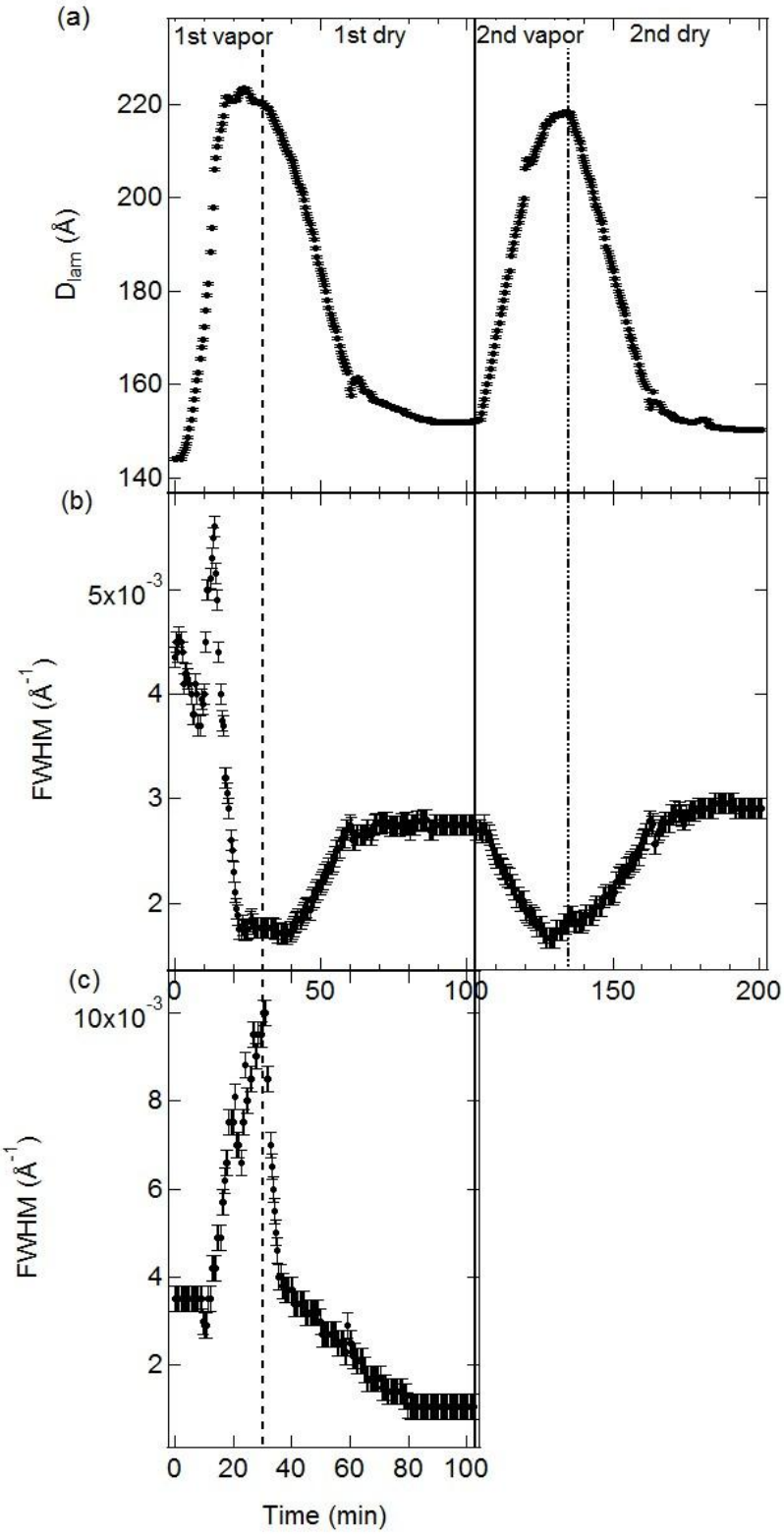

Figure 4.14. (a) Lateral repeat distance, D_{lam}, (b) fwhm along q_z, which is related to the number of correlated lamellae along the film normal, and (c) along q_y, which is related to the correlated roughness of the lamellar interfaces as a function of treatment time. Same notation as in Figure 4.

4.2 Conclusion

Our results can be, therefore, projected within the framework of the mean-field theory describing the behavior of the lamellar thickness as function of the polymer volume fraction[73] (Figure 4.15). During the first vapour treatment the initial data for $\phi_{polymer}$ are missed (points between the arrows in Figure 4.15), therefore they have been extracted interpolating the values from the collected experimental data. During the vapour process two regimes can be identified: in the high-concentration regime D_{lam} increases as $D_{lam} \propto \phi^{-4.16\pm0.13}$. Therefore, the swelling is faster than the uniaxial behavior predicted by the mean-field theory, $D_{lam} \propto \phi^{-1}$. This confirm the observation that randomly oriented lamellae are present but a minority within the whole film thickness of the as-prepared film, meanwhile parallel lamellae are the majority but short-range ordered, therefore forming small domains where the lamellae are locally ordered along the direction parallel with respect to the Si substrate (Figure 4.16a). When the vapour starts to enter the lamellar structures it induces a fast asymmetric swelling process, since only PB is sufficiently mobile at this stage, which leads to a large reorganization of the lamellae, therefore promoting a faster longer-range ordering of the parallel lamellae (Figure 4.16b). This swelling regime change when ϕ ~ 0.86, in fact in the low concentration regime D_{lam} stabilizes till ϕ ~ 0.8 when $D_{lam} \propto \phi^{0.1\pm0.01}$ till drying begin, i.e. the T_g(PS) is crossed and the polymer mobility increase, therefore the polymer coiling increases and additional lamellae are formed, meanwhile the lamellar order along the parallel energetically stable direction is mainly unchanged (Figure 4.16c). Upon drying, $D_{lam} \propto \phi^{-0.53\pm0.03}$ till ϕ ~ 0.93, therefore a process slightly slower than the uniaxial deswelling take place, since now, after the formation of additional lamellae, more lamellae are oriented along the direction parallel with respect to the Si substrate, therefore a symmetric and controlled swelling take palce. During the drying the PS is still mobile therefore the film to accommodate more lamellae in the same volume increases the sharpness of the interfaces, i.,e. longer-range order. Then $D_{lam} \propto \phi^{-2.78\pm0.1}$ till the end of drying process, which resemble the same behavior than the as-prepared film during the early stage of vapour treatment, therefore it is only the PB that in this ϕ range contribute to the swelling of the system. During the second cycle of vapour and subsequent drying

treatment, the system shows at beginning a different behavior during vapour, where $D_{lam} \propto \phi^{-1.16\pm0.01}$ is following the mean-field theory prediction in the case of high-concentration regime. In fact, now the lamellae are already long range oriented along the parallel direction, i.e. the PS block is long-range ordered in a glassy state, limiting the swelling rate. Moreover, now the number of lamellae is greater than the first cycle, therefore the solvent as to cross more interfaces and less voids, reducing the vapour diffusion time within the whole D_{film}. During the second vapour treatment, instead, D_{lam} does not show any evidence of a secondary regime as expected by the mean-filed theory in the case of low concentration. Therefore a stable condition is reached for the lamellae and no additional lamellae are formed, but only an uniaxial swelling occurs. Then during the drying the swelling process follows exactly the same behavior already observed in the case of the first drying.

Since the vapour of a good solvent enter the copolymer film only by means of voids already present, this induce no changes in the lamellar swelling at the very beginning of each vapour treatment.[84,85]

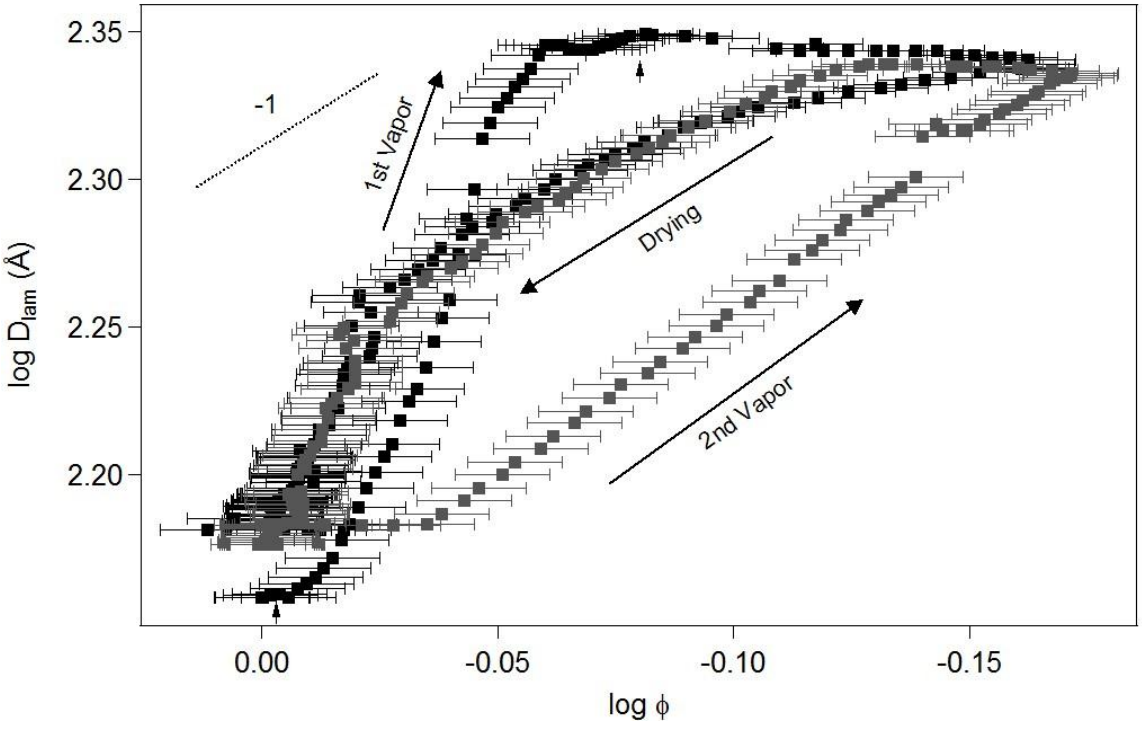

Figure 4.15. Double-logarithmic representation of D_{lam} as function of ϕ. The black markers are related to the the first cycle of the vapour and drying treatment, instead the grey ones are relative to the second cycle. The two vertical arrows mark the missing data points range of the first cycle, obtained interpolating the experimental data.

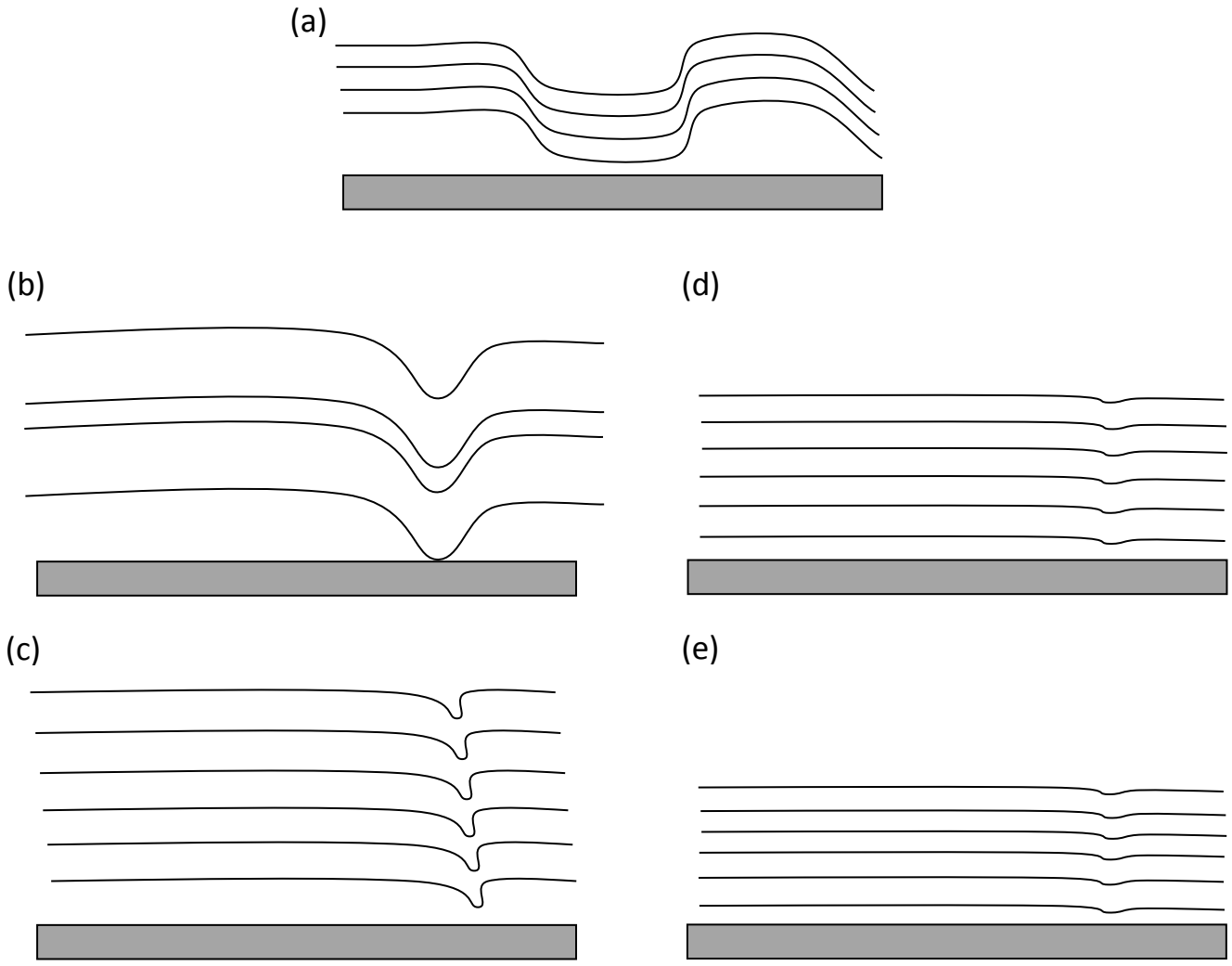

Figure 4.16. Sketch of the structure of the (a) as-prepared sample, (b) vapour treatment below ϕ_g(PS) and (c) above ϕ_g(PS). Drying process: (d) PS is still mobile; whereas (e) PS is in the glassy state. The short lines denote lamellar interfaces. For clarity, only few lamellar domains are shown. The substrate is marked in gray.

Chapter 5

Creation of lateral structure during solvent vapour treatment

As previously discussed, the thin film geometry allows detailed studies of the swelling and rearrangement during vapour treatment, because the structures may be oriented by the film surface and the film/substrate interface. Previous investigations on lamellar poly(styrene-*b*-butadiene) thin films after spin-coating[42] and during vapour treatment and subsequent drying[25,22,41] or heat treatment[86] have shown that, using in-situ, grazing-incidence small-angle X-ray scattering with 2D detection, a wealth of information is accessible, such as the lamellar orientation and its distribution as well as the lamellar thickness, i.e. the repeat distance and the number of correlated lamellae. Moreover, information about the lamellar roughness and undulations of the lamellar interfaces can be gained. Combining in-situ, real-time GISAXS with atomic force microscopy, which details the surface morphology, and X-ray reflectometry, which reveals the film thickness as well as possible layered structures inside the film, detailed information on the processes during vapour treatment and drying can be gained giving information on their molecular origin. Knowledge of the mechanisms and the kinetics of the processes during solvent vapour annealing plays an important role in the preparation of long-range ordered and regularly oriented structures thus enabling their application.

In the present chapter, we have examined a poly(4-octylstyrene-*b*-butylmethacrylate) (OB5) di-block copolymer. Previous investigations[1] showed that, in the bulk, it forms the lamellar structure after thermo-annealing. *n*-hexane (HX) – the solvent used for vapour treatment in the present study – dissolves lower and swells higher molar mass fractions of both POS and PBMA homopolymers.[1] It is thus close to non-selective for both blocks, but not a good solvent. Moreover, it was found using AFM that a thin film which has a featureless surface after the preparation forms perpendicular (or standing) lamellae after swelling in HX vapour for a few minutes and subsequent drying.[1] In contrast, acetone vapour treatment resulted in a parallel lamellar orientation. Acetone is a non-solvent for POS and a good solvent for PBMA, thus very selective for PBMA. The quality and selectivity of the solvent for the two blocks thus seem to be key parameters for the final lamellar orientation.

In the present work, the structural changes during vapour treatment of spin-coated films having different film thicknesses were followed using in-situ, real-time GISAXS. It was found that treatment with HX vapour results in the formation of lateral structures, as expected. The processes are complex, and the kinetics depends strongly on the film thickness.

5.1 Experimental procedure and results

In the present study, GISAXS measurements were performed and the resulting DDSRs were very weak and were only discernible from the background in the Yoneda band, thus their positions and radii cannot be read off at the q_z value of the specularly reflected beam. Instead, the intensity profiles along q_y were integrated over a stripe of a width along q_z of 0.003 Å^{-1} centered at the q_z position of the Yoneda peak of the polymer, where the scattering is most intense (Figure 2.9), namely at q_z = 0.028, 0.027 and 0.031 Å^{-1} for the thicker, the intermediate and the thin film, which were measured at α_i = 0.22°, 0.20°, and 0.25°, respectively. Their q_y-range covers -0.16 Å^{-1} to 0.16 Å^{-1}. The peak positions were determined by fitting Lorentz functions to the peaks on both sides of the scattering plane, including scattering peaks due to the Kapton windows used in our chamber:

$$I(q_y) = \frac{I_1}{1+4\left((q_y - q_{y1})/w_1\right)^2} + \frac{I_2}{1+4\left((q_y - q_{y2})/w_2\right)^2} + \frac{I_{DDSR}}{1+4\left((q_y - q_{y,DDSR})/w_{y,DDSR}\right)^2}, \quad (5.1)$$

where the first two terms describe the scattering of the Kapton exit windows of the flight tube, whereas the latter describes the first-order DDSR of the sample. q_{yi} and $q_{y,DDSR}$ are the peak positions (i = 1, 2), w_i and $w_{y,DDSR}$ the full widths at half maximum and I_i and I_{DDSR} the peak heights. For the precise determination of the $q_{y,DDSR}$ values, the fitting results from negative and positive q_y values were averaged. The systematic overestimation in the determination of the repeat distance, D_{lam}, by reading it off at the Yoneda position of SiO_x (Figure 2.9) is estimated below 1 Å at α_i = 0.20° (used for the intermediate film thickness), 3 Å at 0.22° (thick film) and 15 Å at 0.25° (thin film). This error only affects the absolute D_{lam} values; within each data set, the results are consistent. Also, the width of the ring is slightly overestimated.

Even in this case the number of correlated lamellae in the film plane, N_S, was estimated as follows:[16]

$$N_s \cong \frac{2.75}{\pi} \times \frac{q_{y,DDSR}}{w_{y,DDSR}} . \quad (5.2)$$

The lateral correlation length amounts to $N_S D_{lam}$.

The conversion of the 2D images from pixels to q values as well as the construction of 1D profiles and the peak fitting were carried out using the GISAXS Analysis Package, written by us within the Igor Pro development environment.

After alignment of the sample in the X-ray beam and GISAXS measurements of the as-prepared film, 2 ml of HX were injected into a reservoir in the sample cell through a Teflon capillary, and GISAXS images were taken subsequently with an exposure time of 60 s, while the film was immersed in saturated vapour. A custom-made vapour cell based on an aluminum cylinder equipped with a solvent reservoir was used to swell the film with HX vapour.[22,25] All measurements were carried out at room temperature (RT). The sample was kept in saturated vapour for ~45 min. Drying of the sample was carried out by flushing the sample cell with N_2 gas. Again, GISAXS images were taken in real time with an exposure time of 60 s. For the second vapour/drying cycle, the procedure was repeated. To avoid beam damage during the time-resolved GISAXS measurements, the sample was moved sideward after each measurement. After each vapour treatment and drying, the sample was realigned.

In a previous study,[1] it was found using AFM that the surface of a fresh dip-cast film having a thickness 500 Å was featureless. When the thin film was swollen by HX and subsequently dried, perpendicular (standing) lamellae were observed at the surface. To elucidate the mechanisms of structure formation, we have carried out time-resolved GISAXS measurements on three P(OS-*b*-BMA) films having similar or lower film thicknesses. This way, we get an insight into the role of the film interfaces. First, we confirm that the as-prepared samples do neither reveal any surface structure nor any inner structure on the length scales investigated. Afterwards, we present the GISAXS results from the three films during repeated vapour/drying cycles as well as the surface structures measured after one vapour/drying cycle. Finally, we discuss the role of the film thickness on the structure formation process.

The film thicknesses were determined using VIS interferometry. They were found at D_{film} = 520 ± 50 Å, 430 ± 50 Å and 350 ± 50 Å for films spin-coated at 1000 rpm, 2000 rpm and 3000 rpm, respectively. The film thicknesses thus amount to 2.0, 1.6 and 1.3× D_l^{bulk}, respectively. In the following, the films will be referred to as thick, intermediate and thin.

AFM images were taken of the three as-prepared films (Figure 5.1a-c), i.e. after spin-coating and drying at room temperature. They do not show any evidence of surface

order for the thick and the intermediate films (Figure 5.1a,b). Only in the thin film (D_{film} = 350 Å), small and weakly ordered lamellar domains are present at the surface (Figure 5.1c). (The phase images are featureless.) For lateral lamellar order, Bragg peaks are expected at k = 1/260 Å = 0.0038 Å^{-1}. For none of the three films, the 2D Fourier transforms (insets in Figure 5.1a-c) display distinctive features or do the corresponding 1D Fourier transforms show any peaks (not shown). The RMS surface roughnesses are 30 Å, 20 Å and 10 Å, for the thick, the intermediate and the thin film, respectively, thus much smaller than both D_{film} and D_{lam}.

GISAXS maps of the three as-prepared films (Figure 5.1d-f) do not show any features apart from the specularly reflected beam and diffuse scattering, which is presumably due to surface roughness and to weak internal structuring. The first-order Bragg peak from the lamellar structure is expected at $q_y = 2\pi/260$ Å = 0.024 Å^{-1}. The 1D intensity profiles (Figure 5.2), obtained by integrating over a stripe having a q_z width of 0.003 Å^{-1} centered at the q_z-positions of the Yoneda peaks of the polymer films, however, do not show any peaks.

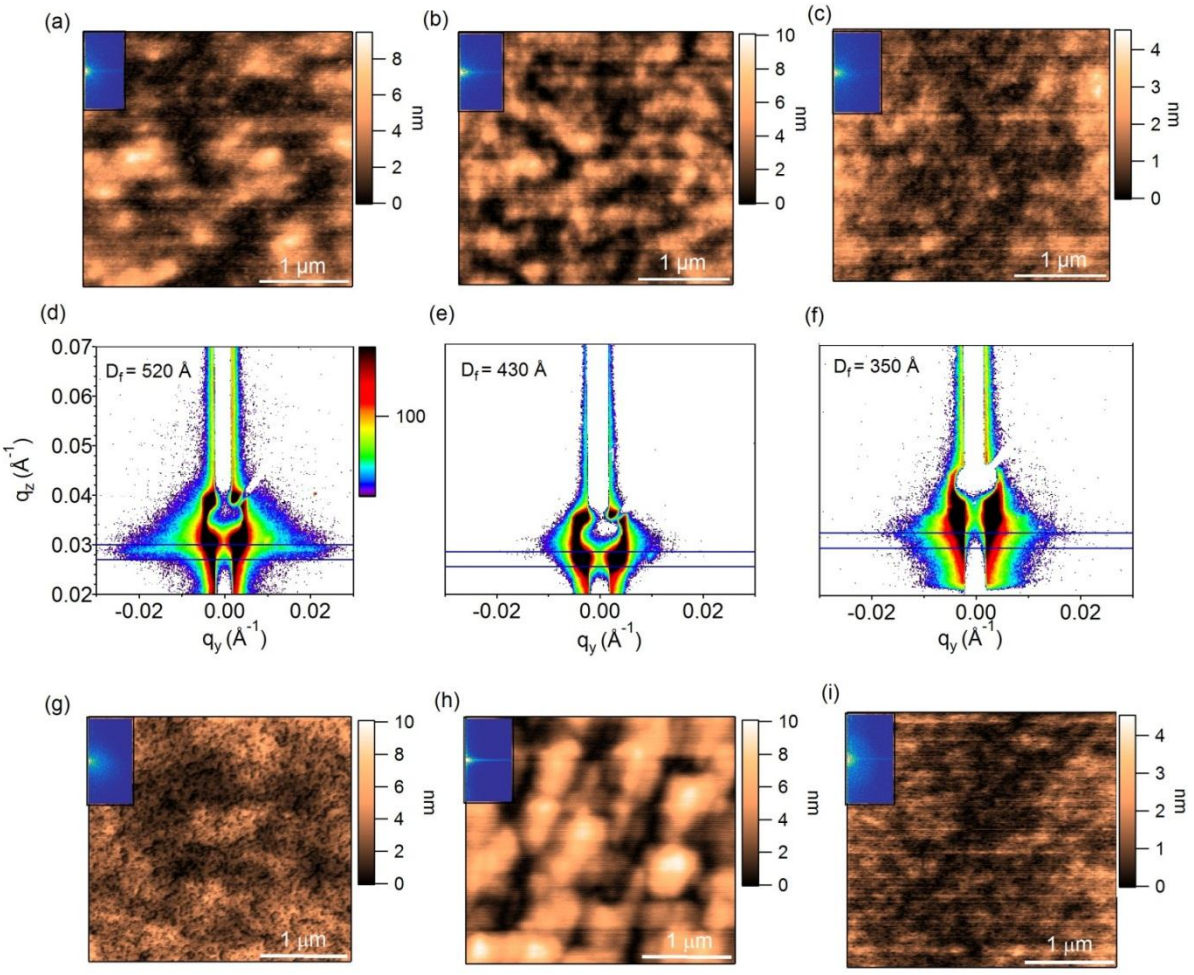

Figure 5.1. Ex-situ investigations. For each film thickness (given in the figure), three images are shown: AFM image of the as-prepared film (a-c), 2D GISAXS images of the as-prepared film (d-f), and AFM images after one vapour/drying cycle (g-i). The AFM height images have a size of 3 µm × 3 µm. The insets show the corresponding 2D Fourier transforms, ranging from -0.005 to 0.005 Å^{-1}. The color scale for all GISAXS pictures is the same as in Fig. 5.1d. The white stripes in the center are due to the beamstops. The blue horizontal lines in the GISAXS images show the regions used to construct the intensity profiles.

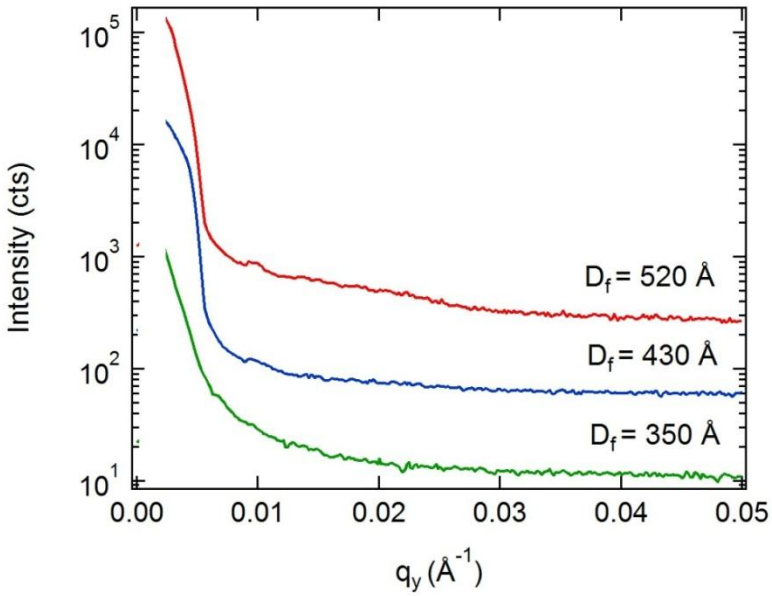

Figure 5.2. As-prepared films. 1D GISAXS intensity profiles along q_y for the three different thicknesses. The film thicknesses are given for each profile. The curves are shifted vertically.

To elucidate the formation of lateral structures by treatment with saturated HX vapour, we investigated the surface structures ex-situ AFM after one vapour/drying cycle (Figure 5.1g-i). The surface texture of the thick film after the first vapour/drying cycle shows a weak, small-scale structure (Figure 5.1g). It is not regular enough to result in a peak in the 1D Fourier transform, though. The RMS surface roughness is 15 Å, the surface is thus smoother than in the as-prepared film. In contrast to the thick film, large surface structures appear in the film with intermediate thickness after vapour treatment and drying (Figure 5.1h). The Fourier transform does not show any peak, though. The RMS surface roughness is now 25 Å, thus higher than in the as-prepared film. At the surface of the thin film, small structures appear after one vapour/drying cycle (Figure 5.1i). The 2D Fourier transform shows no feature. The RMS surface roughness is 10 Å, thus unchanged from the as-prepared film. The AFM images of the three films are thus not conclusive of the possible internal

structural changes during the vapour treatment and drying since only weak and irregular structures are present.

The processes going on during one or two vapour/drying cycles were monitored using time-resolved GISAXS. In these experiments, vapour treatment was started by injecting 1-2 ml of HX into the reservoir at the bottom of the sample cell (~1-2 cm below the sample). After ~45 min, drying was started by flushing the cell with dry N_2 gas.

Thick film. The changes in the thick film during exposure to saturated HX vapour are evident from the time series of GISAXS images shown in figure 5.3. After injection of liquid HX into the cell, out-of-plane peaks appear at q_y = 0.02 $Å^{-1}$ and become more intense with time, i.e. an increasing fraction of the film contributes to the scattering from a lateral structure. The peak intensity keeps growing until the end of the vapour treatment. We attribute these peaks to the enhanced part (Yoneda band) of the first-order DDSR due to a randomly oriented lamellar structure (Figure 2.9). The repeat distance of the lateral structure, D_{lam}, is determined by reading off the q_y peak position. Initially, i.e. after 1 min of swelling, it amounts to 314 Å (Equation 2.2); this thickness of the swollen lamella is already significantly larger than D_{lam}^{bulk}.[1] The 1D intensity profiles (Figure 5.4) show an intensity maximum due to this DDSR, which becomes significantly more intense after ~8 min and which changes position in a complex way with time. During drying, the peak weakens immediately (Figure 5.3).

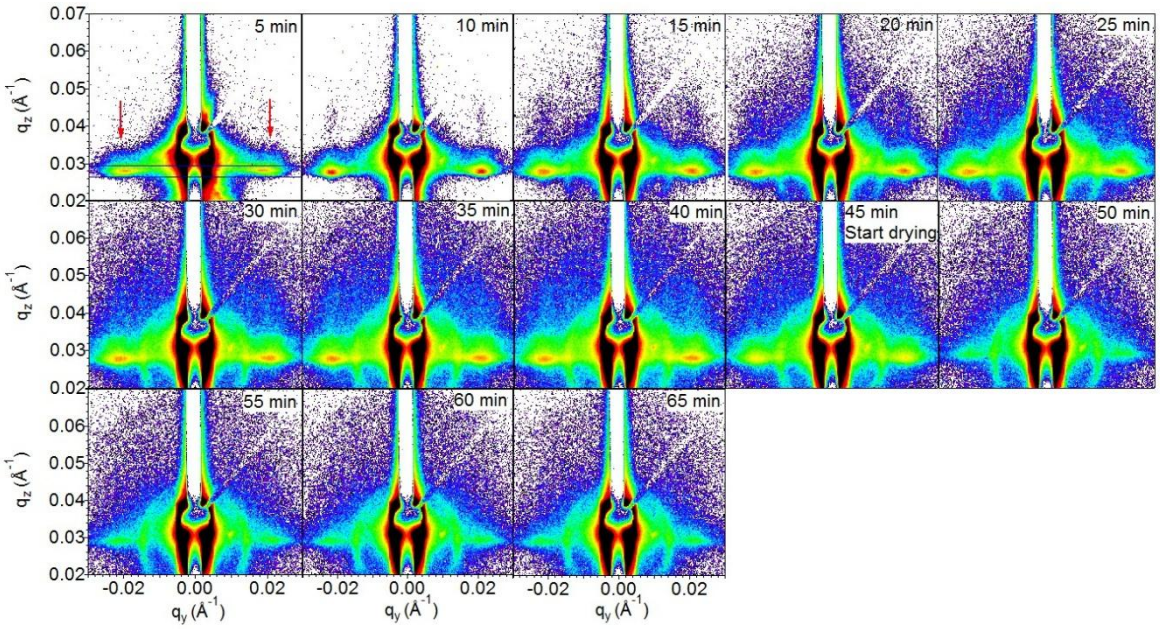

Figure 5.3. Representative GISAXS images of the thick film during treatment with HX vapour and subsequent drying, taken at α_i = 0.22°. The times after injection of HX into the cell are given in each image. Drying starts after 45 min by starting a flow of N_2 gas. The arrows mark the DDSRs. The ring-like features are due to scattering from Kapton. For all images, the color scale and the regions used to construct the intensity profiles are the same as in figure 5.1d.

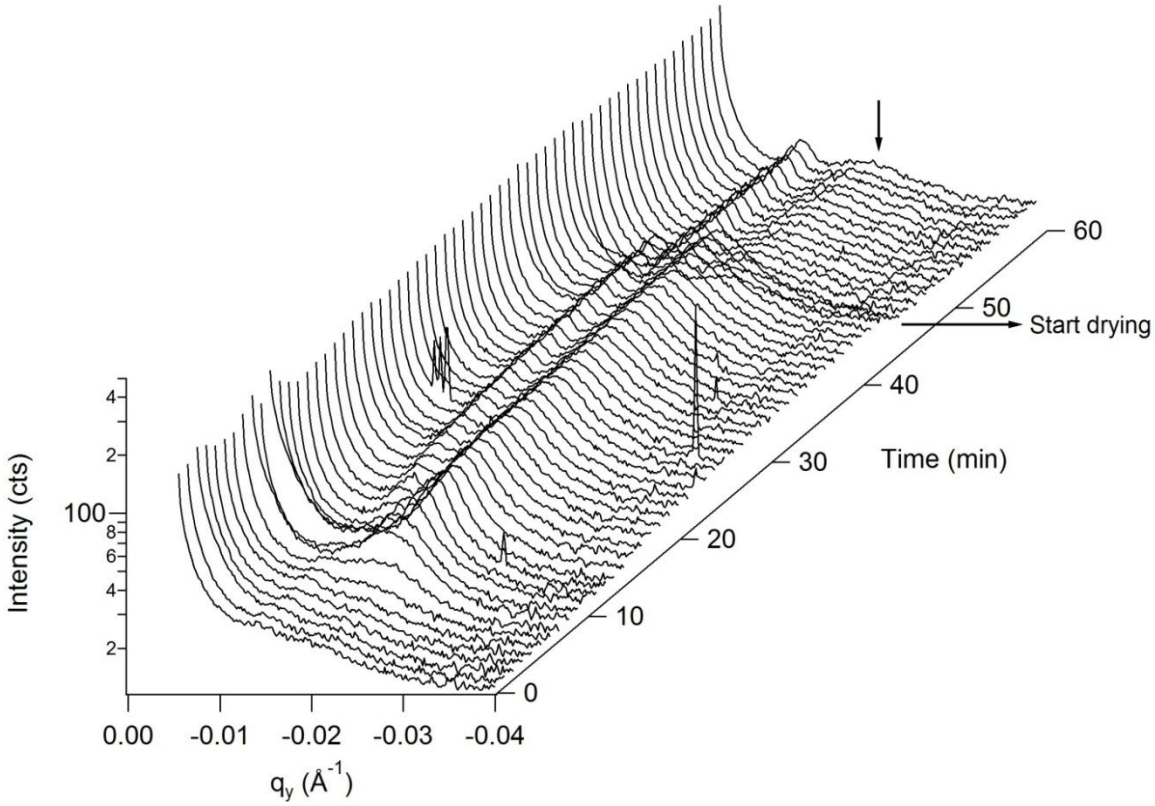

Figure 5.4. Thick film during the first cycle of vapour treatment and subsequent drying. Intensity profiles along q_y as a function of time, centered at q_z = 0.028 Å^{-1}. The vertical arrow indicates the position of the first-order DDSR. An additional peak at a lower q_y value of 0.014 Å^{-1} is due to scattering from the Kapton windows. The drying starts at the marked position.

From the q_y position of the peak, we calculate the repeat distance, D_{lam}, as a function of time (Figure 5.5a). It becomes possible to read off a peak position after 1 min. During the first 10 min, D_{lam} decreases until it reaches 293 ± 2 Å, then stabilizes after a small overshoot at 297 ± 2 Å after 21 min. It remains nearly unaffected by the drying process with the final value being 296 ± 2 Å, which is still higher than D_{lam}^{bulk}; indicating remaining solvent in the film. The number of correlated lamellae, N_S, in the

film plane (Equation 5.2), increases from ~1.3 and reaches a maximum of $N_s = 4$ after 5 min, then slowly decreases and stabilizes at a value of ~2 after 21 min (Figure 5.5b). The value of N_s decreases abruptly to a value of 1.4 upon drying. Even though the DDSRs are weak during drying, they are still present, i.e. the lateral orientation is partially maintained. The second vapour/drying cycle shows that the behavior of both D_{lam} and N_S during the first cycle is qualitatively reproducible.

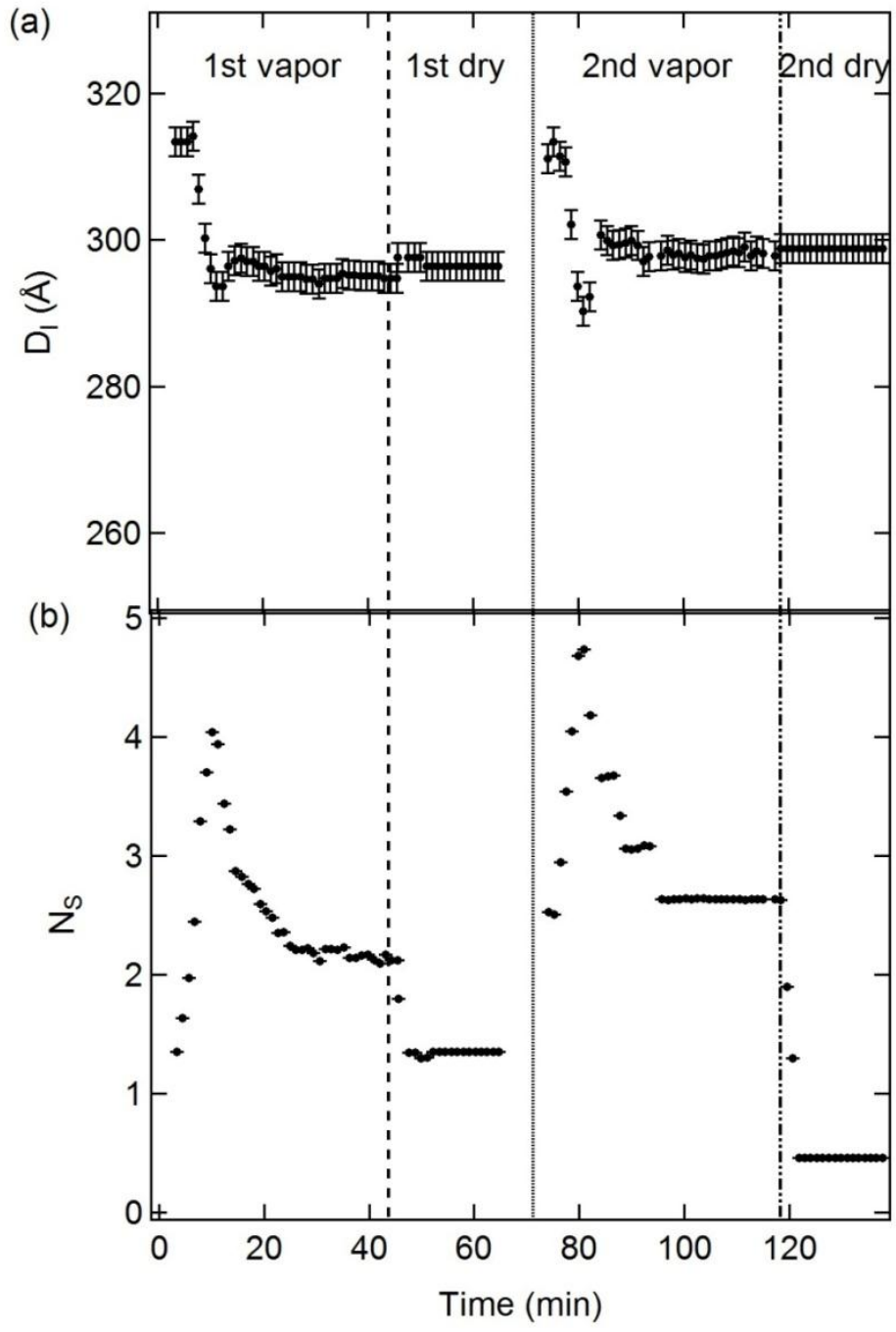

Figure 5.5. GISAXS results of the thick film. (a) Lateral repeat distance, D_{lam}, and (b) number of correlated lamellae, N_S, as a function of treatment time. The dashed, dotted and dash-dotted lines indicate the start of the first drying, the second vapour treatment and the second drying.

Thus, in the thick film, we observe a tendency to a formation of the lamellar structure. This structure is most ordered after 5 min when the number of correlated lamellae is maximum. Further vapour treatment results in a partial deterioration of the structure. Moreover, upon drying, the structure is only partially stable which explains why the resulting surface texture is only weak (Figure 5.1g). The lateral repeat distance shows relatively fast kinetics with the changes being finished within ~20 min upon vapour treatment and ~5 min upon drying.

Intermediate film. During exposure to saturated HX vapour and drying, the GISAXS maps of the P(OS-*b*-BMA) film with D_{film} = 430 Å show qualitatively the same behavior as the thick film (Figure 5.6). However, the changes are slightly faster than in the thick film. The DDSR becomes more intense during the vapour treatment, i.e. the fraction of the film displaying a lateral structure increases with time. In contrast to the thick film, the growth of the peak intensity stops already after ~20 min. When drying is started, the DDSR weakens immediately. A second cycle of vapour treatment and subsequent drying was not performed due to beam time restrictions.

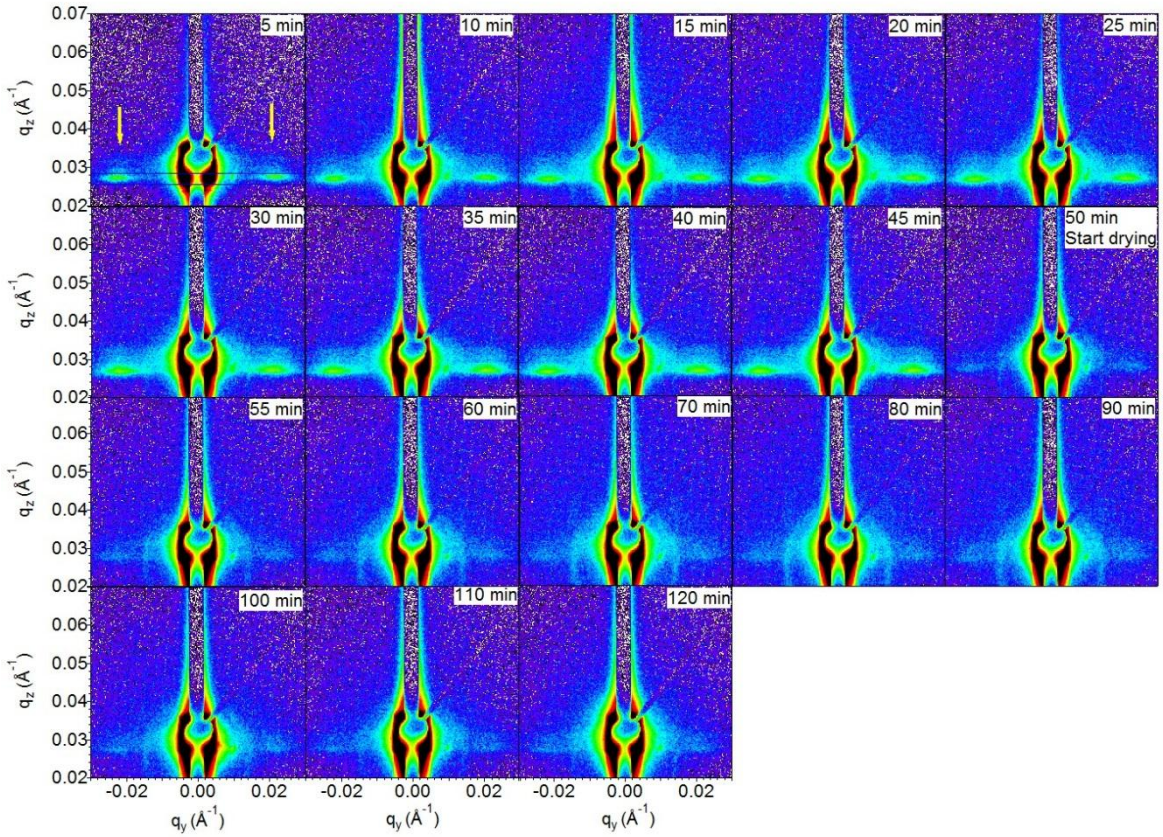

Figure 5.6. Representative GISAXS images of the film with intermediate thickness during treatment with HX vapour and subsequent drying, taken at α_i = 0.20°. Same scale and notation as in figure 5.3.

The 1D intensity profiles as well as the resulting fitting parameters (Figures. 5.7, 5.8) show qualitatively very similar behavior to the one of the thick film. However, the time and length scales are different – the minimum of D_{lam} is reached already after 8 min, thus earlier than in the thick film, and the final value of D_{lam} in the vapour is with 289 ± 2 Å slightly lower than in the thick film. Also the overshoot of N_S at N_s = 3 takes place earlier (after 5 min) than in the thick film. N_s reaches a final value of ~2, which is similar to the value in the thick film. The height of the peak settles after ~20 min and does not continue to grow as in the thick film.

Upon drying, the peak nearly vanishes, therefore no further fitting is possible.

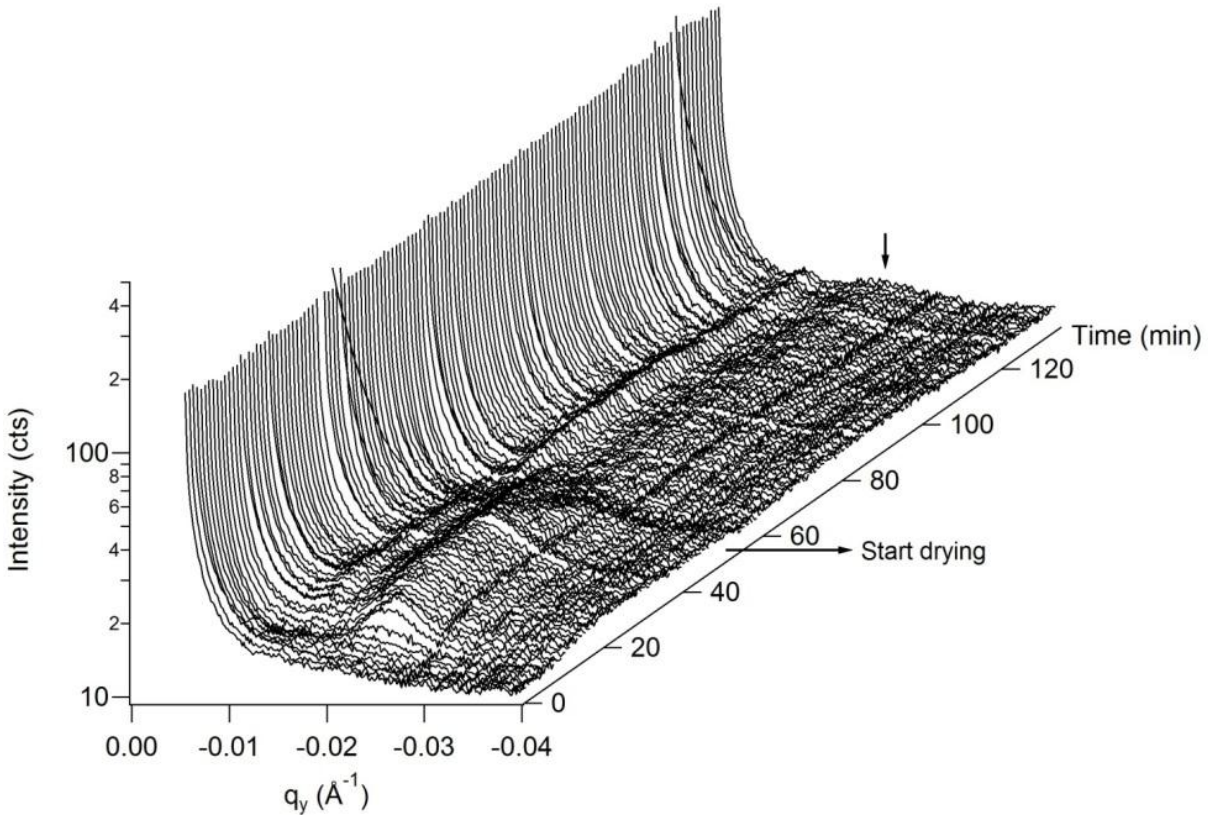

Figure 5.7. Intermediate film during the first cycle of vapour treatment and subsequent drying. Intensity profiles along q_y as a function of HX vapour treatment time and subsequent drying, centered at q_z = 0.027 Å^{-1},. Same notation as in figure 5.4.

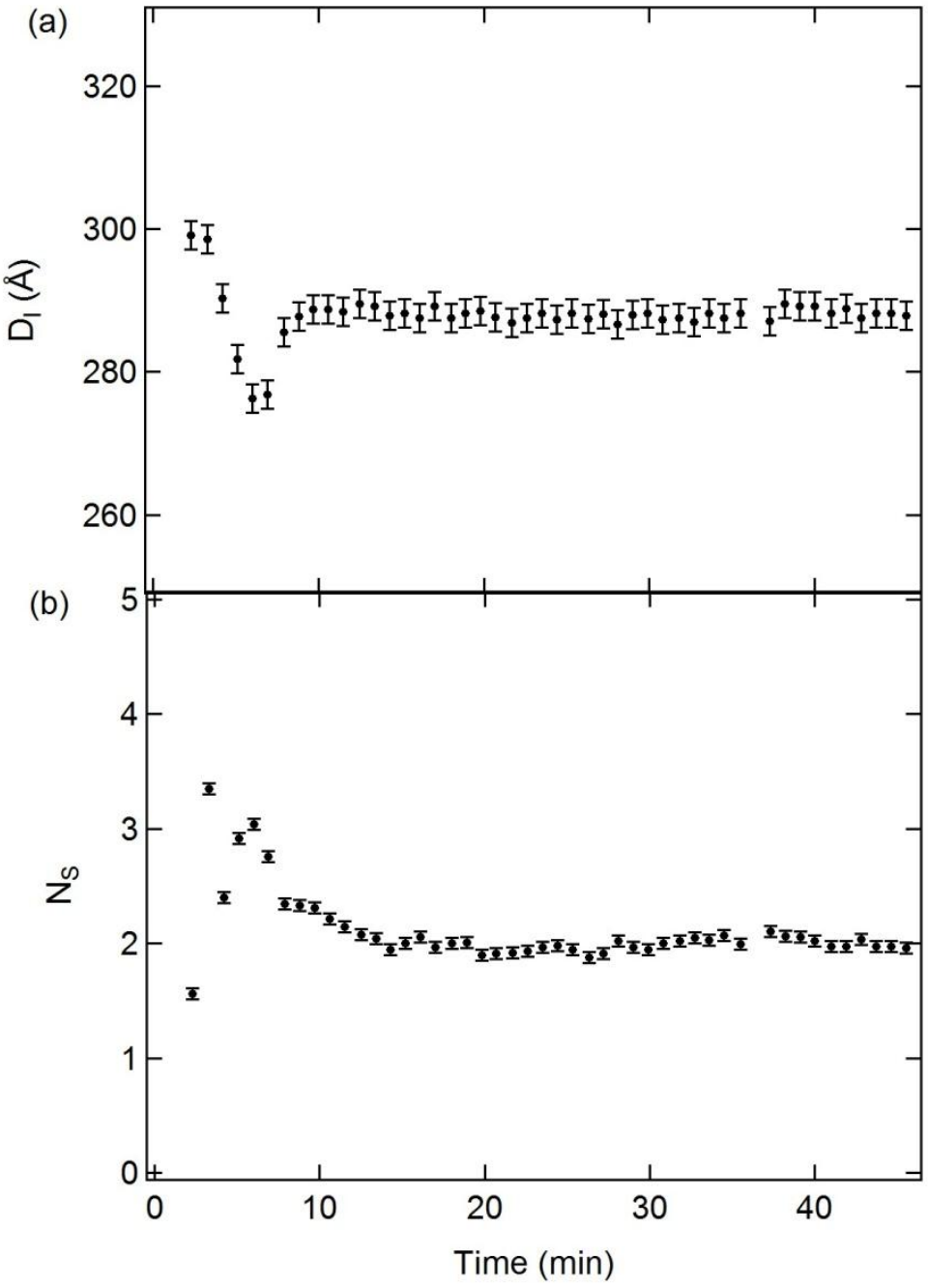

Figure 5.8. GISAXS results of the film with intermediate thickness. (a) Lateral repeat distance, D_{lam}, and (b) number of correlated lamellae, N_S, as a function of treatment time.

Thin film. During exposure to saturated HX vapour, the thin film shows a behavior completely different from the previous ones. The GISAXS maps of the P(OS-*b*-BMA) film with D_{film} = 350 Å show a very weak DDSR, much weaker than the ones observed in the intermediate and the thick films, pointing to a poorly defined lateral order (figure 5.9). It keeps becoming more intense during the first ~30 min and then stops growing. Upon drying, the DDSR weakens immediately, as in the two thicker films.

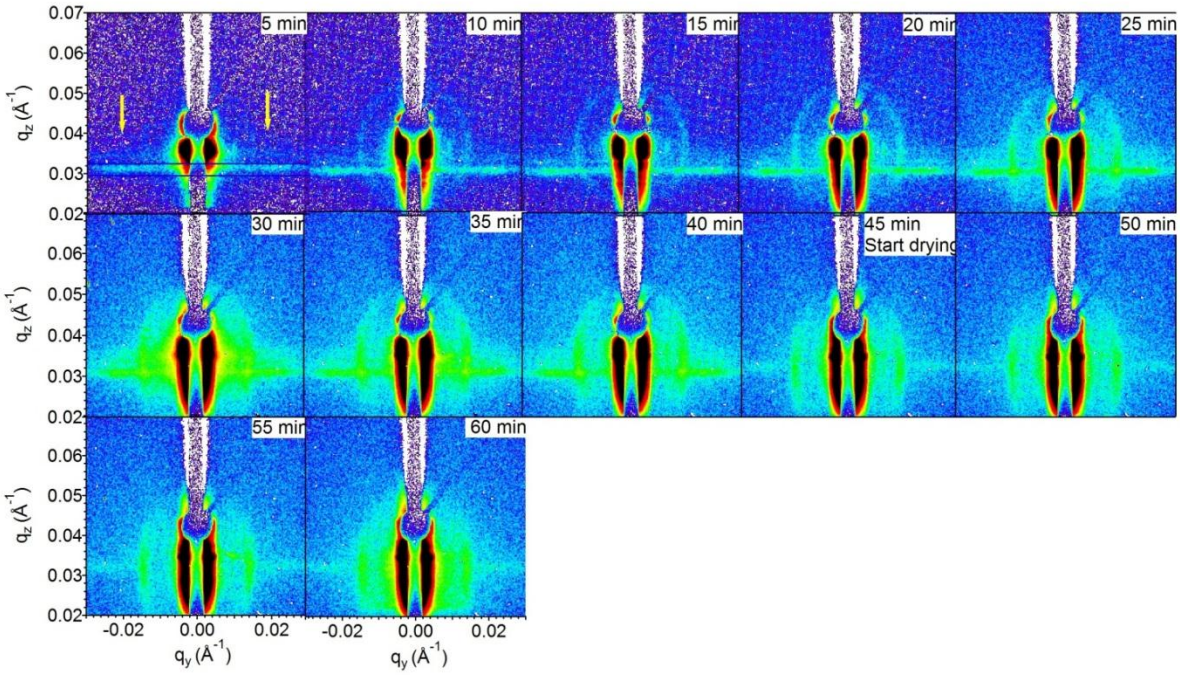

Figure 5.9. Representative GISAXS images of the thin film during treatment with HX vapour and subsequent drying, taken at α_i = 0.25°. Same scale and notation as in figure 5.3.

The 1D intensity profiles show that the intensity of the peaks due to the DDSR starts to increase only after ~10 min (figure 5.10). The behavior of D_{lam} is very different from the one in the two thicker films: During the first 30 min, D_{lam} increases slowly until it reaches a broad maximum at 296 $\pm$ 2 Å after 40 min and decreases to a value of 289 $\pm$ 2 Å at the end of the vapour treatment (Figure 5.11a). These changes are much slower than in the intermediate and the thick film. During the first 9 min of vapour treatment, N_S increases to ~1.5 during the first ~10 min, then decreases to very low values (Figure 5.11b).

Upon drying, D_{lam} keeps decreasing smoothly to 272 $\pm$ 2 Å, a value close to D_{lam}^{bulk}, then, after ~10 min the peak becomes very weak but still present (figure 5.10, inset). N_S decreases abruptly upon drying to a value of ~0.8. The second vapour/drying cycle is completely different from the first one, i.e. the changes are not reproducible, possibly because the first vapour treatment was too short to reach equilibrium. Another possibility may be the deterioration of the film by the vapour treatment.

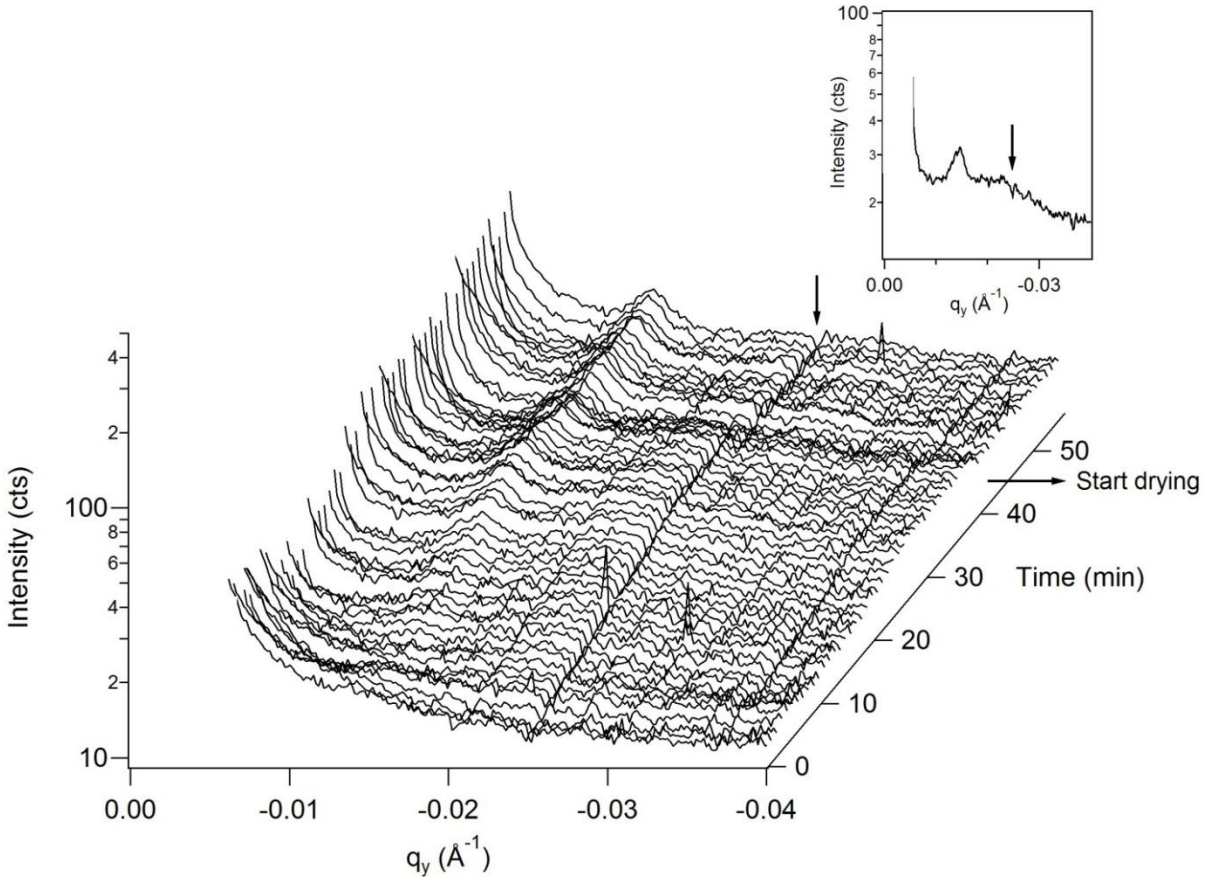

Figure 5.10. Thin film during the first cycle of vapour treatment and subsequent drying. Intensity profiles along q_y as a function of HX vapour treatment time and subsequent drying, centered at q_z = 0.031 Å^{-1}. The inset shows the intensity profile after 20 min of drying, the arrow indicates the position of the first-order DDSR. Same notation as in figure 5.4.

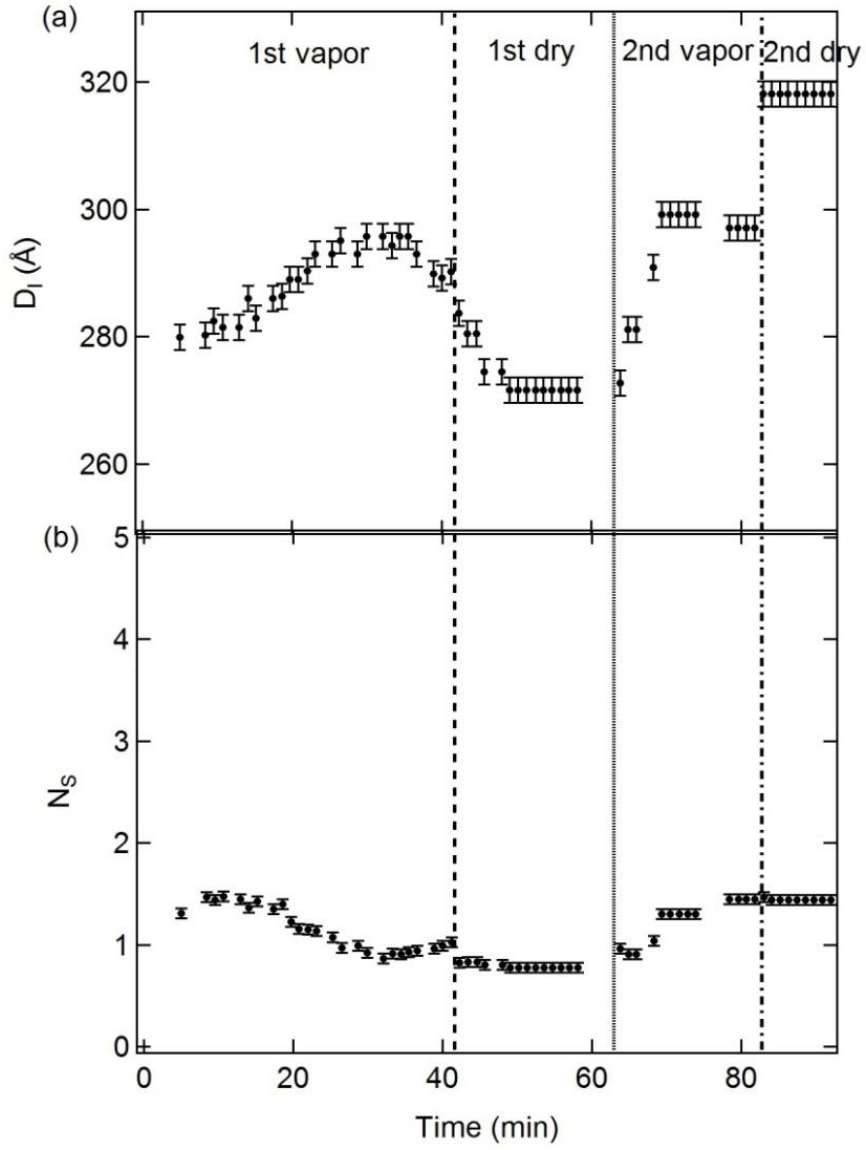

Figure 5.11. GISAXS results of the thin film. (a) Lateral repeat distance, D_{lam}, and (b) number of correlated lamellae, N_S, as a function of treatment time.

5.2 Conclusion

Thin films from lamellar P(OS-*b*-BMA) di-block copolymers are very susceptible to the quality and selectivity of the solvent. For instance, HX is a solvent which is close to non-selective and rather poor for both blocks. In the bulk, both blocks are above or only slighty below their glass transition temperature, thus vapour treatment of the P(OS-*b*-BMA) system is expected to have a relatively fast effect on the structure. Indeed, we could confirm that, on time scales similar to the ones used in the present study, thin films from poly(styrene-*b*-(butyl methacrylate)) do not show any changes in scattering during vapour treatment with HX, possibly because of the high glass transition temperature of polystyrene as well as its insolubility in HX. We conclude that, to achieve lateral structures, both blocks need to have a certain mobility.

Our study shows that lateral structures can be obtained most rapidly for the intermediate film thickness (430 Å, $D_f = 1.6\times D_{lam}^{bulk}$). In the thick film ($D_{film} = 2.0\times D_{lam}^{bulk}$), the same behavior with an undershoot of D_{lam} is observed, however, on a slightly longer time scale. The reason for the difference may be due to the longer distance which the solvent molecules need to travel inside the film. In these two films, the lateral structure is partially preserved during drying. On the contrary, the thin film ($D_{film} = 1.3\times D_{lam}^{bulk}$) shows very different and very slow kinetics in HX vapour. The behavior observed confirms that a long time is needed to rearrange the originally disordered polymer material into an ordered structure. Moreover, the decrease of the value of D_{lam} after drying with decreasing film thickness points to the fact that the amount of remaining solvent in the film increases with film thickness.

The changes of the lamellar orientation observed upon vapour treatment and drying are consistent with the lateral structures observed previously after HX vapour treatment and drying using AFM.[1] Thus, for di-block copolymers with both blocks being above or close to the glass transition temperature, it is sufficient that the solvent used for treatment is a poor solvent (i.e. better than a non-solvent) in order to alter the lateral structure orientation, instead of e.g. thermo-annealing of thin layers to suitable temperatures as demonstrated in Ref. 87. The present real-time, in-situ GISAXS investigations elucidate the time scales of the structural changes, in contrast to methods like transmission electron microscopy (TEM) which is used to inspect the internal structure of polymer thin films is limited to stable structures.[88] Neither is ex-situ, post-treatment AFM not sufficient to reveal these processes since it only monitors the surface texture.

Chapter 6

Conclusion

The structural ordering in thin block copolymer films during thermal and solvent vapour treatment has been studied, focusing on the changes of the lamellar structure. In order to relate these changes to the changes of chain conformation, in-situ GISAXS, together with SAXS, XR, VIS-interferometry and AFM has been employed; this allowed us to follow the structural rearrangement in-situ.

Two different di-block copolymer systems have been studied: poly(styrene-*b*-butadiene), with high and low molar mass, and poly(4-octylstyrene-*b*-butylmethacrylate). Both copolymers were prepared by means of living anionic polymerization and spin-coated in solution on a silicon substrate in order to obtain di-block copolymer thin films. In both cases the Si substrate was treated in order to tune its surface energy. We observed that the substrate treatment is fundamental in order to obtain a thin film with well-defined morphologies.

We have chosen P(S-*b*-B) because it is a well-known system which exhibits a low T_g for the PB block and an high T_g for the PS block, moreover it shows a well-defined initial lamellar orientation. This was, therefore, a good starting point in order to understand the mechanism underlying the process of lamellar ordering on a large scale. The P(OS-*b*-BMA), instead, was selected because it is a new system where both the block exhibits a low T_g, furthermore the lateral structures can be created and controlled by means of an appropriate choice of selective solvents. Moreover a methodic study on the effect of the film thickness on the lamellar structures was possible.

Thermal treatment was employed in order to induce lamellar structural reorganization. In this study we have successfully related the glass transition temperature of the glassy polymer (PS) with the polymer mobility, which induces the large scale ordering of the block copolymer structures. In consistency with theoretical predictions, we have shown that the best correlated structure for our P(S-*b*-B) system with high molar mass is obtained by treatment at 100°C. A methodic study was performed and a large range of temperatures was probed, both below and above the T_g(PS). For temperatures below T_g(PS), after cooling down the system to room temperature, the perpendicular lamellar orientation is unchanged inside the film, and only a local improvement is observed at the surface. Above T_g(PS), structural

changes do occur both during heating and during cooling, moreover at the film surface, a severe rearrangement is observed, with PB migrating to the top of the film surface. Although the glass transition temperature is a well know phenomenon, it was never directly related to the effect on the polymer mobility and therefore to the large scale rearrangement of the nanostructures within thin films, as instead methodically shown in this PhD. thesis.

Vapour annealing has been used as tool in order to induce structural ordering and structure formation within di-block copolymer thin films, for low molar mass P(S-*b*-B) and P(OS-*b*-BMA).

In the case of the P(S-*b*-B) with low molar mass the scaling behaviour of the lamellar thickness has been studied and projected within the framework of the mean-field theory. Therefore, we developed a model for the description of the dependence of the D_{lam} on the polymer volume fraction upon solvent vapour treatment and subsequent drying, identifying the structural changes and large scale rearrangement occurring within the whole film thickness during the vapor and drying treatment. In particular, we pointed out the importance of the solvent selectivity which affects the initial swelling of the whole system, identifying then the conditions which lead to the formation of additional lamellae. Moreover, with our methodic study we were able to identify the best vapor and drying treatment protocol, which we applied to block copolymer thin films in order to induce a long-range ordering of the nanostructures within the film itself. This study is consistent with the previous observations of our group, adding an important contribution: in the study presented in this PhD. thesis the key role of the drying process has been highlighted. Drying the sample in a controlled way and monitoring the whole process in-situ allowed us to identify the crucial step of lamellar formation and reorganization in presence of selective solvent. Many studies focus mainly on the importance of the vapour treatment, we demonstrated the key role played by the drying treatment in inducing both structural ordering and structure formation, understanding the link between the lamellar structural reorganisation and the polymer volume fraction.

The vapor treatment of P(OS-*b*-BMA) allowed us to understand the role of solvent selectivity and polymer mobility on the creation of lateral structures. We methodically studied the effect of solvent vapor treatment on films with different thicknesses. Our study shows that for thicker films, with thickness comprised between 400 and 500 Å, lamellar structures are created during solvent vapor treatment and the lateral structure is partially preserved during drying. We observed that thicker is the film slower will be the lateral structure creation, mainly due to the distance which the solvent molecules need to travel inside the film itself. In the case of the thin films, ~300 Å, we were able to identify the major role of the film thickness and compare it with the case of thicker films: the lamellar swelling is strongly affected by the amount of remaining solvent into the whole film thickness, therefore a longer time is needed to rearrange the disordered structures into an ordered one. Our results are consistent

with previous studies, in addition we highlighted the role of solvent selectivity on the block copolymer nanostructures formation, in particular identifying a more controlled method than the thermal annealing to achieve lateral structure formation and ordering. In fact, in the case of di-block copolymers with both blocks being above or close to the glass transition temperature, it is sufficient that the solvent used for treatment is a poor solvent in order to alter the lateral structure orientation.

The present PhD. thesis shows that thermal annealing is an important tool to identify the crucial role of the glass transition temperature on the polymer mobility, meanwhile the solvent vapour treatment can precisely control the formation and ordering of the nanostructures in block copolymer thin films, therefore accurately affecting the polymer mobility itself with respect of the T_g, indeed. Our conclusions are consistent with previous studies and theoretical predictions, but adding contributions to the understanding of block copolymer thin films ordering and kinetics, elucidating processes which have been not completely covered by other studies.

List of publications

1. **A. Sepe**, D. Posselt, S. Jaksch, R. Steinacher, J. Zhang, J. Perlich, D.-M. Smilgies and C.M. Papadakis. *Structural ordering in block copolymer thin films during solvent vapour treatment*. **In preparation for Macromolecules**

2. **A. Sepe**, Z. Di, P. Černoch, P. Štěpánek, C. Darko, D.M. Smilgies, A. Timmann and C.M. Papadakis. *Creation of lateral structures in di-block copolymer thin films during vapour uptake and subsequent drying.* **Submitted to Langmuir**

3. **A. Sepe**, E.T. Hoppe, S. Jaksch, D. Magerl, Q. Zhong, J. Perlich, D. Posselt, D.-M. Smilgies, and C.M. Papadakis. *The effect of heat treatment on the internal structure of nanostructured block copolymer films.* **Journal of Physics: Condensed Matter 23, 254213 (2011)**

4. **A. Sepe**, E.T. Hoppe, D. Posselt, J.-F. Moulin, D.-M. Smilgies and C.M. Papadakis. *Solvent distribution in block copolymer thin films.* **FRM II Scientific Highlights, Neutron Research Reactor, Technische Universität München, München, Germany, 2010.**

Bibliography

[1] Černoch, P.; Štěpánek, P.; Pleštil, J.; Šlouf, M.; Sidorenko, A.; Stamm, M. *Eur. Polym. J.* **2007**, *43*, 1144-1153.
[2] Rubinstein, M.; Colby, R.H. *Polymer Physics* **2003**, *Oxford University Press*.
[3] Fasolka, M.J.; Mayes, A.M. *Annu. Rev. Mater. Res.* **2001**, *31*, 323-55
[4] Strobl, G. *The Physics of Polymers* **2007**, *Springer*.
[5] Botiz, I.; Darling, S.B. *Mater. Today* **2010**, *13*, 42-51.
[6] Hashimoto, T.; Shibayama, M.; Kawai, H. *Macromolecules* **1980**, *13*, 1237.
[7] Hamley, I.W. *Wiley* **2004**, *Developments in Block Copolymer Science and Technology.*
[8] Wang, J.-Y.; Park, S.; Russell, T.P. *World Scientific Publishing* **2008**, *Polymer thin films.*
[9] Knoll, A.; Horvat, A.; Lyakhova, K.S.; Krausch, G.; Sevink, G.J.A.; Zvelindovsky, A.V.; Magerle, R. *Phys. Rev. Lett.* **2002**, *89*, 035501/1-4.
[10] Walton, D.G.; Kellogg, G.J.; Mayes, A.M.; Lambooy, P.; Russell, T.P. *Macromolecules* **1994**, *27*, 6225.
[11] Matsen, M.W. *J. Chem. Phys.* **1997**, *106*, 7781.
[12] Huang, E.; Mansky, P.; Russell, T.P.; Harrison, C.; Chaikin, P.M.; Register, R.A.; Hawker, C.J.; Mays, J. *Macromolecules* **2000**, *33*, 80.
[13] Tang, W.H. *Macromolecules* **2000**, 33, 1370.
[14] Morkved, T.L.; Jager, H.M. *Europhys. Lett.* **1997**, *40*, 643.
[15] Russell T.P.; Menelle, A.; Anastasiadis, S.H; Satija, S.K.; Majkrzak, C.F. *Macromolecules* **1991**, 24, 6263.
[16] Papadakis, C.M.; Almdal, K.; Mortensen, K.; Posselt, D. *J. Phys. II France* **1997**, *7*, 1829.
[17] Hamley, I.W. *Prog. Polym. Sci* **2009**, *34*, 1161-1210.
[18] Fukunaga, K.; Elbs, H.; Magerle, R.; Krausch, G. *Macromolecules* **2000**, *33*, 947-53.
[19] Fukunaga, K.; Hashimoto, T.; Elbs, H.; Krausch, H. *Macromolecules* **2002**, *35*, 4406-13.
[20] Kim, S.H.; Misner, M.J.; Xu, T.; Kimura, M.; Russell, T.P. *Adv Mater* **2004**, *16*, 226-31.
[21] Kim, S.; Briber, R.M.; Karim, A.; Jones, R.L.; Kim, H.C. *Macromolecules* **2007**, *40*, 4102-5.
[22] Papadakis, C.M.; Di, Z.Y.; Posselt, D.; Smilgies, D.-M. *Langmuir* **2008**, *24*, 13815-8.
[23] Chen, Y.; Huang, H.; Hu, Z.; He, T. *Langmuir* **2004**, *20*, 3805-8.
[24] Torkarev, I.; Krenek, R.; Burkov, Y.; Schmeisser, D.; Sidorenko, A.; Minko, S.; Stamm, M. *Macromolecules* **2005**, *38*, 507-16.

[25] Di, Z.; Posselt, D.; Smilgies, D.-M.; Papadakis, C.M. *Macromolecules* **2010,** *43,* 418.
[26] Bercea, M.; Wolf, B. A. *J. Chem. Phys*, **2006**, *124*, 174902.
[27] Fredrickson, G.H.; Helfand, E. *J. Chem. Phys.* **1987**, *87*, 697-705.
[28] Helfand, E; Tagami, Y. *J. Chem. Phys.* **1972**, *56*, 3592-3601.
[29] Orwoll, R.A.; Arnold, P.A. *AIP press* **1996**, *Physical Properties of Polymers Handbook.*
[30] Schuld, N.; Wolf, B. *John Wiley & Sons* **1999**, *Polymer Handbook 4th Edition*.
[31] Leibler, L. *Macromolecules* **1980**, *13*, 1602.
[32] Rudd, J.F. In Polymerhandbook 2nd ed.; Brandrup, J.; Immergut, E.H., Eds.; Wiley: New York, **1989**.
[33] Turturro, A.; Gattiglia, E.; Vacca, P.; Viola, G.T. *Polymer* **1995**, *36*, 3987.
[34] Papadakis, C. M.; Almdal, K.; Mortensen, K.; Posselt, D. *Europhys. Lett.* **1996,** *36*, 289-294.

[35] NanoCalc 2000, *Ocean Optics manual*
[36] Filmetrics F30, *Filmetrics manual*.
[37] http://www.polymer-physics.uwaterloo.ca/equipment/afm.htm
[38] http://www.gisaxs.de
[39] Müller-Buschbaum, P. *Anal.Bioanal.Chem.* **2003**, *376*, 3.
[40] Roth, S.V.; Döhrmann, R.; Dommach, M.; Kuhlmann, M.; Kröger, I.; Gehrke, R.; Walter, H.; Schroer, C.; Lengeler, B.; Müller-Buschbaum, P. *Rev. Sci. Instrum.* **2006**, *77*, 085106.

[41] Smilgies, D.-M.; Li, R.; Di, Z.; Darko, C.; Papadakis, C.M.; Posselt, D. *Mater. Res. Soc. Symp. Proc.* **2009** *1147* OO01.
[42] Busch, P.; Rauscher, M.; Smilgies, D.-M.; Posselt, D.; Papadakis, C.M. *J. Appl. Cryst.* **2006**, *39*, 433.
[43] Li, M.; Douki, K.; Goto, K.; Li, X.; Coenjarts, C.; Smilgies, D.-M.; Ober, C.K. *Chem. Mater.* **2004***, 16*, 3800.
[44] Sanjeeva Murthy, N. *The Rigaku Journal* **2004**, *21*, 15-24
[45] Pickett, G.T.; Witten, T.A.; Nagel. S.R. *Macromolecules* **1993**, *26*, 3194.
[46] Sommer, J.-U.; Hoffmann, A.; Blumen, A. *J. Chem. Phys.* **1999**, *111*, 3278.
[47] Potemkin, I.I. *Macromolecules* **2004**, *37*, 3505.
[48] Potemkin, I.I.; Busch, P.; Smilgies, D.-M.; Posselt, D.; Papadakis, C.M. *Macromol. Rapid Commun.* **2007**, *28*, 579.
[49] Y. Tsori, E. Sivaniah, D. Andelman, T. Hashimoto *Macromolecules* **2005**, *38*, 7193.
[50] Geisinger T.; Müller, M.; Binder K. *J. Chem. Phys.* **1999**, *111*, 5241 and 5251.
[51] Smilgies, D.-M.; Busch, P.; Papadakis, C.M.; Posselt, D. *Synchr. Rad. News* **2002**, *15*, 35.
[52] Busch, P.; Posselt, D.; Smilgies, D.-M.; Rheinländer, B.; Kremer, F.; Papadakis, C.M. *Macromolecules* **2003**, *36*, 8717.

[53] Papadakis, C.M.; Busch, P.; Posselt, D.; Smilgies, D.-M. *Adv. Solid State Phys.* **2004**, *44*, 327.
[54] Müller-Buschbaum, P.; Hermsdorf, N.; Roth, S.V.; Wiedersich, J.; Cunis, S.; Gehrke, R. *Spectrochim. Acta B* **2004**, *59*, 1789.
[55] Xu, T.; Goldbach, J.T.; Misner, M.J.; Kim, S.; Gibaud, A.; Gang, O.; Ocko, B.; Guarini, K.W.; Black, C.T.; Hawker, C.J.; Russell, T.P. *Macromolecules* **2004**, *37*, 2972.
[56] Li, M.; Douki, K.; Goto, K.; Li, X.; Coenjarts, C.; Smilgies, D.-M.; Ober, C.K. *Chem. Mater.* **2004***, 16*, 3800.
[57] Lee, B.; Park, I.; Yoon, J.; Park, S.; Kim, J.; Kim, K.; Chang, T.; Ree, M. *Macromolecules* **2005**, *38* 4311.
[58] Kim, S.H.; Misner, M.J.; Yang, L.; Gang, O.; Ocko, B.M.; Russell, T.P. *Macromolecules* **2006**, *39*, 8473.
[59] Stein, G.E.; Kramer, E.J.; Li, X.; Wang, J. *Macromolecules* **2007**, *40*, 2453.
[60] Busch, P.; Posselt, D.; Smilgies, D.-M.; Rauscher, M.; Papadakis, C.M. *Macromolecules* **2007**, *40*, 630.
[61] Albalak, R.J.; Thomas, E.L.; Capel, M.S. *Polymer* **1997**, *38*, 3819.
[62] Harrison, C.; Adamson, D.H.; Cheng, Z.; Sebastian, J.M.; Sethuraman, S.; Huse, D.A.; Register, R.A.; Chaikin, P.M. *Science* **2000**, *290*, 1558.
[63] Tsarkova, L.; Horvat, A.; Krausch, G.; Zvelindovsky, A.V.; Sevink, G.J.A.; Magerle, R. *Langmuir* **2006**, *22*, 8089.
[64] Kelly, J.Y.; Albert, J.N.L.; Howarter, J.A.; Kamg, S.; Stafford, C.M.; Epps III, T.H.; Fasolka, M.J. *Appl. Mater. Interfaces* **2010**, *2*, 3241
[65] Zhang, X.; Yager, K.G.; Fredin, N.J.; Ro, H.W.; Jones, R.L.; Karim, A.; Douglas J.F. *ACS Nano* **2010**, *4*, 3653
[66] Yager, K.G.; Fredin, N.J.; Zhang, X.; Berry, B.C.; Karim, A.; Jones, R.L. *Soft Matter* **2010**, *6*, 92
[67] Albalak, R. J.; Capel, M. S.; Thomas, E. L. *Polymer* **1998**, *39*, 1647.
[68] Kim, S. H.; Misner, M. J.; Xu, T.; Kimura, M.; Russell, T. P. *Adv. Mater.* **2004**, *16*, 226.
[69] Xuan, Y.; Peng, J.; Cui, L.; Wang, H.; Li, B.; Han, Y. *Macromolecules* **2004**, *37*, 7301.
[70] Ludwigs, S.; Schmidt, K.; Krausch, G. *Macromolecules* **2005**, *38*, 2376.
[71] Bang, J.; Kim, S. H.; Drockenmuller, E.; Misner, M. J.; Russell, T. P.; Hawker, C. J.; *JACS* **2006**, *128*, 7622.
[72] Peng, J.; Han, Y.; Knoll, W.; Kim, D. H. *Macromol. Rapid Commun.* **2007**, *28*, 1422.
[73] Noolandi, J.; Hong, K. M. *Ferroelectrics* **1980,** *30*, 117-123.
[74] Shibayama, M.; Hashimoto, T.; Hasegawa, H.; Kawai, H. *Macromolecules* **1983**, *16*, 1427.
[75] Di, Z.; Posselt, D.; Smilgies, D.-M.; Li, R.; Rauscher, M.; Potemkin, I.I.; Papadakis, C.M. *Macromolecules* **2012**, submitted.

[76] Smilgies, D.M. *J. Appl. Crystallogr.* **2009**, *42*, 1030-1034.

[77] Busch, P.; Rauscher, M.; Moulin, J.-F.; Müller-Buschbaum, P. *J. Appl. Crystallogr.* **2011**, 44(2), 370-379.

[78] Gutmann, J.S.; Müller-Buschbaum, P.; Schubert, D. W.; Stribeck, N.; Smilgies, D.-M.; Stamm, M. *Physica B* **2000**, *283*, 40.

[79] Strobl, G. R. *The Physics of Polymers*; Springer: Berlin, 1996.

[80] Helfand, E.; Tagami, Y.J. *J. Chem. Phys*, **1972**, *56*, 3592-3601.

[81] Bercea, M.; Wolf, B. A. *J. Chem. Phys*, **2006**, *124*, 174902.

[82] Müller-Buschbaum, P.; Gutmann, J.S.; Wolkenhauer, M.; Kraus, J.; Stamm, M.; Smilgies, D.; Petry, W. *Macromolecules* **2001**, *34*, 1369-1375

[83] Goffloo, K.; Kosfeld, R. *Angew. Makromol. Chem.* **1974**, *37*, 105.

[84] Tang, I.; Lu, J. R.; Lewis, A. J.; Vick, T. A.; Stratford, P. W. *Macromolecules* **2002**, *35*, 3955.

[85] Müller-Buschbaum, P.; Bauer, E.; Cubitt, R. *Phyisica B* **2006**, *385-386*, 703.

[86] Sepe, A.; Hoppe, E.T.; Jaksch, S.; Magerl, D.; Zhong, Q.; Perlich, J.; Posselt, D.; Smilgies, D.-M.; Papadakis, C.M. *J. Phys.: Condens. Matter* **2011**, *23*, 254213.

[87] Morkved, T.L.; Jaeger, H.M. *Europhys. Lett.* **1997**, *40*, 643.

[88] Radzilowski, L.H.; Carvalho, B.L.; Thomas, E.L. *J. Polym. Sci. B: Polym Phys.* **1996**, *34*, 3081.